



PONTIFICIA UNIVERSIDAD CATÓLICA DE CHILE
INSTITUTO DE FÍSICA

Dynamics of Laser-Produced Annular Plasmas and Laboratory Astrophysics Experiments With Magnetically-Driven Rotating Plasmas

by

VICENTE VALENZUELA VILLASECA

Thesis submitted to Instituto de Física,
Pontificia Universidad Católica de Chile, to partial fulfillment of
the requirements for the degree of Master of Science in Physics

SUPERVISOR : Prof. Mario Favre
EXAMINING COMMITTEE : Dr. Felipe Veloso
Dr. Donovan Díaz

August 20, 2018
SANTIAGO – CHILE

Abstract

This thesis is separated in two different parts, in which two different plasma experiments are studied.

In Part I we studied the dynamics of a plasma plume produced by focusing ring-like laser beams produced by a Nd:YAG 3.5 ns FWHM, 1064 nm wavelength laser beam focused using the combination of an axicon prism and a focusing lens onto a solid target. The experiments were carried in two different regimes of background gas pressure, ring radius and materials. Additionally the effects of a static, external magnetic field produced by NeFeB permanent magnets on the propagation of the plume were studied.

Firstly, titanium plasmas in 80 mTorr argon (Ar) background were studied using a 50 ns time resolution intensified CCD capturing the optical self-emission of the plasma. Resulting from the expansion of the annular plume a central stagnation column was observed to form in ~ 80 ns, propagating on axis at characteristic velocity $\sim 10^{5-6}$ cm/s. Following the propagation of the jet, the formation of a planar shock produced by the interaction of the plasma with the background gas was observed. This configuration changes in characteristic timescales ~ 500 ns, once the central column can no longer be observed and the planar shock transitions into a bow shock. The velocity of the plume is not considerably modified by the presence of the field, however the shape of the plume and persistence in time of the radiance of the plasma was affected. These results are ascribed by the effects of magnetic confinement and single particle trajectories, respectively. Additionally, gradients in radiance along the shock suggest temperature gradients perpendicular to the density gradients imposed by the shock.

Secondly, carbon in $\sim 0.1 - 1.0$ atm Ar experiments were carried. A neutral shock produced by the rapid expansion of the plasma is observed. Interpreted as the action of the stagnation column within the blast wave, it is observed a bubble leading the axial propagation of the shock wave, thus forming an asymmetric shock. It propagates at characteristic velocity $\sim 10^5$ cm/s and observed to be dominated by the presence of neutrals rather than plasma. However, strong electron density gradients are observed within the downstream.

Part II is focused on magnetically-driven rotating plasmas. We employed a modified Z pinch configuration consisting of a cylindrical 16 mm radius, 10 mm height arrangement of 8, 40 μm

diameter aluminium wires, which are angularly perturbed by 8 1 mm diameter steel rods used as return posts, as a load of the MAGPIE pulsed power generator (1.2 MA, 240 ns) based at Imperial College London. As a consequence of the off-axis implosion ablation stream, a seemingly rotating Z pinch the subsequent emission of a jet. The rotation is indirectly evidenced by difference in the expected diffusion times required to fill the hollow centre of the rotating plasma estimated ~ 25 ns and the lifetime of such structure > 100 ns. The density of this plasma is estimated $\sim 10^{18-21}$ cm^{-3} and it has characteristic circulation velocity $\sim 10^{6-8}$ cm/s. The jet is estimated to have an axial velocity $\sim 10^{6-7}$ cm/s. It has a high-degree of collimation and reaches a length ≥ 1.6 cm.

This experiment is framed within the field of Laboratory Plasma Astrophysics, which allow us to reproduce and isolate features of astrophysical systems in table-top experiments. A rigorous derivation of the similarity criteria to scale one environment to the other, namely laboratory to astrophysical, based upon the single-fluid magnetohydrodynamic formalism is given, obtaining the dimensionless parameters of the systems and their explicit relation with the dynamical evolution of them. Furthermore, a novel method to estimate error bars in such parameters is presented. According to the estimations benchmarked by the data, the plasma flows within this experiments are scale invariants, therefore they are comparable to other scale invariant systems, which is the case for astrophysical environments, as dissipation is dynamically negligible.

Acknowledgements

Quiero comenzar agradeciendo a mi familia y amigos/as. Ustedes han permitido tener el privilegio de poder dedicarme enteramente a este trabajo. Por su amor incondicional muchas gracias.

Gracias Rafa por ser mi compañero de tantas (tantas!) batallas, sin ti no hubiese llegado hasta acá. Gracias Emilia por tu compañía durante estos últimos meses. Gracias a Toto, Iván, Daniel, Manuel, Chirri, Leando e Ivania por tantas risas en la oficina. Gracias al grupo de Salsa por mantenerme cuerdo durante los meses más estresantes de este trabajo. Estoy muy agradecido de haberme encontrado con ustedes durante mis últimos meses en Chile y que nos hayamos hecho tan amigos.

Gracias Gonzalo, Milenko, Wilmer, Francisca, Pavel y Francisco por ser mis amigos y compañeros de guerra. Estoy profundamente agradecido de Mario por supervisar este trabajo. Tus sabios comentarios aportaron mucho a esta tesis. Gracias Felipe por enseñarme tantas cosas durante estos años trabajando juntos tus lecciones me acompañan siempre.

Gracias Tuko por apoyarme tanto desde que nos conocemos. Gracias a ti pude trabajar en conjunto al grupo de Imperial College, además de preparar postulaciones y entrevistas en el Reino Unido, sobreviviendo en el intento.

I am very grateful to the MAGPIE team and the Plasma group at Imperial College for letting me join them for a very cool couple of months. It was a truly life-changing experience. Thank you Daniel, Thomas, Jack Hare, Jack Halliday, Ellie, Sergey, Jerry, Meriame, Sav, et al. for everything. I am extremely excited to join you during the coming years.

I am very thankful to the support granted by FONDECYT grants 1171412 and 1180100 during the development of this thesis. I greatly acknowledge the Royal Astronomical Society for funding my 6-week research visit to Imperial College London through its small grants scheme. Their continuous support to the field of Laboratory Astrophysics is key to keep developing this exciting subject.

Contents

I	Dynamics of Laser-Produced Annular Plasmas	1
1	Introduction	2
1.1	Our Magnetised Universe	2
1.2	The Biermann Battery	3
1.3	Blast Waves	5
1.3.1	Solutions	7
1.3.2	The relation of the Biermann battery and asymmetric shocks	8
1.4	Laser-Produced Plasmas	8
1.4.1	Magnetic confinement effects in laser-produced plasmas	10
1.4.2	Colliding plumes in laser-produced plasma experiments	11
1.4.3	Laser-produced annular plasmas	12
1.5	Summary	13
2	Experimental Set-up	15
2.1	Annular Laser Beams	15
2.2	Principles of Diagnostics	16
2.2.1	Intensified Charged Coupled Device	16
2.2.2	Shadowgraphy & schlieren imaging	16
2.2.3	Interferometry	17
2.3	Spatial Distribution of the Experiment & Synchronisation	19
3	Experimental Results	23
3.1	Dynamics of Titanium Laser-Produced Annular Plasmas in Low Pressure Background Argon Gas	23
3.2	Dynamics of Carbon Laser-Produced Annular Plasmas in High Pressure Background Argon Gas	28
3.2.1	Shadowgraphy & schlieren imaging	29
3.2.2	Interferometry	36
4	Conclusions and Future Work	40

II	Laboratory Astrophysics Experiments With Magnetically-Driven Rotating Plasmas on the MAGPIE Generator	42
5	Introduction	43
5.1	Differentially Rotating Plasmas and Outflows in Astrophysical Environments . . .	43
5.2	Z Pinch Wire Arrays	44
5.2.1	How to produce a rotating Z pinch	44
5.3	MHD Scaling and Laboratory Astrophysics	46
5.3.1	Euler similarity	46
5.3.2	An order-of-magnitude method of quantifying errors in dimensionless parameters	51
5.4	Summary	55
6	Experimental Set-up	56
6.1	The MAGPIE Pulsed-Power Generator	56
6.2	Diagnostics	57
6.2.1	Optical fast framing	58
6.2.2	Micro-channel plate imaging	58
6.3	Distribution of Diagnostics	59
7	Results	61
7.1	Rotating Plasma	61
7.2	Outflow Dynamics	64
7.3	Dimensionless Parameters and Scalability	66
8	Conclusions and Future Work	69

List of Figures

1.1	Cartoon of an Eulerian compression wave in the upstream frame of reference. The wave moves from left to right at a supersonic velocity (light blue arrow). As the shock moves forward, the fluid in the upstream (dashed line) enters into the shocked region (gray) and then into the downstream (dotted line).	5
1.2	Cartoon of an asymmetric blast wave. The continuous black line is the shock region, separating downstream and upstream. The gray arrows denote the velocity of the shock in certain points. The red and green arrows depict the direction of the temperature and density gradients, respectively.	8
1.3	Cartoon of the annular cutting a tomographic plane perpendicular to the target that contains the axial. a) The plasma (blue bubbles) is produced by the annular beam (red triangles) and expands as indicated by the small black arrows. b) At later times the plasma stagnates at the centre of the column (orange region), whereas the axial and radial propagation produces blast waves.	12
2.1	a) Schematic figure of the process of producing an annular laser beam. The laser beam propagates from right to left. First it enters the axicon prism with base angle θ_{ax} , then it is focused by the lens of focal length f onto a target at distance f from the lens. b) Image of an ablated surface after the beam has been focused onto it. .	15
2.2	Principle of shadowgraphy and schlieren imaging. a) Shadowgraphy and, b) schlieren.	17
2.3	Mach-Zehnder interferometer. Green arrows indicate the path of the laser beams as they pass through beam splitters (BS) and mirrors (M). a) Reference interferogram (<i>i.e.</i> no plasma in the path of the probing beam) and, b) probing interferogram. . .	18
2.4	Schematic of the first experimental set up. Each rectangle denotes the edges of three different optic tables. (a) Axicon prism, (b) focusing lens and (c) is the flat titanium target.	19
2.5	Schematic of the second experimental set up. Each rectangle denotes the edges of three different optic tables. (a) Axicon prism, (b) focusing lens and (c) is the flat carbon target, (d) is a spatial filter system to improve the quality of the diagnostics beam, (e) is a 50 cm focal length lens, (f) is the $\sim 620 \mu\text{m}$ diameter schlieren pinhole and (g) is an additional lens to set the focal plane on the plasma.	20

2.6	Diagram of the plasma-diagnostics synchronising system.	21
2.7	Schematic of the third experimental set up. Each rectangle denotes the edges of three different optic tables. (a) Axicon prism, (b) focusing lens and (c) is the flat carbon target, (d) is a spatial filter system to improve the quality of the diagnostics beam, (e) compensating glass and (f) neutral filter.	21
2.8	Magnetic field produced by NeFeB magnets. a) Topology of the magnetic field. Color code indicates the strength of the field, whereas the white arrows point in its direction. b) Numerical simulation (continuous line) and empirical data (purple dots) for the axial component of the field along the symmetric axis of the set-up. c) Numerical simulation (continuous line) and empirical data (pink dots) for the axial component of the field along the radial direction.	22
3.1	Set of images representative of the characteristic time evolution of the Ti plasma plume, as measured by its self-emission before $t = 600$ ns. a) Plasma propagating freely and, b) plasma in an static external field.	24
3.2	Set of images representative of the characteristic time evolution of the Ti plasma plume, as measured by its self-emission from $t \sim 600$ ns to ~ 4000 ns. a) Plasma propagating freely and, b) plasma in an static external field.	25
3.3	a) False color image of the Ti plasma plume at $t = 512$ ns. Two separate regions are identified and pointed with white arrows: the shock and the leading edge. The dotted line shows the approximate portion inspected using ImageJ to plot the intensity profile. b) Intensity histogram extracted from image. c) Trajectories of the shock in both free propagation and in the magnetic field and, d) trajectories of the leading edge in both free propagation and in the magnetic field.	26
3.4	a) False color image of the Ti plasma plume at $t = 137$ ns. The continuous white line shows the approximate position of the solid target, whereas the dotted line shows the approximate portion inspected using ImageJ to plot the intensity profile. b) Trajectories of the diameter of the plume in both free propagation and in the magnetic field.	28
3.5	Series of different shadowgraph images of the blast wave at $t = 265$ ns.	29
3.6	Shadowgraphy images of the experiment up to $t \sim 390$ ns. Time runs from left to right. The first row are all in 715 Torr background. Likewise, the second and third rows correspond to 250 Torr and 140 Torr, respectively. The red arrows point to the position of the central column.	30
3.7	Schlieren imaging of the annular plasma in 1 atm background Ar.	30
3.8	Shadowgraphy images of the experiment from $t \sim 500$ ns to $t = 1510$ ns. Time runs from left to right. The first row are all in 715 Torr background. Likewise, the second and third rows correspond to 250 Torr and 140 Torr, respectively. The red arrows point to the position of the emerging bubble, whereas the green arrows point to the planar front.	31

3.9	Shadowgraphy images of the experiment from $t = 2020$ ns to $t = 5010$ ns. Time runs from left to right. The first row are all in 715 Torr, the second row corresponds to 250 Torr and third row corresponds 140 Torr, background gas pressure. The green arrows point to the planar front.	32
3.10	Shadowgraphy images of the experiment at $t \sim 140$ ns. The first row shows results in free propagation, whereas the second with the external magnetic field. The red arrows point to the central column.	33
3.11	Shadowgraphy images of the experiment at $t \sim 500$ ns. The first row shows results in free propagation, whereas the second with the external magnetic field. The red arrows point to the central column.	34
3.12	Shadowgraphy images of the experiment at $t \sim 2000$ ns. The first row shows results in free propagation, whereas the second with the external magnetic field. The green arrows point to the planar front.	35
3.13	Trajectory profiles for the on-axis propagation of the blast wave.	36
3.14	Interferogram of the plasma plume at 388 ns in 0.3 atm Ar background. a) Experimental data and, b) one-pixel width path of the fringes.	37
3.15	Preliminary density maps (along the optical path) in 0.3 atm Ar background. a) Blast wave at $t = 137$ ns. The stagnation column, plasma downstream and neutral shocks are indicated by inlet arrows. Additionally the interpretation of the sign on the line density is provided. b) Blast wave at $t = 388$ ns and, c) blast wave at $t = 1010$ ns.	38
5.1	Schematic of the rotating Z pinch. The circular dotted contours are left for better visualisation. In a standard wire array: a) the wires are placed equally spaced, b) the magnetic contour is cylindrically symmetrical and, c) the implosion is purely radial. In the rotating Z pinch: d) the return posts are placed nearby the wires and angularly displaced by θ , e) the magnetic contour have a radial component and, f) the implosion is driven off-axis. g) Schematic depiction of the direction of the current through the wires and return posts.	45
6.1	Schematic image of the hardware. The red arrows indicate the path of the electrical current.	57
6.2	Schematic figure of the MCP principle of function. a) An image of the plasma onto the detection plate is formed, b) the ionising self emission produces photo-electrons on the detection plate, c) when the pulsed votage is applied, the initial photo-electrons are accelerated into the micro-channel producing an electron avalanche.	58
6.3	Schematic image of the diagnostics distribution inside the vacuum chamber.	60
7.1	Time evolution of the experiment probed by end-on optical self-emission.	62

7.2 Interferometric data for 532 nm wavelength probing beam. a) Raw reference interferogram and, b) one-pixel width path of the reference interferogram. c) Plasma interferogram and, b) one-pixel width path of the plasma interferogram. 63

7.3 Map of electron density probed by the 532 nm wavelength end-on laser beam. 64

7.4 Images from UV/XUV self-emission using a 70 μm pinhole diameter. 65

7.5 Images from UV/XUV self-emission using a 150 μm pinhole diameter. 65

7.6 Images from UV/XUV self-emission. (a) At $t = 276$ ns a straight highly collimated jet is observed. (b) At $t = 336$ ns the jet develops a kink shape. The green arrow points at the kink jet, whereas the blue arrow to the ablation streams surrounding the return posts. 66

List of Tables

- 1.1 Some examples of order-of-magnitude magnetic fields observed in nature and the spatial scales at which they are observed. 3

- 7.1 Extreme values for estimations of physical quantities. 67
- 7.2 Dimensionless parameter for the rotating flow (within array). 68
- 7.3 Dimensionless parameter for the outflow. 68

- 8.1 Fitting parameters for the axial propagation of the shock in free propagation (FP) and in the external magnetic field (MF). 71
- 8.2 Fitting parameters for the axial propagation of the leading edge in free propagation (FP) and in the external magnetic field (MF). 71
- 8.3 Fitting parameters for the radial propagation of the plume in free propagation (FP) and in the external magnetic field (MF). 72
- 8.4 Fitting parameters for the axial trajectory of the blast wave in free propagation (FP) and in the external magnetic field (MF) at different background pressure. . . 72

Part I

**Dynamics of Laser-Produced
Annular Plasmas**

Chapter 1

Introduction

In this chapter, I introduce a variety of apparently unrelated topics. I start by commenting on the biggest question that motivates this part of the thesis: where do magnetic fields found in the Universe come from? Although this may look as much larger issue than this work, as in fact it is, I intend to convince the reader that this question can be addressed by using laser-produced plasma experiments. In this regard, I next explain one mechanism that allows the generation of magnetic fields from initially unmagnetised media. Afterwards, I switch to explain blast waves, which represent an ideal environment to observe and control such mechanism. Later, I turn to laser-produced plasmas in general, including collisions amongst plumes, as a natural method to study blast waves. Finally, I explain the basic ideas behind laser-produced annular plasmas (the true scope of this work) and why they may result key to have a better understanding of many of the processes described above.

1.1 Our Magnetised Universe

A fascinating fact about the Universe is that magnetic fields are extremely ubiquitous. As shown in Table 1.1, they are present in every macroscopic spatial scales, spanning from ‘everyday’ ($\sim 10^0$ cm) to cosmological ($\sim 10^{25}$ cm) lengths [1, 2, 3, 4]. Where does this magnetisation come from? How do these fields *spark*¹ into existence? How do they grow and persist in time? How do they affect the evolution of structures throughout the Universe?

Even from the viewpoint of fields where these questions may not seem relevant, understanding the generation and evolution of magnetic fields is widely interesting, *e.g.* in Geophysics and Telecommunications (How does the Earth’s magnetic field affect the ionosphere? Accordingly, how does the dynamics of the ionosphere meddle with satellite signals?), Astrobiology and Planetary Exploration (How does the evolution of planetary magnetic fields shape the existence of life on planets -including our own-? Do they bring new sustainability requirements for humans inhabiting other planets?), amongst others.

¹I have admittedly quoted Francisco Suzuki-Vidal’s article on Nature Physics *How to spark a field* [5].

Context	Scale (cm)	Magnetic field (G)
Refrigerator magnets	$\sim 10^0$	$\sim 10^1$
Human brain	$\sim 10^1$	$\sim 10^{-9} - 10^{-8}$
Neutron star	$\sim 10^6$	$\sim 10^8 - 10^{15}$
Planets	$\sim 10^8 - 10^9$	$\sim 10^{-1} - 10^1$
The Sun	$\sim 10^{11}$	$\sim 10^{-1}$ (mean field)
Molecular clouds	$\sim 10^{21} - 10^{22}$	$\sim 10^{-2}$
Galaxies	$\sim 10^{21} - 10^{23}$	$\sim 10^{-9} - 10^{-6}$
Galaxy clusters	$\sim 10^{25}$	$\sim 10^{-6} - 10^{-5}$

Table 1.1: Some examples of order-of-magnitude magnetic fields observed in nature and the spatial scales at which they are observed.

Typically, systems having characteristic spatial scales larger than 10^6 cm are dynamically dominated by plasmas², as this state of matter is more abundant than solids, liquids and neutral gases. Therefore one might suspect that the physics of conducting fluids might lead to both the generation of magnetic fields and their amplification (or damping) via magnetohydrodynamical processes like diffusion, instability and turbulence. Plasmas in nature commonly behave as highly non-linear systems, thus in order to understand their complex evolution in ‘real-world scenarios’, laboratory experiments are key for developing insights, testing models and discovering new phenomena to address these fascinating questions.

In section 1.2 we discuss one process that triggers the appearance of magnetic fields from zero initial conditions, *i.e.* with no initial field, and briefly explain its interaction with other fluid-related phenomena to produce magnetic dynamos that amplifies and sustain the magnetic seeds.

1.2 The Biermann Battery

In 1950, Ludwig Biermann addressed the question of the generation of magnetic fields from zero initial conditions³ [6]. The derivation of his findings is straightforward and quite pedagogical, therefore it is worthwhile explaining it here (by admittedly following [8, 9]).

In the framework of two-fluid magnetohydrodynamics (MHD), we write the equation of motion for the electron fluid (in *cgs* units)

$$n_e m_e \dot{\mathbf{v}}_e = en_e(\mathbf{E} + \frac{\mathbf{v}_e}{c} \times \mathbf{B}) - \nabla p_e + \mathbf{f}_{i,e}, \quad (1.1)$$

²However, plasmas having solid-state-density are usually termed ‘warm dense matter’ and are treated as a different state of matter, provided the relevance of quantum mechanics in their microphysics.

³An extensive review of the origin of primordial magnetic fields in the Universe, termed *Magnetogenesis*, including physics far beyond the scope of this work, and their relevance in the formation of large-scale structures can be found in [7].

where n_e is the electron number density, \mathbf{v}_e is the velocity of the electron fluid element, \mathbf{B} the magnetic field, p_e the electron pressure and $\mathbf{f}_{i,e}$ the ion-electron momentum transfer term, e and c the electron charge and speed of light, respectively. Now, we take one simplification: take the inertia-less electron approximation, which is the smallest term⁴.

Furthermore, the collision amongst electrons and ions raises the electrical resistivity η and it is usual to write $\mathbf{f}_{i,e} = en_e\eta\mathbf{j}$, where $\mathbf{j} \approx en_e(\mathbf{u} - \mathbf{v}_e)$ is the current density and \mathbf{u} the mass velocity. By taking these approximations we find the Ohm law for the plasma

$$\mathbf{E} = -\frac{\mathbf{u} \times \mathbf{B}}{c} + \frac{1}{en_e} \frac{\mathbf{j} \times \mathbf{B}}{c} - \eta\mathbf{j} + \frac{\nabla p_e}{en_e}. \quad (1.2)$$

Thus, by introducing the Ampere law $\mathbf{j} = c\nabla \times \mathbf{B}/4\pi$ and Gauss law for the magnetic field $\nabla \cdot \mathbf{B} = 0$ (in *cgs* units) in the third term in the right-hand-side of equation (1.2) the induction equation due to the electron fluid is

$$\frac{\partial \mathbf{B}}{\partial t} = \nabla \times (\mathbf{u} \times \mathbf{B}) - \frac{1}{en_e} \nabla \times (\mathbf{j} \times \mathbf{B}) + \frac{\eta c^2}{4\pi} \nabla^2 \mathbf{B} + \frac{c}{en_e^2} \nabla p_e \times \nabla n_e. \quad (1.3)$$

In the right-hand-side of equation (1.3) we find the convective term, the Hall term, the diffusive term and the *Biermann battery*, respectively.

The latest term is the mechanism responsible for magnetising an initially unmagnetised plasma in which the gradients of both pressure and density in the electron fluid are non-parallel. In other words, by taking $B = 0$ the Biermann battery is the only non-vanishing term in the right-hand-side of (1.3), resulting in a non-trivial magnetic evolution. As we shall see in the next section, shocks within blast waves are ideal laboratories for producing non-parallel gradients in density and temperature (hence, pressure), and thus the Biermann battery is responsible for producing magnetic seeds.

Furthermore, by imposing $B = 0$ and introducing $p_e = k_B n_e T_e$, to incorporate the electron temperature T_e , the expression for the Biermann battery of an initially unmagnetised plasma is commonly written as

$$\frac{\partial \mathbf{B}}{\partial t} = \frac{k_B c}{en_e} \nabla T_e \times \nabla n_e. \quad (1.4)$$

Notice that this effect is produced as long as the electrons are decoupled from the ions, limiting the spatio-temporal regime at which it can operate, *i.e.*, within sufficiently short timescales the motion of electrons can produce a non-curl-free electric field. This fact is explicit when estimating the strength of the Biermann battery during the linear regime, as calculated by Schoeffle *et al.* [9]

$$B \approx \frac{k_B d_e}{L_n} \sqrt{4\pi n_e T_e}, \quad (1.5)$$

where $d_e = c/\omega_e$ is the electron inertial length ($\omega_e = \sqrt{4\pi n_e e^2/m_e}$ is the plasma frequency) and L_n is the characteristic length such as $\nabla n_e \sim n_e/L_n$.

⁴More rigorously speaking, this approximation is valid at the regime of slow-timescale evolution, so the acceleration of the fluid elements does not compensate the small numerical value of the electron mass.

The reader must be wondering in which scenarios the density and temperature gradients may be non-parallel. Before answer that question, in the following section, I will explain what blast waves are and how they might represent an ideal opportunity to produce magnetic seeds via the Biermann battery.

1.3 Blast Waves

When energy is released in a very short period of time, *i.e.* in timescales much shorter than dissipative processes, and also deposited in small spatial scales, *i.e.* the energy density is extremely high, an explosion termed *blast wave* takes place. The explosion acts as a super-fast piston injecting energy to the surrounding medium, where ‘super-fast’ means faster than the speed of sound of such medium. Therefore, the perturbation produced by the piston initiates a compressing traveling wave [10]. The supersonic compressing front travels through the medium in which it takes place resulting in a *shock wave*. In this section I will discuss the basic structure of a blast wave, in particular dissecting it in its three fundamental components: upstream, shock and downstream.

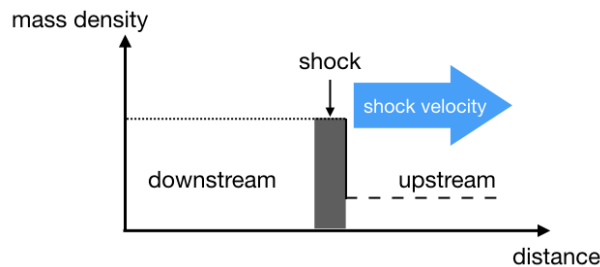


Figure 1.1: Cartoon of an Eulerian compression wave in the upstream frame of reference. The wave moves from left to right at a supersonic velocity (light blue arrow). As the shock moves forward, the fluid in the upstream (dashed line) enters into the shocked region (gray) and then into the downstream (dotted line).

Let us first consider a compression wave moving at u_s through a medium which has speed of sound c . The compressing wave separates the medium in two different regions. The *upstream* is the unperturbed medium ahead of the piston.

Notice that since the perturbation is supersonic, *i.e.* travels faster than the speed at which information can be carried through the fluid, then the compression produced by the piston will be sudden and violent. This leads to a sharp increase of density, termed *shock*. In terms of fluid equations, this shock determines the causality limit for information within the medium.

When the fluid enters the shocked region, it is heated up to a temperature such that after the process the shock is subsonic. The hot fluid behind the shock is termed *downstream*. Thus, the motion of the fluid elements in the frame of reference co-moving with the blast wave is always upstream, shock, downstream [10].

Blast waves and their properties are a fascinating field of research, but I intend not to enter

into so many details in this thesis, as elementary notions are sufficiently good to understand our experiments⁵.

Can the upstream be pre-heated by a shock?

This question is quite relevant in regards of pure gasdynamics and, at first glimpse, the answer seems to be no. Since the shock wave determines the boundary of acoustic causality, it is impossible for information to reach any fluid element in the upstream faster than the shock. One must conclude that the fluid must be heated only once the shock has carried it into the subsonic downstream, right? False (even neglecting radiative transfer), as I will illustrate using a very simple toy model.

Let us think of the shock as a flat rigid wall moving at constant velocity \mathbf{u}_s in a well defined direction and consider a thermal particle of mass m within the upstream moving at the speed of sound in the upstream c towards the shock, such that $c = u_s/M$, where $u_s = |\mathbf{u}_s|$, $c = |\mathbf{c}|$ and $M \equiv u_s/c$ is the Mach number of the shock. Notice that, in a Maxwellian distribution, this particle has the mean velocity of the population within the upstream, therefore its dynamics dominates the thermal part of the fluid evolution.

Now assume that the particle collides elastically against the shock, *i.e.* in the reference frame co-moving with the shock the particle incomes and outcomes with the same speed c , but in opposite directions. The kinetic energy of the particle in this frame of reference such as $K)_s = mc)_s^2/2$, then the elastic collision means $K_{in})_s = K_{out})_s$. In order to prevent ourselves from stacking a large number of subindices, I will denote the shock frame of reference using a right parenthesis as notation. Now, denoting an arbitrary velocity vector \mathbf{V} in the upstream frame of reference without the right parenthesis, such vector transforms in the shock reference frame as $\mathbf{V} = \mathbf{V})_s + \mathbf{u}_s$. Defining \mathbf{u}_{out} as the velocity of the particle after the collision in the upstream frame of reference and plugging everything in the energy balance, it yields

$$K_{out} = K_{in} + m[\mathbf{u}_{out} - \mathbf{c}] \cdot \mathbf{u}_s, \quad (1.6)$$

from which it is concluded that the particle increases its kinetic energy by $m[\mathbf{u}_{out} - \mathbf{c}] \cdot \mathbf{u}_s > 0$. Hence, after the collision the particle has speed $u_{out} = c(M + \sqrt{1 + M^2}) > c$. Furthermore, notice that $u_{out} > u_s$ by a factor $1 + \sqrt{1 + M^2}/M$. Therefore, the interaction of the shock with the thermal particles within the upstream can interact elastically, in such a way that they return as non-thermal particles into the upstream. Through collisions they, in turn, can deliver their kinetic energy into the upstream, pre-heating it *without violating causality*. This hot upstream is termed *precursor*, because from the standpoint of an observer co-moving with the upstream, the precursor precedes the shocked region [11].

⁵Two amazing texts that I can recommend to get into this topic are Zel'dovich's (2002)[10] and Drake's (2006) [44] books.

1.3.1 Solutions

The time evolution of the blast wave depends on initial energy density, the medium through which it is propagating and the symmetry of the explosion. Now I will describe the solutions for the equation of motion of blast waves relevant to this thesis. As the reader might imagine, it exists a plethora of studies regarding blast wave solutions, given that many of them hold military applications, thus by no means the following should be understood as an extensive review⁶.

Ballistic solution

The simplest solution imaginable appears when the ram pressure is much lower than the momentum density of the shock, thus the pressure exerted by the upstream is negligible, *i.e.* $\dot{\mathbf{u}}_s = 0$. This leads to a uniform trajectory of the shock termed *ballistic propagation* with the general form

$$\mathbf{r}(t) = \mathbf{u}_{s0}t + \mathbf{r}_0, \quad (1.7)$$

where \mathbf{u}_{s0} is the constant shock velocity and \mathbf{r}_0 is the initial position. This solution is valid whenever the mass of the shock is much higher than the mass of the upstream [12].

Drag model

Let us now consider a situation in which the shock velocity is dragged by the background gas⁷. Such situation can be described by a simple model in which the strength of the drag is proportional to the velocity of the flow, *i.e.*

$$\dot{\mathbf{u}}_s = -\beta\mathbf{u}_s, \quad (1.8)$$

where β is a proportionality constant termed *dragging coefficient*. Equation (1.8) is easy to solve and has a general solution

$$\mathbf{u}_s(t) = \mathbf{u}_{s0}e^{-\beta(t-t_0)}, \quad (1.9)$$

where \mathbf{u}_{s0} is the initial velocity of the shock and t_0 is the reference time (which without loss of generality can be set to zero). Integrating the latter equation in time and with a little algebra one finds the trajectory of the shock being

$$\mathbf{r}(t) = \mathbf{r}_s (1 - e^{-\beta t}) - \mathbf{r}_0, \quad (1.10)$$

where $\mathbf{r}_s = -\beta^{-1}e^{\beta t_0}\mathbf{u}_{s0}$ is termed the *stopping distance* and \mathbf{r}_0 in practice is an adjustment parameter in which one incorporates the temporal difference between the initial formation of the plasma and its detection in a timing signal [18].

⁶An educated reader might notice that I do not consider the very famous Sedov-Taylor solution that models the blast wave resulting from a strong point explosion [10]. Due to the spatial extension of an annular plasma this solution will not be relevant in the context of this thesis.

⁷This can be extended to a solvable *turbulent* drag in which friction is $\propto v^2$. However, the model drag model will prove sufficiently good in Chapter 3.

1.3.2 The relation of the Biermann battery and asymmetric shocks

Up until now, two important results should have stuck with the reader: one is that the Biermann battery can operate only when density and temperature gradients are non-parallel and, the second is that blast waves provides with jumps in density termed shocks. It should be rather obvious why these two different things might be related: a blast wave with a temperature gradient along its shock has non-parallel temperature and density gradients!⁸ As shown in Figure 1.2, an asymmetric shock is an ideal laboratory to study the Biermann battery, as has been studied by Eleanor Tubman, *et al.* (2017) [12]. Therefore, being able to produce and control the properties of such asymmetric shocks with high degree of reproducibility might be key to understand the magnetisation present in our Universe.

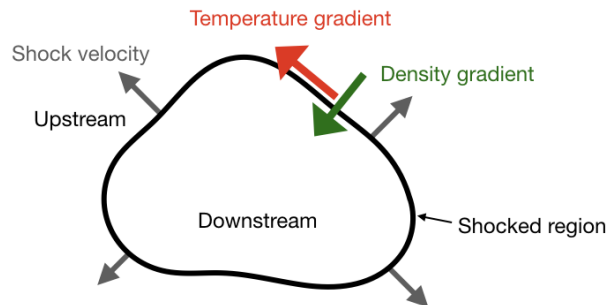


Figure 1.2: Cartoon of an asymmetric blast wave. The continuous black line is the shock region, separating downstream and upstream. The gray arrows denote the velocity of the shock in certain points. The red and green arrows depict the direction of the temperature and density gradients, respectively.

This idea is at which this thesis distantly aims for. High-power laser beams are an excellent method to produce energetic blast waves, as they can carry an important amount of energy and deliver it in fs to ns timescales, resulting in power densities much higher than 10^9 W/cm². I will now turn into such kind of experiments and explain what shocks can be produced in that context.

1.4 Laser-Produced Plasmas

In this part I discuss an efficient way to produce blast waves: high-intensity laser beams, in particular the effect that they have on solid targets. Firstly, I explain very briefly the way that they produce a rapid ionisation of the medium in which they are focused, in order to produce unmagnetised plasmas. During the next two sections I will regard the most basic effects of external magnetic fields and some aspects of experiments studying collisions between these plasmas.

The fundamental idea behind laser-produced plasmas is the fact that electrons in a material

⁸This does not prevent that there might be components of the temperature gradient parallel to the density gradients, however these components will not contribute to the battery.

can gain energy from light. This can happen within two different scales: either they interact as quantum (electron-photon) or as classical entities (electron-electromagnetic wave).

On the one hand, quantum interactions are usually dominant when the breakdown is in its initial stages, as the electrons are bounded to the atoms and/or molecules of the material. On the other hand, classical effects are important when the initial electrons are gaining energy from the electromagnetic wave and producing ionisation by electron-neutral and electron-ion collisions.

If the energisation of the electrons of the material is sufficiently large, the material will become an ionised gas (a plasma). The criterion to evaluate the production plasmas by illuminating target is generally given by the observation of the characteristic glow of the plasma. There are multiple interplaying processes that can lead to the ionisation of a medium and consequent plasma formation, by light-matter interaction [13], which I will very briefly summarise:

- i) *Resonant ionisation* occurs when a bounded electron with ionisation energy $E_i = h\nu$ gains energy by absorbing a single photon of frequency ν .
- ii) *Multi-photonic ionisation* (MPI) is a key effect when the energy per photon of the laser is insufficient to ionise the atom. During the MPI the bounded electrons gain energy from $m \geq E_i/h\nu$ photons, thus reaching the regime of continuum energies.
- iv) *Laser-induced heating* is the energy transfer from the laser to the material within a layer of a given thickness. If sufficient energy is delivered to the target faster than the typical diffusion times, it will rapidly vaporise.
- iii) *Electron-neutral and electron-ion inverse bremsstrahlung collisions* are the combination of two separate effects. Electron-neutral collisions bremsstrahlung collisions dominate up to temperatures $\sim 10^4$ K, initial electrons gain energy from the laser by inverse bremsstrahlung and then deliver part of their energy to the electrons in atoms and molecules in the vapor. As temperature increases, absorptivity does too, leading to the electron-ion version of this process, where both ions and electrons gain energy from the laser. If the rate of ionising collisions overcomes the recombination rate, then an electron cascade growth takes place, forming a plasma.

Thus, once the target has been illuminated a rapid vaporisation of the surface of the material takes place. This is because, in the case for both materials used in this work, titanium and graphite, the absorption of the radiation by target occurs at short lengths. Therefore, it is common that the diffusion length is much larger than the absorption length. During the breakdown of the material, the increase in temperature ΔT is

$$\Delta T = \frac{2\alpha I}{K} \left(\frac{\chi t}{\pi} \right)^{1/2}, \quad (1.11)$$

where α is the metal absorptivity, I the irradiance (*i.e.* energy flux), K thermal conductivity t the pulse width and χ thermal diffusivity [13] which is associated to thermal dissipation within the heat equation.

After the vaporisation, ionisation occurs, leading to the formation of an plasma expanding as a *plume*. In a low-enough irradiance regime such that two-species effects, e.g. Biermann battery, can be neglected during the breakdown, this plume will be unmagnetised. The deposition of energy acts in a similar way as a detonation, therefore the plume acts as piston pushing the ambient medium, producing a blast wave [13].

1.4.1 Magnetic confinement effects in laser-produced plasmas

Effects of external magnetic fields in unmagnetised plasmas can be regarded as a multiscale problem. The most fundamental is the change in the motion of the charged particles within the plasma, as helix trajectories termed *gyro-orbits*⁹ are imposed by the magnetic field to those particles. The second, macroscopic approach to this problem deals with the effects of the magnetic field onto a conducting fluid. I now analyse in the simplest cases both different scales.

Single particle confinement effect in a static, uniform magnetic field

In the absence of electric and gravitational fields, a particle within the plasma with charge q , mass m and initial velocity \mathbf{v}_0 trapped in a homogeneous, static magnetic field \mathbf{B} has equation of motion in *cgs* units

$$\dot{\mathbf{v}} = \frac{q}{mc} \mathbf{v} \times \mathbf{B}. \quad (1.12)$$

Taking the common decomposition $\mathbf{v} = \mathbf{v}_{\parallel} + \mathbf{v}_{\perp}$, where $\mathbf{v}_{\parallel} \cdot \mathbf{B} = v_{\parallel} B$ and $\mathbf{v}_{\perp} \cdot \mathbf{B} = 0$, one can solve the differential equation (1.12) for the components of \mathbf{v} to find

$$\mathbf{v}_{\parallel} = \mathbf{v}_{\parallel 0}, \quad (1.13)$$

$$\mathbf{v}_{\perp} = \mathbf{v}_{\perp 0} \left[\sin\left(\frac{qB}{mc}t\right) + \cos\left(\frac{qB}{mc}t\right) \right]. \quad (1.14)$$

Which are the parametric components of a helix whose centre follows the magnetic field direction with constant velocity \mathbf{v}_{\parallel} . This is why the magnetic field is termed *guiding field* in many contexts, such as tokamak physics. Notice that the system has a characteristic frequency $\omega_g = |q|B/mc$ termed *gyro-frequency*. As opposed to the rectilinear free propagation of the charged particle, the magnetic field traps it in an orbit with *gyro-radius*

$$R_g = \frac{mc}{|q|B} v_{\perp}, \quad (1.15)$$

which can be found by solving (1.14) or simply using known relations from Newtonian mechanics. This is the first, simplest magnetic *confinement* effect found in plasma physics, as the magnetic field restricts the motion of the charged particles at characteristic spatial scales of R_g .

⁹They are sometimes called Larmor orbits in the framework of plasma physics. However, rigorously speaking, the period of a gyro-orbit is exactly half as the Larmor orbit. Therefore I avoid the use of that misleading terminology here.

Magnetic confinement in single-fluid MHD

The second regime at which one can easily see confinement effects is in fluid mechanics. Let us write the single-fluid MHD equation of motion, but consider just magnetic and pressure effects, *i.e.*

$$\frac{d}{dt}(\rho\mathbf{u}) = -\nabla p + \frac{1}{4\pi}(\nabla \times \mathbf{B}) \times \mathbf{B}, \quad (1.16)$$

where ρ is the mass density, \mathbf{u} the macroscopic velocity field, p the fluid pressure field and \mathbf{B} the magnetic field. The last term in the right-hand-side of equation (1.16) can be expanded, leading into two terms. Working them out one finds magnetic corrections to the thermal propagation dynamics given by

$$\frac{d}{dt}(\rho\mathbf{u}) = -\nabla p - \nabla \left(\frac{B^2}{8\pi} \right) + \frac{1}{4\pi}(\mathbf{B} \cdot \nabla)\mathbf{B}. \quad (1.17)$$

Notice that the second term in the right-hand-side of equation (1.17) is analogue to a pressure exerted on the fluid, therefore we define $p_M \equiv B^2/8\pi$ as the *magnetic pressure* and acts in the exact same manner as a fluid field forcing the motion of the plasma. The third term, which is proportional to magnetic field gradients is termed *magnetic tension*. This tension is raised from changes in the direction of the magnetic field, *i.e.* curvature of the field lines, thus it is usually illustrated as the magnetic lines acting of ropes containing the plasma.

Up until now I have neglected the fact that the fluid might dynamically affect the external magnetic field. This is indeed a strong assumption. However, when plasmas such that the dissipation due to resistivity cannot be neglected, *i.e.* their macroscopic characteristic timescales are long compared to dissipation timescales, any externally imposed static field escapes the motion of the plasma in a process termed *magnetic diffusion*. This will be better understood in Part II when discussing the induction equation and the Reynolds magnetic number.

1.4.2 Colliding plumes in laser-produced plasma experiments

The idea of colliding laser-produced plasmas is not new and research centred on this topic can be traced back to 1974 [14], having many possible applications such as laboratory studies of shock waves, pulsed laser deposition, X ray sources, amongst others.

The interaction between two counter-propagating plumes can be broadly categorised in two classes: firstly, they can produce *stagnation*, *i.e.* they are rapidly decelerated forming a dense stagnation-layer and turning their macroscopic kinetic energy into heat (and subsequently, radiating energy); or secondly, they can interact weakly in a process termed *interpenetration*.

These two scenarios can be rigorously separated by defining the *collisionality parameter* ξ ,

$$\xi \equiv \frac{D}{\lambda_{ii}}, \quad (1.18)$$

where D is the separation of the plasmas and λ_{ii} is the mean free path for binary ion-ion collisions. *Hard stagnation* is achieved when $\xi \gg 1$, *soft stagnation* when $\xi \sim 1$ and interpenetration when $\xi \ll 1$.

In order to design experiments of interacting plumes one must take a look at the functional form of λ_{ii} for taking into account what material and/or configuration is appropriate. Relevant to the experiments presented in this thesis, the mass of the ions within the plasma is roughly the same m_i , *i.e.* both plumes are composed by the same chemical element, and 1 and 2 denote two counter-propagating plumes.

$$\lambda_{ii} = \frac{m_i^2 v_{1,2}^4}{4\pi e^4 n_e Z^4 \Lambda}, \quad (1.19)$$

where $v_{1,2}$ is the relative speed amongst the plumes, Z is the effective charge state of the plasma, n_e is the electron number density and $\Lambda \equiv \ln(12\pi e^{-3}(\epsilon_0 k_B T)^{3/2} n^{-1/2})$ is the Coulomb logarithm for binary collisions [41].

A particularly relevant result is that, if stagnation is obtained in the process, then the collision is inelastic. This means that the particles within both plumes randomise its macroscopic momentum, turning it into heat. Thus, the stagnation layer has a temperature higher than both plumes.

1.4.3 Laser-produced annular plasmas

As opposed to focusing the laser beam as a spot on a flat target, F. Veloso *et al.* (2006, 2009) [15, 16] and L. M. Cabalín & J. J. Laserna (2004) [17], studied the plasma plume produced by an annular beam. The means by which one can produce ring-shaped laser beam will be reviewed in the next chapter. I now explain the basic dynamics of such experiments, which were carried up until very early times of its evolution $t \sim 100$ ns.

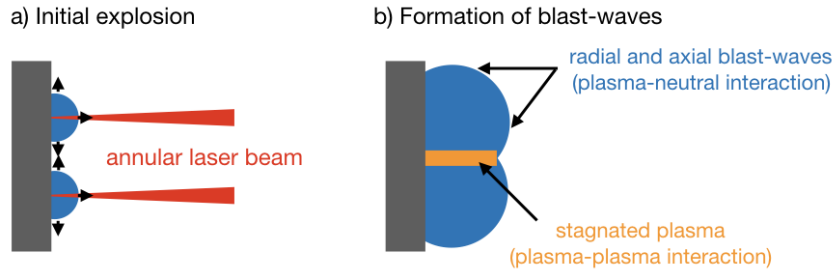


Figure 1.3: Cartoon of the annular cutting a tomographic plane perpendicular to the target that contains the axial. a) The plasma (blue bubbles) is produced by the annular beam (red triangles) and expands as indicated by the small black arrows. b) At later times the plasma stagnates at the centre of the column (orange region), whereas the axial and radial propagation produces blast waves.

As illustrated in Figure 1.3, the plasma starts its expansion as a free gas due to the ablation of the solid target. In the meantime, the portion of the plasma expanding outwards sweeps the background gas producing blast waves. However, the inwards propagation collides in the middle, stagnating and producing a hot column of shocked plasma. This hot column proceeds to keep expanding axially as a jet-like structure. In high-pressure background experiments the annular plasma can be regarded as a piston pumping energy into the neutral background gas.

This experiment is particularly interesting because it combines three shock wave experiments at once, even without the *a priori* interest in magnetisation processes. Nonetheless, notice that resulting from the stagnation process, the central column has to have higher temperature than the rest of the blast wave where no plasma-plasma interaction occurs. Therefore, the central part of the axial blast is expected to be hotter than the radial part of the blast wave, leading to the formation of an asymmetric shock in the long run. This is, in fact, a very nice prospect, because in principle it is possible to control the production and strength of the Biermann battery along this asymmetric shock from an initially unmagnetised plasma with extremely high reproducibility, because the localised increase in temperature is imposed by controlled dynamics: stagnation, rather than other uncontrollable mechanisms such as beam inhomogeneities. To the best of my knowledge, there are no reports on the later time dynamics of these blast waves nor their properties.

1.5 Summary

Above I explained a number of topics and the key concepts inhabiting them. Thus, I started by motivating this thesis in the frame of addressing the origin of magnetic fields in the Universe. I presented one mechanism which finds its origin in two-fluid magnetohydrodynamical phenomena when the conducting electron fluid has non-parallel gradients in electron temperature and gradients, termed Biermann battery. This effect is produced by gradients in the momentum flux of the electrons, producing electric fields that are not curl-free. Thus, the induction equation delivers a non-trivial time evolution of the magnetic field, producing magnetisation of the initially unmagnetised medium. The non-trivial evolution requires, however, that the gradients in density and temperature are non-parallel.

This peculiar configuration can be achieved using asymmetric blast waves, which are supersonic compressing waves that are produced after transient strong detonations. They are in fact ideal environments to produce, control and study the Biermann battery. Any given blast wave can be decomposed in three broad regions: the upstream, *i.e.* the subsonic fluid that is swept by the blast wave; the shock, *i.e.* a steep density jump produced by the compressing wave that heats the fluid from the upstream and; the downstream, which is the after-shock region.

Due to the shock defining a density jump parallel to the motion of the compressing wave, temperature gradients perpendicular to this direction are, by definition, perpendicular to the density gradient produced by the blast wave. Therefore, in a way blast waves maximise the operation of the Biermann battery because the temperature and density gradients are, ideally, perpendicular. Therefore, the challenge is to experimentally produce and control asymmetric blast waves.

Laser-produced plasmas since they are a feasible way of producing unmagnetised blast waves, since the plasma plume typically represents supersonic fluids propagating through the background gas in a vacuum chamber, shocking it. Additionally, by using two or more counter-propagating plasma plumes, the blast waves controlled via stagnation or interpenetration processes. Further modifications on the dynamics of plasmas can be achieved by imposing external magnetic fields,

as the induce trapping and guiding effects of the particles in helical gyro-orbits, together with magnetohydrodynamical confinement effects such as magnetic pressure and magnetic tension over the fluid.

Finally I explained the central object of study in this work: laser-produced annular plasmas, which can be used to produce and control asymmetric blast waves, through the stagnation within the centre of the annular plume, heating the central part of the shock wave.

Thus, the goal of this thesis is to characterise the dynamics of the annular plasma. By describing qualitatively the time evolution of the blast wave and setting limits on the ‘life expectation’ of the asymmetry of the blast wave. Thus, it is necessary to put constraints on characteristic timescales up to which the asymmetry is mitigated by heat transport, or the plasma has become cold and slow enough so that there is no longer an ionised shock, therefore stopping the Biermann battery effect.

It is expected that the plasma primarily fulfills the role of the supersonic piston that drives the shock formation. Thus, it is very important to quantify the macroscopic characteristic, lengths, velocities (hence timescales) that rule the system. Imaging of the plasma allows us to study density jumps in the upstream-shock-downstream direction, giving us information of the species that inhabit those three regions. This is extremely relevant, as the Biermann battery can only operate in conducting media. Furthermore, as the plasma acts as a piston, it is expected to dominate the downstream which has been observed to contain the stagnation column. Thus, the characterisation of this region is key to understand its implications on the shock.

Regarding the perpendicular direction, *i.e.* along the shock, the asymmetry becomes relevant. Any asymmetry on the evolution of the blast wave in principle is observable in two indirect ways. Firstly, changes of morphology indicate that there must be temperature gradients that can sustain the asymmetry of the blast wave. Here it is important that the transport rates are much smaller than the macroscopic rates. Additionally, these observations can also be benchmarked indirectly by differences in the self-emission of the plasma. If the radiation attributed by *bremstrahlung* of the macroscopic flow can be neglected, then the radiance of the plasma is expected to be related with temperature. In order to fulfill this hypothesis, a characterisation of the evolution of the downstream and shocked regions in terms of self-emission is necessary.

Chapter 2

Experimental Set-up

In this chapter, I explain the experimental methods by which we produce annular laser-produced plasmas and those for probing it. Regarding the latter, we used two families of methods: self-emission diagnostics, which allow us to obtain time-resolved imaging of the electromagnetic radiation generated by the plasma and, refractive diagnostics, which use low intensity lasers to map differences in the refractive index of the plasma, thus extracting both qualitative and quantitative information. Together with these rather general notions, at the end of the chapter I will describe the diagnostics spatial distribution and synchronisation protocol between the plasma and the probing to run the experiments.

2.1 Annular Laser Beams

As reviewed in the last chapter, high-intensity light can produce ionisation in solids, thus producing a plasma by rapid ablation. As opposed to other works focusing laser beams onto a micron-scale spot, our set up combines an axicon prism and a converging lens to focus a ring-shaped laser spot onto a solid target [15, 17, 18].

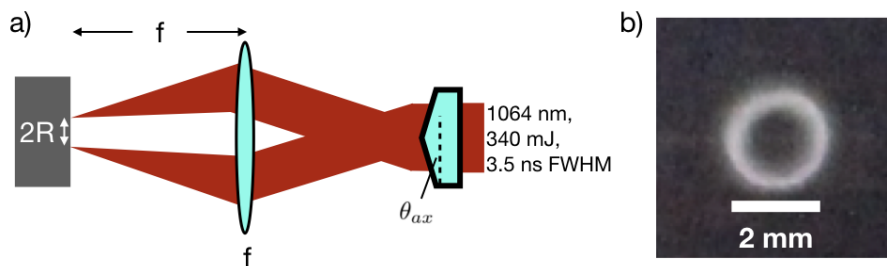


Figure 2.1: a) Schematic figure of the process of producing an annular laser beam. The laser beam propagates from right to left. First it enters the axicon prism with base angle θ_{ax} , then it is focused by the lens of focal length f onto a target at distance f from the lens. b) Image of an ablated surface after the beam has been focused onto it.

An axicon prism is a cone-shaped crystal [19] that produce an annular beam, which when focused with a converging lens of focal distance f , then the ring has radius R given by [16]

$$R = f \tan(\theta_{out} - \theta_{ax}), \quad (2.1)$$

where θ_{ax} is the axicon base angle as measured in radians and θ_{out} is determined by the Snell law $n_{ax} \sin(\theta_{ax}) = n_{air} \sin(\theta_{out})$, where n_{ax} and n_{air} denote the refractive indices of the axicon prism material and air, respectively. By considering $n_{ax} \approx 1.5$ and $\theta_{ax} \ll 1$ the equation above can be expressed as¹

$$R \approx f \frac{\theta_{ax}}{2}. \quad (2.2)$$

2.2 Principles of Diagnostics

In this section I will explain the methods for characterising the macroscopic flow of the fluids within the experiment (both ionised and neutral) and the densities both for neutral and electron gases.

2.2.1 Intensified Charged Coupled Device

The most straightforward non-perturbative way of measuring something is by, literally, *looking* at it. In the context of high-energy-density experiments this means imaging based on the light emitted by the plasma, typically using a charge coupled device (CCD).

A CCD is an array of micron-scale detectors termed *pixels* whose size determine the resolution of the image, whereas the size of the array determines the size of the image. Each pixel typically consists in a semiconductor that delivers a signal whenever a sufficiently intense light interacts with it.

An intensified CCD (ICCD) uses an optic intensifier in front of a CCD to increase the gain of the device, which both increases the effective gain and acts as a shutter. By using a pulsed voltage signal, this allow to obtain time-resolved imaging of the plasma. In the experiment we used an Andor camera operated using a square 50 ns, 5 V electric pulse generated by a pulse generator. The ICCD employed in the experiments has an set of lenses designed to focus and magnify the image projected onto the intensifier.

2.2.2 Shadowgraphy & schlieren imaging

Consider an electromagnetic wave traveling through an inhomogeneous medium, i.e. it has a spatially varying refractive index $\mu = \mu(\mathbf{r})$, then the wave vector will change direction along its path. The *refractive* diagnostics use this fundamental fact to inspect the plasma using low intensity laser beams, as it will deviate from a rectilinear trajectory when passing through such plasma [20]. As we shall see in the next section, the refractive index field is dominated by the distribution of electrons within the plasma.

¹This limit is not generally true. However, the $\theta_{ax} \sim 10^{-2}$ rad for the prisms utilised in this work.

The principle behind the *shadowgraphy* image is illustrated in Figure 2.2a). When the well-collimated probing beam passes through the plasma it is deviated according to the discussed above, generating intensity variations onto the detection plane. In terms of the depiction, this is equivalent to converging arrows increasing the luminosity in the image and, diverging arrows decreasing it.

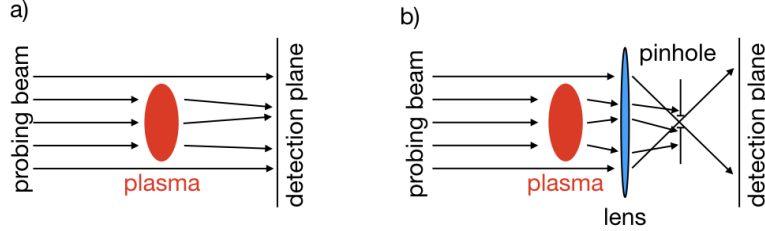


Figure 2.2: Principle of shadowgraphy and schlieren imaging. a) Shadowgraphy and, b) schlieren.

The relative change in intensity, *i.e.* the ratio between the change of intensity ΔI and the intensity of the incoming probing beam I_0 , is very well described in the literature [20] and it is proportional to the distance between the plasma and the detection plane L and the integral of the laplacian of the refractive index along the path of the beam, *i.e.*

$$\frac{\Delta I}{I_0} = L \int dl \cdot \nabla^2 \mu. \quad (2.3)$$

As a consequence of this process, in the detection plane one captures an image of the plasma whenever the laplacian (second derivative) of the refractive index is large enough. However, imagine a plasma such that its refractive index grows linearly in one direction and each plane perpendicular to that given direction has a constant refractive index. Such plasma would be *invisible* in the shadowgraph, since there is no concavity in its refractive index. Schlieren solves that issue incorporating a converging lens and a pinhole between the object and detection planes, as shown in Figure 2.2b).

Notice that the effect of the combination of lens and pinhole is to allow certain rays to pass through and reach the detection plane. Hence, any given ray that is stopped by the pinhole will appear as a black point in the image. More rigorously speaking, a well constructed schlieren set-up acts as a *spatial filter*, removing high-frequencies from the image. In this regard, it is an optimal technique to detect borders (filled with the higher Fourier orders) and it can be demonstrated that it is sensitive to the first derivative of the refractive index. Thus, it is an excellent method to detect and track shock waves².

2.2.3 Interferometry

Interferometric techniques are used in a large variety of fields for its high sensitivity. Just to name a few, two historically notorious experiments have used interferometers: the Michelson-Morley

²As can be appreciated in the beautiful book by Milton Van Dyke *An Album of Fluid Motion* [21].

experiment (1887), which found that the relative motion of the Earth with respect to the hypothesized ether was zero (leading to drop the theory of ether and support special relativity) [22] and the Advanced Laser Interferometer Gravitational-Wave Observatory (LIGO), which reported the direct measurement of gravitational waves from merging black holes in 2016 [23]. The fundamental principle behind all these techniques lies in the combination of two coherent light beams (*i.e.* lasers) having a given relative phase. If the electric fields of two monochromatic waves are given by $\mathbf{E}_1(\mathbf{r}) = \mathbf{E}_{01}(\mathbf{r})e^{i\omega t}$ and $\mathbf{E}_2(\mathbf{r}) = \mathbf{E}_{02}(\mathbf{r})e^{i\omega t + \phi}$, then the intensity in a given plane is [20]

$$I(\mathbf{r}) = E_{01}^2 + E_{02}^2 + 2E_{01}E_{02}\cos(\phi), \quad (2.4)$$

where $E_{0i} = |\mathbf{E}_{0i}|$ ($i = 1, 2$) and the latest term is modulated by the phase. In order to produce interfering beams we used a modified Mach-Zehnder interferometer. The modifications do not affect its functioning, therefore explaining a standard Mach-Zehnder interferometer is enough.

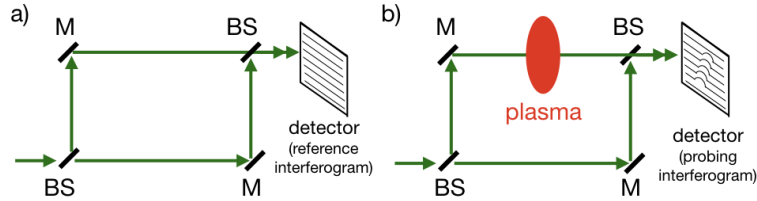


Figure 2.3: Mach-Zehnder interferometer. Green arrows indicate the path of the laser beams as they pass through beam splitters (BS) and mirrors (M). a) Reference interferogram (*i.e.* no plasma in the path of the probing beam) and, b) probing interferogram.

As it is shown in Figure 2.3, an incoming beam is split in two ‘legs’ of the interferometer: the *reference* and the *probing* beams. The former usually travels outside the vacuum chamber, whereas the latter passes through the portion in which the plasma will be. The interferometric technique requires two separate images formed in the detection plane. The reference interferogram is taken with no plasma and it sets a pattern given by the phase imposed by difference in the physical path across the two legs of the interferometer. The probing interferogram is taken when the plasma is on the path of the probing beam. If it has a refractive index differing from unity, then it will add to the total phase between the reference and probing beams. This will be observed as a fringe shift in the probing interferogram when comparing with the reference image. This phase shift is given by [20]

$$\Delta\phi = -\frac{\pi}{\lambda n_c} \int dl \cdot n_e, \quad (2.5)$$

where λ is the laser wavelength, $n_c \equiv \pi m c^2 / e^2 \lambda^2$ (in *cgs* units) is the cutoff density and n_e is the electron density, which sets the upper limit of detection of this technique. Any plasma having electron density $n_e \geq n_c$ is opaque to the incident wave, therefore if that is the case, the fringes are lost in the interferogram. The lower limit of this diagnostic is given by the un-noticed shift of fringes.

In practice, given the path of a ray within the output beam of the interferometer there will be a phase shift given by (2.5), since each portion of the probing beam passed through a given n_e . Resulting from this change in the relative phase, the intensity pattern is changed satisfying equation (2.4), thus the fringes in the interferogram change position with respect to the reference interferogram. By assuming certain symmetry of the system, it is possible to extract n_e from the integral in equation (2.5), thus finding a map of electron density [20, 24, 25].

2.3 Spatial Distribution of the Experiment & Synchronisation

During the development of this thesis, the experimental set-up used in this thesis changed dramatically. No less than three different spatial distribution for side-on probing of the plasma were used, all improving upon the previous set-up.

The first configuration is shown in Figure 2.4. The diagnostics set-up was inherited by previous investigations in the Plasma Group and had a set of detectors, such as a spectrometer and Faraday cups that were not used during this thesis. The 1064 nm, 3.5 FWHM laser beam is produced by an EKSPILA NL 301D/SH Nd:YAG laser, redirected by two mirrors (denoted by M in the following figures), through the axicon prism ($\theta_{ax} = 20$ mrad) and the redirected and focused onto a Titanium target sitting inside the vacuum chamber through a 50 cm focal length converging lens.

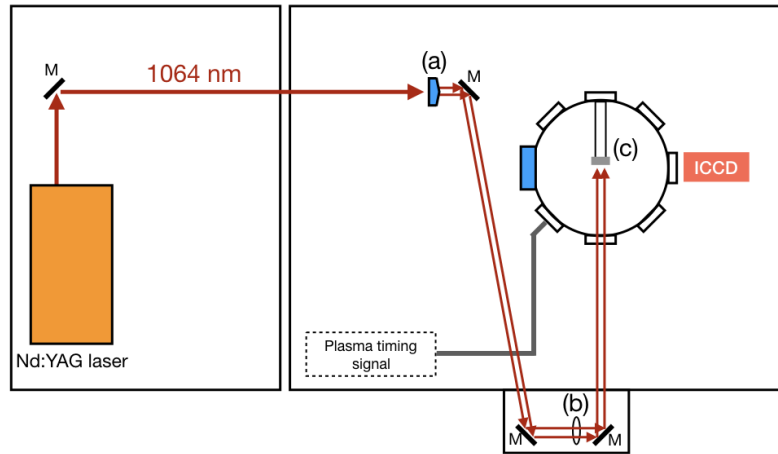


Figure 2.4: Schematic of the first experimental set up. Each rectangle denotes the edges of three different optic tables. (a) Axicon prism, (b) focusing lens and (c) is the flat titanium target.

Notice that configuration allows to have side-on inspection of the plasma. In this set-up the infrared laser operates at 10 Hz controlled by an external circuit. The plasma timing signal is obtained through an optic fiber pointing at the spot where the plasma is produced, with no additional optical systems. Once the light is captured by the fiber, it is transmitted to a photomultiplier biased at ~ 0.7 kV and connected to the oscilloscope. In the meantime the external

circuit sends a second signal with a given delay to the pulse generator. By turning both the knobs of the external circuit and the pulse generator the user can control the timing at which the image is taken by the ICCD. The signal of the pulse generator is registered by the oscilloscope. Spatially-wise, the pix-mm relation is calibrated by taking an image of an illuminated ruler, and then measuring the intensity profile of the notches on the ruler using ImageJ.

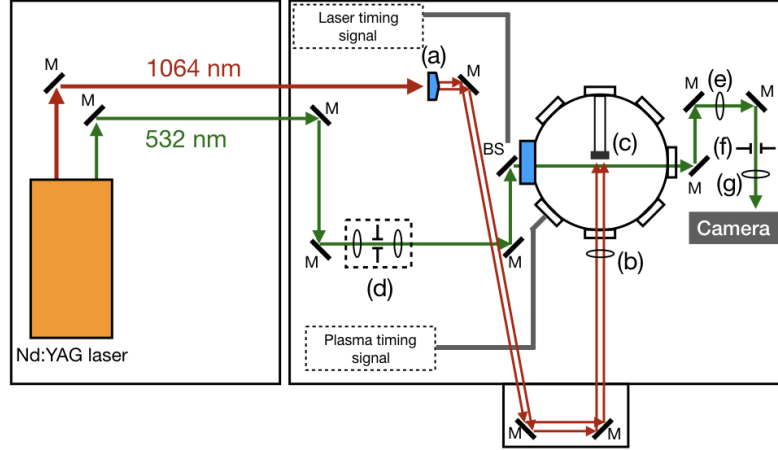


Figure 2.5: Schematic of the second experimental set up. Each rectangle denotes the edges of three different optic tables. (a) Axicon prism, (b) focusing lens and (c) is the flat carbon target, (d) is a spatial filter system to improve the quality of the diagnostics beam, (e) is a 50 cm focal length lens, (f) is the $\sim 620 \mu\text{m}$ diameter schlieren pinhole and (g) is an additional lens to set the focal plane on the plasma.

As stated above, the second set-up improves upon the first one. During the experimental campaign of 2017 two main modifications were implemented. Firstly, the incorporation of schlieren as a method for detecting the shock waves in the experiments and, secondly, a new synchronising system independent from any external circuits.

For diagnostics, the second harmonic (532 nm, 3.5 ns FWHM) from the Nd:YAG laser was used. As shown in Figure 2.5, the diagnostics beam passes through a spatial filter to improve the quality of the beam and then enters the vacuum chamber via a beam splitter. The transmitted beam is used as a timing signal, which is collected by an optic fiber and converted into a voltage signal with a biased photodiode DET110A/M (see Figure 2.6). The reflected beam is used to probe the plasma, and afterwards passes through a 50 cm focus-length converging lens at 50 cm from the plasma. Then the beam is focused through a $620 \mu\text{m}$ pinhole, passes through a second lens whose objective is to focus the spot into the camera placed in the detection plane.

The synchronisation system was upgraded for the second set-up onwards. As depicted in Figure 2.6, the protocol has two ‘knobs’ by which the user controls the timing of the refractive diagnostics respect to the plasma. After the system is triggered, the laser delivers a signal towards the oscilloscope. As this is the most reliable, consistent signal it is used to trigger the oscilloscope. Delay 1 sets the temporal distance between the laser sync out signal and the release of the infrared

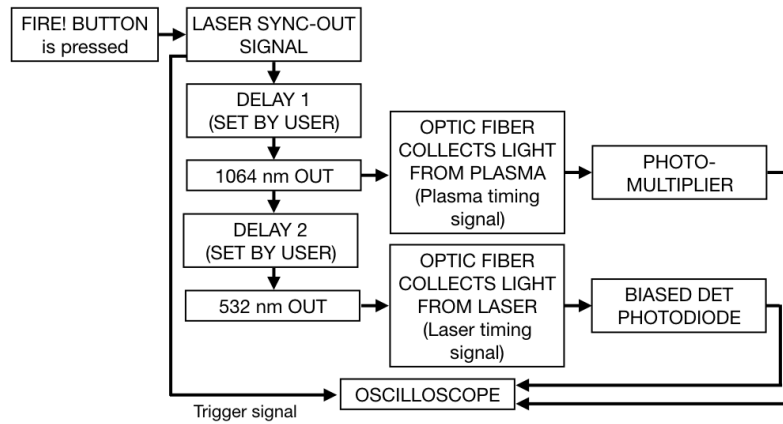


Figure 2.6: Diagram of the plasma-diagnostics synchronising system.

laser beam. It can be set to deliver the laser before the laser sync-out signal, however it is really irrelevant. Once the infrared beam is released, Delay 2 sets the time after which the diagnostics 532 nm pulsed is sent into the experiment. The internal synchronisation system of the EKSPLA laser sets discrete time steps for Delay 2 to $\Delta t \sim 125$ ns, which limits the interframe temporal distance of the data gathering.

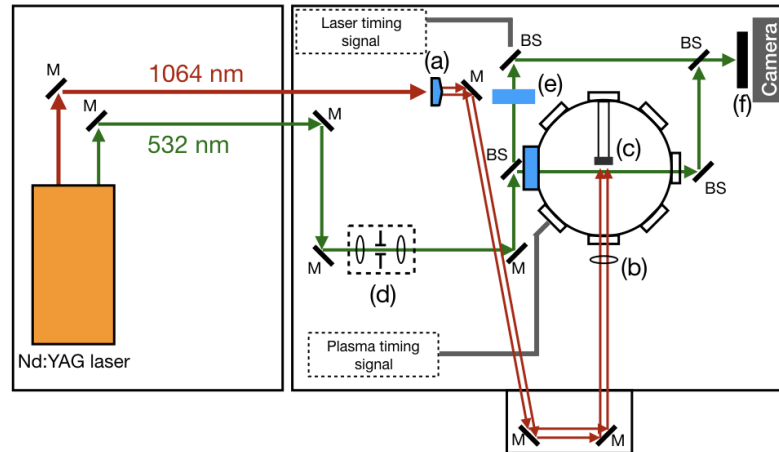


Figure 2.7: Schematic of the third experimental set up. Each rectangle denotes the edges of three different optic tables. (a) Axicon prism, (b) focusing lens and (c) is the flat carbon target, (d) is a spatial filter system to improve the quality of the diagnostics beam, (e) compensating glass and (f) neutral filter.

The third set-up keeps many aspects of the second. It inherits the synchronising system and the diagnostics optical up to the spatial filter. However, at this point we decided to take quantitative data. Hence, the schlieren imaging system was replaced and a modified Mach-Zehnder interferometer was mounted instead (Figure 2.7). The reference leg is additionally used to deliver the diagnostics timing signal. This set-up was used to obtain both shadowgraphy imaging (simply by

blocking the reference beam) and interferometry.

Notice that, in Figure 2.7 no mirrors can be found in the interferometer. This has purposes for the future: firstly, the installation of a side-on spectrometer which will capture self-emission from the plasma passing through the rightmost beamsplitter and, secondly, using the leftmost beam splitter as a window, take images using the ICCD. Thus, together with the corresponding triggering signals, a complete set of diagnostics will be mounted in the laser set-up: self-emission (imaging and spectrometry) and refractive (shadowgraphy and interferometry).

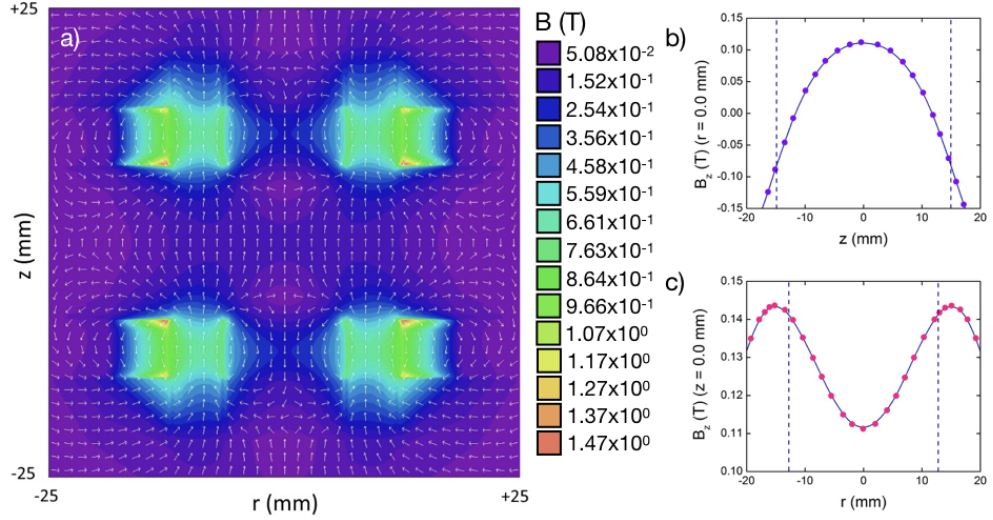


Figure 2.8: Magnetic field produced by NeFeB magnets. a) Topology of the magnetic field. Color code indicates the strength of the field, whereas the white arrows point in its direction. b) Numerical simulation (continuous line) and empirical data (purple dots) for the axial component of the field along the symmetric axis of the set-up. c) Numerical simulation (continuous line) and empirical data (pink dots) for the axial component of the field along the radial direction.

Finally, in order to investigate the effects of an external, static magnetic field, a set of two coaxial NeFeB ring-shaped permanent magnets was used. As explained in Chapter 1, the topology of the magnetic field is extremely important since the magnetic tension $\propto \nabla \mathbf{B}$. Figure 2.8a) shows both the magnetic topology and strength simulated by a finite-element simulation software developed by Field Precision LLC, *Magnum* [26]. The simulation had been benchmarked and validated in previous reports (e.g. see Mario Favre *et al.* 2017 [27]) using Hall probes in the radial and axial directions, as shown in Figure 2.8b) and c). The target is placed between the two bottom magnets in Figure 2.8, therefore, close to the target surface the magnetic field is mainly radial. However, as the plume expands, the magnetic field is mainly axially.

Chapter 3

Experimental Results

In this chapter I present the results from two different sets of experiments, differing in both the radius of the annular beam, target material, background gas pressure and diagnostics. Firstly, the results for titanium annular plasma plumes propagating through the low pressure (~ 100 mTorr) residual air in the vacuum chamber. Secondly, the results for carbon annular plumes in high pressure (order of 1 atm) argon gas background.

The reference time $t = 0$ is defined by the oscilloscope time when the plasma is detected using a combination of an optic fiber and a photo-multiplier, as discussed in Chapter 1. Both of these experiments were carried independently with and without an external static magnetic field provided by NdFeB permanent magnets. Henceforth, I use the term *free propagation* to denote the experiments *without* external magnetic field, despite the presence of the background gas.

3.1 Dynamics of Titanium Laser-Produced Annular Plasmas in Low Pressure Background Argon Gas

As a preliminary study of the dynamical evolution of the experiment, we started by investigating the plasma self-emission generated by focusing the laser beam onto a flat titanium (Ti). The experiments are carried in 80 mTorr ambient argon (Ar). The Nd:YAG 1064 ns, 3.5 ns FWHM laser operates at 10 Hz and diameter of the annular beam is 10 mm. The plasma is probed using the ICCD Andor camera gated with a 50 ns, 5 V square pulse, thus setting such as the time resolution of the imaging. The image timing is defined as the rise of the voltage pulse. For improving the visualisation, the gray-scale images obtained from the ICCD camera are presented in false color determined by intensity [18, 27].

Figure 3.1a) shows the imaging of the plasma propagating freely at early stages ($t < 600$ ns). At $t = 34$ ns we observe a flat uniform emission very closely to the target, where the axial propagation of the plasma dominates its early dynamics. A bright column in the centre of the plasma can be observed at $t = 74$ ns onwards, suggesting on-axis stagnation of the plasma at early times. The

apparent increase of radiance can be interpreted as *bremstrahlung* radiation produced by the free charged particles within the plasma rapidly stopping in the stagnation column. However this can only occur during the initial stages of evolution of the annular plasma, therefore one concludes that the enhanced irradiance from the central column for later times is related to the increase of temperature of the plasma produced by the inelastic collision of the flows propagating on-axis.

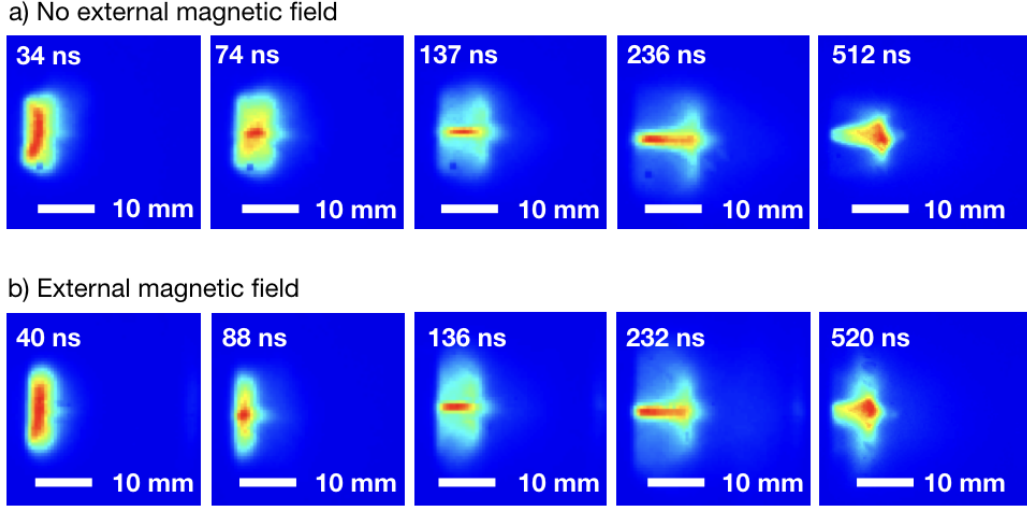


Figure 3.1: Set of images representative of the characteristic time evolution of the Ti plasma plume, as measured by its self-emission before $t = 600$ ns. a) Plasma propagating freely and, b) plasma in an static external field.

The formation of a plane front propagating together with the leading tip of the jet-like structure can be observed at $t = 137$ ns. The fact that the plume has a highly defined edge can be ascribed to the propagating plasma sweeping the background gas at supersonic velocity, thus producing a shock. This is evident at 236 ns, as the planar front is defined a thin, radiative structure, as opposed to the decaying light emitted by the receding plasma found between the radiant shock wave and the Ti target and outside of the central column. Afterwards, the column is observed to decay, the planar front evolves into a curved plume at ~ 500 ns with a sharp tip defining the leading feature of the axial propagation. Notice that at this stage the central part of the leading plume is much brighter than the rest of it. This is inherited by the blast from the now extinct central column and shows that the temperature gradient can endure up until this stage.

Further imaging of the plasma self-emission at later times ($t > 600$ ns) is shown in Figure 3.2. It reveals that the initially planar blast wave evolves into a round bullet-like plume at $t = 1230$ ns. Meanwhile, the jet-like structure can no longer be observed, which can be expected as a consequence of the plasma thermally expanding as the pressure of the surrounding medium decreases. Finally, at characteristic time scales $t \sim 4000$ ns, the plasma is observe to extinguish, suggesting that it has become a rather cold gas.

An outstanding feature of when comparing the free propagation experiment to the one with

magnets is that the presence of the external field does not seem to be morphologically relevant in the evolution of the plasma at early times. By comparing Figure 3.1a) and b), other than the fact that at 88 ns the plane front of the plume appears to be closer to the Ti target than at 77 ns of the freely propagating plume, the morphology and evolution of the annular plasma does not seem to change drastically.

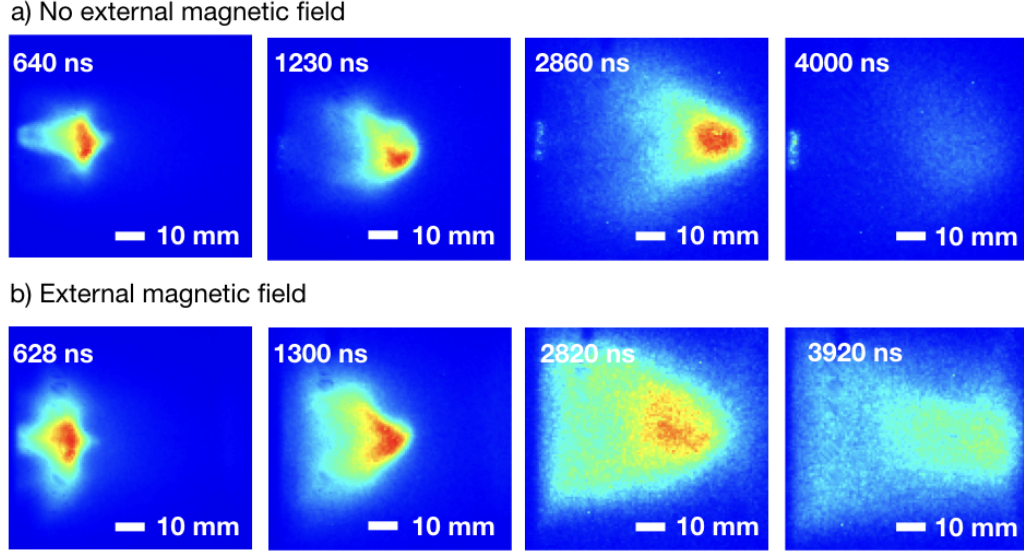


Figure 3.2: Set of images representative of the characteristic time evolution of the Ti plasma plume, as measured by its self-emission from $t \sim 600$ ns to ~ 4000 ns. a) Plasma propagating freely and, b) plasma in an static external field.

In contrast to early times, we observe significant differences between the free and magnetic field propagation as shown in Figure 3.2a) and b). Firstly, it is quite evident that the tip of the plume seems sharper with the presence of the external field at both ~ 600 ns and 1250 ns. This might be explained as a confinement effect due to the presence of a mostly axially oriented field in the symmetry axis of the magnets. This field would impose a magnetic tension hampering the radial propagation of the leading edge, effectively acting as a guiding field.

At $t \sim 4000$ ns, we observe that the plasma is much more radiant when embedded in the external magnetic field and confined within the region between the magnets. This can be interpreted in the following way: firstly, due to gyro-orbits introduced by the magnetic field, the ratio of the particle travel-path to the mean-free-path is larger than in the case of free propagation. Hence, the collision rate for electrons and ions increases, consequently radiating by two main mechanism: free-free radiation generated mainly by electron-electron and electron-ion collisions and excitation of the bound electrons within the ions and neutral atoms, which later decay into lower energy levels radiating photons. To confirm this hypothesis, it is necessary to obtain spectra and/or spectral imaging of the plasma at these times, which is beyond the scope of this thesis and proposed as future work in Chapter 4. However, let us support the statement by estimate the gyro-radius for

Ti and Ar with average ionisation $Z \sim 1$ and temperature $T \lesssim 1$ eV (which is consistent with a cold plasma, which is reasonable at very late times of the experiment). The mean magnetic field strength in the region between magnets is $\sim 5 \times 10^2$ G, therefore the gyro-radii $R_{g,Ti} \lesssim 1.3$ cm and $R_{g,Ar} \sim 1$ cm, which is consistent with the observations.

In order to quantify the effects of the magnetic field in the flow dynamics, we plot the intensity profiles of each image and measure the position of the plasma at different times. Figure 3.3a) and b) depicts this process: the intensity profile is plotted at the axis of symmetry. Two different regions can be defined as the boundary of the plasma, both of which are in fact interesting. Firstly the leading edge of the plasma, which can be found in the upstream and, secondly, the shock. Since they are, in principle, independent objects, both trajectories are tracked.

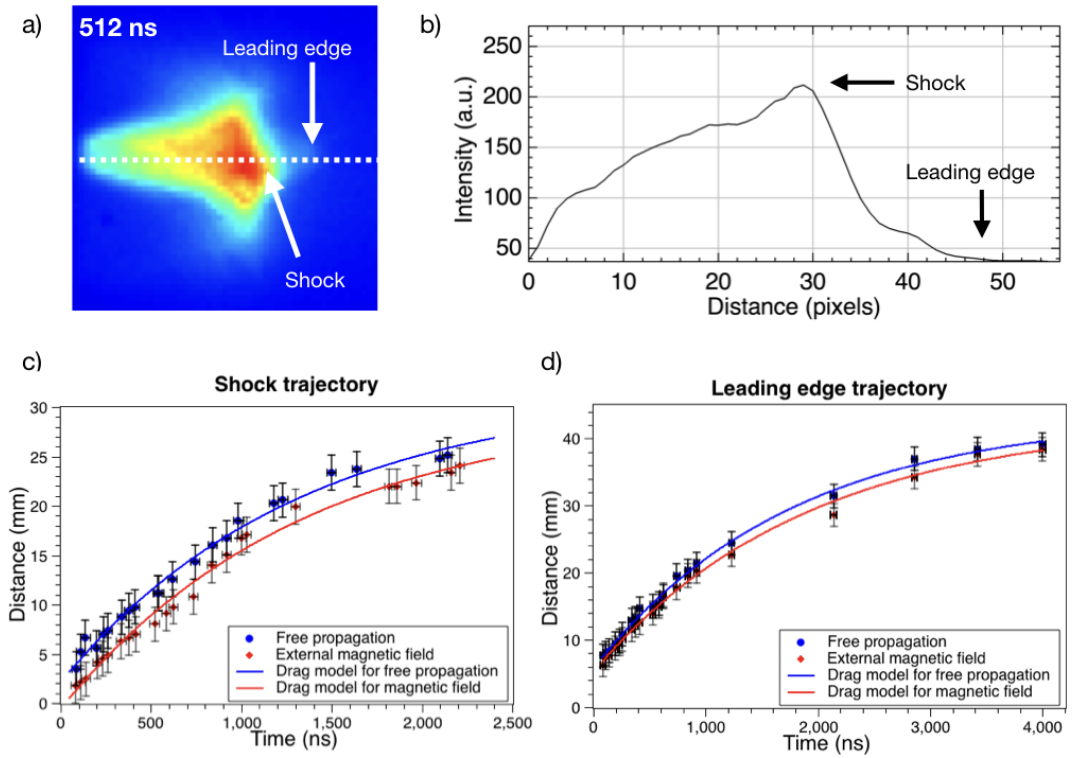


Figure 3.3: a) False color image of the Ti plasma plume at $t = 512$ ns. Two separate regions are identified and pointed with white arrows: the shock and the leading edge. The dotted line shows the approximate portion inspected using ImageJ to plot the intensity profile. b) Intensity histogram extracted from image. c) Trajectories of the shock in both free propagation and in the magnetic field and, d) trajectories of the leading edge in both free propagation and in the magnetic field.

Figure 3.3b) notably resembles the ‘cartoon’ description of a compressing wave, with the main increase in luminosity attributed to the shock region, *i.e.* a denser region of hotter fluid elements is expected to have enhanced radiance. Furthermore, the region contained between the shock and

the leading edge can be interpreted as a precursor, produced by pre-heating processes of the shock over the upstream.

The data sets are fitted extremely well with the drag model. In the case of the shock trajectory $R^2 = 0.9897$ and $R^2 = 0.9893$ in free propagation and with external field, respectively. To denote quantities calculated for the experiments with the external field I will add a sub-index B , which will be omitted in free propagation. Using the fitting parameters of the model, one can easily compute that the initial axial velocities are $v_0 = (2.2 \pm 0.6) \times 10^6$ cm/s and $v_{0B} = (2.3 \pm 0.6) \times 10^6$ cm/s. Therefore, the effect of the magnetic field is not important at initial stages, which is consistent with a plasma heavily dominated by thermal pressure rather than MHD confinement effects, *i.e.* magnetic pressure and tension.

Similarly, the propagation of the leading edge can be adjusted with the drag model, since $R^2 = 0.9967$ in free propagation and $R^2 = 0.9954$ with external field. The initial velocities are not distinguishable from the initial velocities of the shock $v_0 = (2.1 \pm 0.4) \times 10^6$ cm/s and $v_{0B} = (2.0 \pm 0.4) \times 10^6$ cm/s.

This trend is consistent after comparing the drag coefficients (at this point the reader should remind that the magnetic pressure acts analog as an external fluid onto the plasma). From the fitting, for the shock $\beta = (7.6 \pm 2) \times 10^5$ s⁻¹ and $\beta_B = (7.5 \pm 1) \times 10^5$ s⁻¹, thus the difference in the drag coefficient is not significantly changed due to the magnetic field. Similarly, for the leading edge we find $\beta = (5.7 \pm 0.9) \times 10^5$ s⁻¹ and $\beta_B = (5.3 \pm 0.9) \times 10^5$ s⁻¹.

A statistically significant effect in the axial propagation of the shock between the two experiments can be found in the difference of the initial position $\Delta r_0 = r_{0B} - r_0 = (8.1 \pm 0.1) \times 10^{-3}$ m. This can only be explained in terms of magnetic effects during the implosion process, from which the central column and the axial shock is formed afterwards. From the magnetic topology, notice that the target is located where the magnetic field is mainly radial, thus it acts as a guiding field. Therefore it must be the magnetic pressure responsible for the changes during the initial stages. Our interpretation is that during the very first stages of the initial implosion, the streams of plasma moving inwards are retained by the magnetic pressure, delaying its arrival into the stagnation column. Hence, the axial propagation stages is consequently delayed.

In contrast, there is no significant difference between the initial position of the leading edge in the two experiments, since $\Delta r_0 = r_{0B} - r_0 = (0.5 \pm 1) \times 10^{-3}$ m. This is consistent with the interpretations proposed above. Since the leading edge seems to determine a boundary of the shock wave precursor, it is natural to think that its initial stages once the axial shock is already formed.

Analog to the axial expansion, we measured the radial expansion using with a profile line at a constant distance of 2 mm from the surface of the target. The result is shown in Figure 3.4, and shows that the ballistic model is very accurate with $R^2 = 0.9853$ and $R^2 = 0.977401$ in free propagation and with external field. Notice that the global structure of the outwards radial from does not form a sharp edge, as opposed to the axial propagation. This suggests that the pressure

exerted by the background Ar is not sufficient to drag the propagating plume nor form a shocked region. No statistically significant differences between the free propagation and magnetic field are found. The outwards expansion velocity are $v_0 = (2.4 \pm 0.3) \times 10^6$ cm/s and $v_{0B} = (2.5 \pm 0.4) \times 10^6$ cm/s.

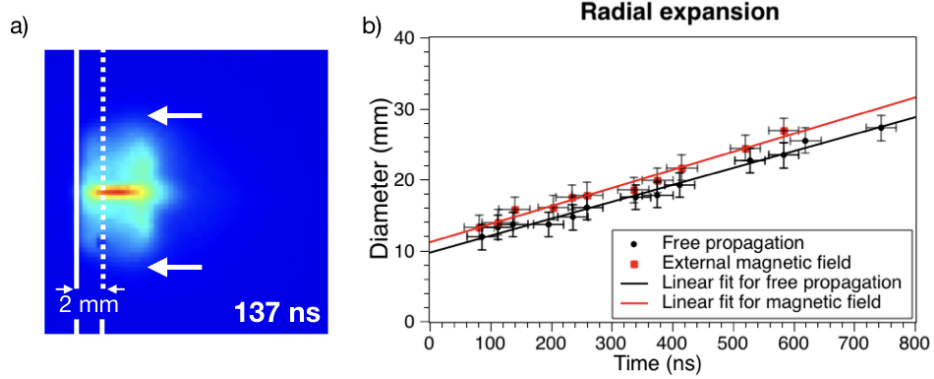


Figure 3.4: a) False color image of the Ti plasma plume at $t = 137$ ns. The continuous white line shows the approximate position of the solid target, whereas the dotted line shows the approximate portion inspected using ImageJ to plot the intensity profile. b) Trajectories of the diameter of the plume in both free propagation and in the magnetic field.

Finally, the collisionality parameter defined by equation (1.18), $\xi = D/\lambda_{ii}$, can be used to estimate parameters of the plasma. By taking the typical separation of the counterstreaming plasmas as the radius of the ring¹ $D = 5$ mm, $n_e \sim 10^{18}$ cm⁻³ and approximating the characteristic inwards velocity to be equal to the outwards velocity $\sim 1 \cdot 10^6$ cm/s and using the fact that $\xi \geq 1$, then the average ionisation is constrained to be $Z \geq 2$. Conversely, by assuming $Z \geq 1$, the electron number density has a lower constraint $\sim 10^{11}$ cm⁻³.

3.2 Dynamics of Carbon Laser-Produced Annular Plasmas in High Pressure Background Argon Gas

In order to inspect in detail the dynamics of the shock waves produced in the experiment, we introduced a new set of refractive diagnostics: schlieren, shadowgraphy and interferometry. Taking advantage of the fact that magnification can be easily modified with optical systems, we switched to smaller annular beams to increase the power density. Accordingly, the annular beam diameter is 2 mm. Furthermore, since carbon (C) is a very well studied material due to its multiple uses in pulsed-laser deposition, we decided to use C targets to have a better benchmark for quantitative data, *i.e.* interferometry. We studied the propagation of the plasma in uniform background argon

¹The reader must not feel confused by unfortunate notation. As defined in Chapter 1, D stands for the separation between the two plasmas, not the *diameter*. However, in terms of order-of-magnitude computation, it is not a really important distinction.

(Ar) gas at three different pressures: 140 Torr (~ 0.2 atm), 250 Torr (~ 0.3 atm) and 715 Torr (~ 1 atm). Henceforth, I will refer to the background pressure in atm rather than Torr. As discussed in Chapter 2, the experiment works on a shot-to-shot basis, *i.e.* one shot whenever the experimenter presses fire and one laser image per shot. The probing beam is produced by a Nd:YAG 532 nm, 3.5 ns FWHM laser.

3.2.1 Shadowgraphy & schlieren imaging

Reproducibility in experimental set-up 2 & 3

One of the advantages of taking images from on a shot-to-shot basis is the fact that erosion on the target's surface is significantly decreased. As consequence, the experiment has a higher degree of reproducibility, as clearly seen in the series of shadowgraph images presented in Figure 3.5. Those images were taken one after the other and once ~ 50 laser pulses had already ablated the target. No major differences can be noticed between images, in particular the shape of the outermost shell (which we will see below, is in fact a shock of neutral species).

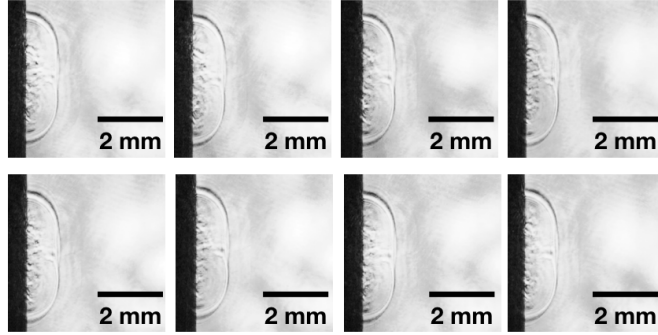


Figure 3.5: Series of different shadowgraph images of the blast wave at $t = 265$ ns.

However, notice that there are smaller structures contained within this shell that are irreproducible from shot-to-shot. This can be the result of two reasons: firstly, the alignment of the laser beams (both probing and plasma-producing beams) slightly changes in different shots, which can be observed as the change of luminosity of the beam for different frames, therefore the contrast changes in the ICCD between different shots and/or; secondly, those are in fact structures forming from non-linear phenomena, *e.g.* turbulence and rarefactions, and therefore are extremely sensitive of the initial conditions, *i.e.* both the state of the flat target and the conditions of the annular beam.

Time evolution of blast waves

In order to gain qualitative insights about the time evolution of the plasma plume within of the experiment I start this part by discussing shadowgraphy and schlieren images. Figure 3.6 show the first stages of the evolution, as the plume acts as a piston pushing the background gas. Notice

that, as one might expect, only at sufficiently low pressure (~ 0.2 atm) the plume is observed separated from the target at very early times $t = 9$ ns. At $t \sim 140$ ns the plasma expands forming a plane axial shock and round radial shocks. Notice that at background pressures lower than 1 atm the central column can be observed. This can be explained as the action of the background gas slowing down the inner-propagating streams of the annular plasma. A remarkable fact is that at $t = 264$ ns the shadowgraphy at 1 atm clearly shows the annular shape reported by Veloso (2006) [15] as the central column is formed by on-axis collapse of the ring-shaped plasma.

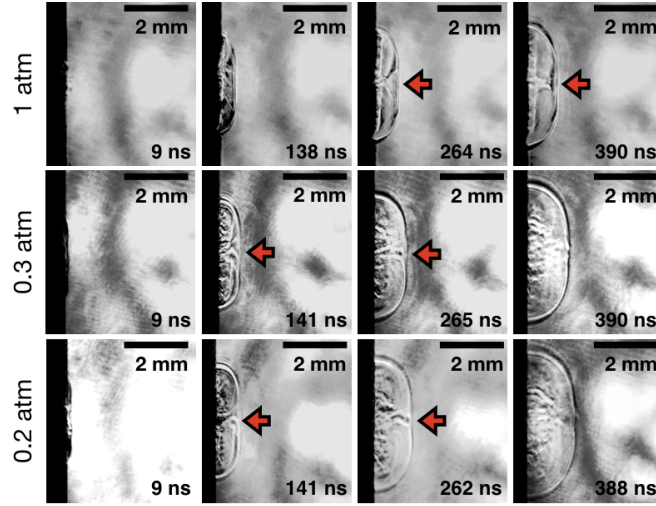


Figure 3.6: Shadowgraphy images of the experiment up to $t \sim 390$ ns. Time runs from left to right. The first row are all in 715 Torr background. Likewise, the second and third rows correspond to 250 Torr and 140 Torr, respectively. The red arrows point to the position of the central column.

This collapsed configuration is not obvious for later times. In order to discriminate the absence of the central column due to diagnostics limitations or internal motion of the plasma, I will discuss the schlieren imaging of the plasma. Indeed, the stagnation column within the annular plasma at 1 atm can be observed with greater contrast by using schlieren imaging as shown in Figure 3.7.

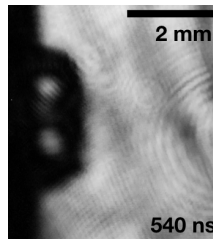


Figure 3.7: Schlieren imaging of the annular plasma in 1 atm background Ar.

Notice two things: firstly, the column can be observed for longer timescales than using shadowgraphy. For instance, compare Figure 3.7 in which the central column is evident at 540 ns to the first frame (1 atm, 514 ns) in Figure 3.8 in which the column can no longer be observed. This

is likely because schlieren is sensitive to first-order derivatives of the refraction index, in contrast to shadowgraphy which is sensitive for second-order derivatives. Therefore, schlieren is a better diagnostic to highlight borders. This indicates that within the region between the target and the outermost shock has a pressure strong enough to sustain the stagnation column confined. Secondly, notice that the quality of the imaging is not as detailed as the shadowgraphy. This is due to departure from the paraxial propagation of the probing beam along the optical path, as can be observed from dark regions within the laser spot. Thus, I will not further study the schlieren imaging.

I will now discuss the outermost shock dynamics. Within characteristic timescales $t \sim 500$ ns the axial front of the blast wave seemingly keeps a planar configuration. However, this dramatically changes during the following dynamical stages. Two main features can be observed from characteristic timescales $t \sim 500 - 1500$ ns (Figure 3.8): firstly, the axial front becomes round which is consistent with the observation of the low background pressure in Ti plasmas and; secondly, the central part of the blast wave propagates faster than the rest. This is consistent with the formation of a hot jet-like structure observed using schlieren pushing the central part of the blast wave, propelling it forward. Henceforth I will refer to this special feature as a ‘bubble’, for rather evident reasons.

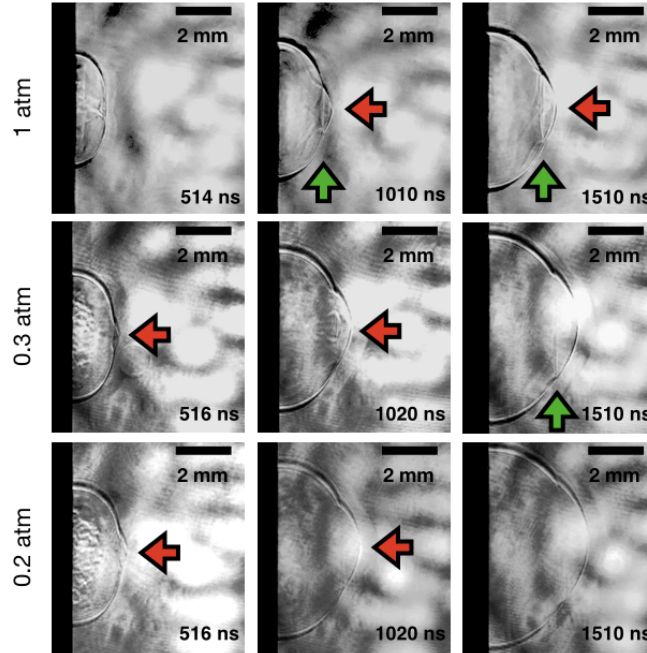


Figure 3.8: Shadowgraphy images of the experiment from $t \sim 500$ ns to $t = 1510$ ns. Time runs from left to right. The first row are all in 715 Torr background. Likewise, the second and third rows correspond to 250 Torr and 140 Torr, respectively. The red arrows point to the position of the emerging bubble, whereas the green arrows point to the planar front.

The red arrows in Figure 3.8 point at the position of the seemingly emerging bubble produced

in the central part of the blast wave. Additionally, a second planar front can be observed as a thin black line within the downstream of the bubble. This feature is highlighted by the green arrows in Figures 3.8 and 3.9. Notice that it always delimits the bubble from the rest of the radially propagating blast wave. This suggest that it is not a true shock, but rather that there is a layer that separates the radial blast wave and the bubble.

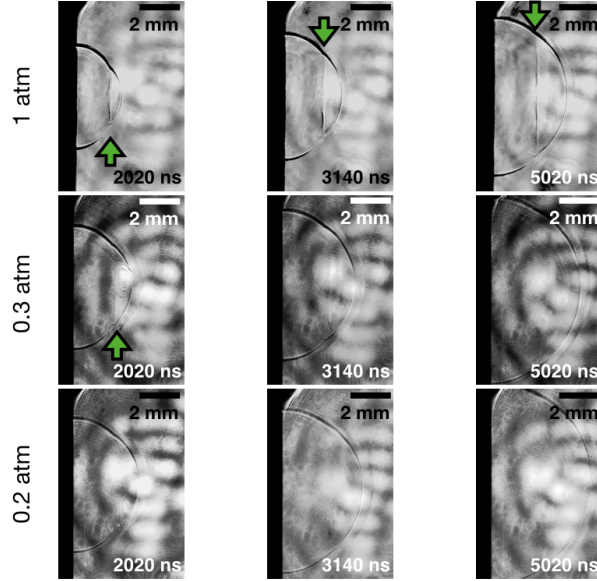


Figure 3.9: Shadowgraphy images of the experiment from $t = 2020$ ns to $t = 5010$ ns. Time runs from left to right. The first row are all in 715 Torr, the second row corresponds to 250 Torr and third row corresponds 140 Torr, background gas pressure. The green arrows point to the planar front.

Up to this point it is confident to say that the laser-produced annular plasma is in fact a solid method to produce asymmetric shocks. Notice that the sharp tip in the central part of the blast wave is a robust characteristic of the long-time dynamics of this experiment, even when performed under high-pressure environments. This is extremely relevant, because temperature gradients disrupt the symmetry of shocks, *i.e.* planar and spherical blast waves cannot have temperature gradients along their shocks [28].

Probing of later times indicates that there is a transition from the *asymmetric* blast wave into an apparently spherical blast wave, as can be seen in Figure 3.9. In fact, excepting 1 atm experiments which have the slower pace for time evolution, the thin line delimiting the separation between the bubble and the rest of the blast wave cannot be observed. Thus, one can conclude that a rather spherically symmetric configuration has been reached. This is consistent with the effect of drag produced by the background gas: since the force exerted by the surrounding gas is proportional to the velocity of the shock, then it brakes the faster part of the blast wave, *i.e.* the anomalous bubble, more efficiently than the rest of the blast wave, allowing it to ‘catch up’, this resulting in a symmetrical configuration.

Effects of the magnetic field in the asymmetric blast waves

Now I focus on the effect of the external magnetic field in the dynamics of the blast waves. As we will see in the next section, the outermost shock is not ionised, therefore any change in the dynamics is due to the effect of the magnetic field in the initial annular plasma, *i.e.* altering the dynamics of the initial piston. Due to experimental constraints, the target is now placed in a region where the magnetic field is axial, *i.e.* near the central region between magnets.

Figure 3.10 shows the shadowgraphy images of the plasma at $t = 140$ ns in free propagation (top row) and with the external magnetic field (bottom row). It is extremely interesting the seemingly unstructured shape of the plasma within the magnetic field at 1 atm. Also notice that, within the outermost shock in the experiments at 0.3 and 0.2 atm background gas, these structures emerge. Therefore, one concludes that the initial stages of the annular plasma are drastically affected by the external magnetic field.

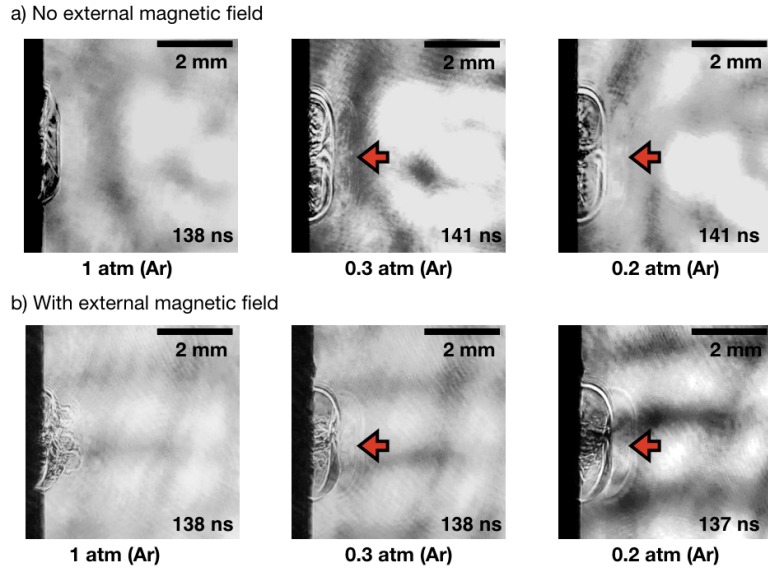


Figure 3.10: Shadowgraphy images of the experiment at $t \sim 140$ ns. The first row shows results in free propagation, whereas the second with the external magnetic field. The red arrows point to the central column.

Based upon the discussion in Chapter 2, this could be an effect on two separate length-scales: microscopic scales, determined by the gyro-orbits and macroscopic fluid-scales. The typical gyro-radius for C ions with average ionisation of $Z = 1$ is $R_{g,C} \sim 0.6$ cm and for Ar $R_{g,Ar} \sim 1$ cm, which are larger than the outermost shock observed at these times, whereas for electron is $R_{ge} \sim 1 \mu\text{m}$, which is much smaller than the structures observed. Thus, it is concluded that the structures must raise from a fluid-like nature of the laser-produced plasma.

Furthermore, possibly as heritage from the early-formed structures, we observe a complex central columns formed during the inwards collapse of the ring. By comparing the experiment at 0.2 and 0.3 atm background gas at $t \sim 140$ ns, the accompanying shocks propagating radially

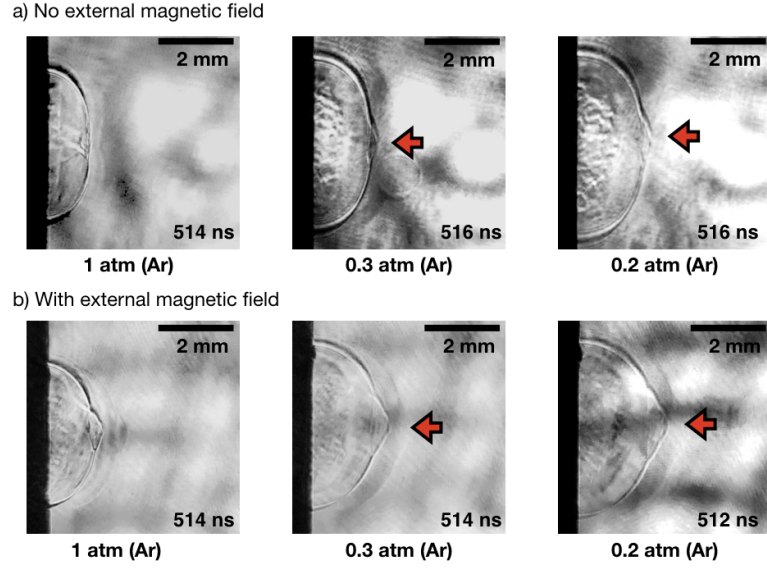


Figure 3.11: Shadowgraphy images of the experiment at $t \sim 500$ ns. The first row shows results in free propagation, whereas the second with the external magnetic field. The red arrows point to the central column.

outwards from the annular plasma when in presence of the magnetic field also appear to be less structured to those in free propagation. An outstanding result is that, similarly to what it is observed in the Ti plasma at $t = 1300$ ns, the tip of the blast wave is extremely sharp, as seen in the anomalous bubble expanding in the axial central front. This feature of the blast wave is very relevant, as the asymmetry seems to be enhanced by the external field probably due to collimation of the jet-like structure within the blast wave.

However at later times $t \sim 2000$ ns the shock transits into a more symmetrical configuration, as can be observed in Figure 3.12. The planar front previously interpreted as the interface between the axial bubble and the radial part of the shock seems less apparent when the plasma propagates in the external magnetic field. It is possible that the magnetic pressure/tension not only collimates the central column, but it also smooths the differences in propagation velocity right in the interface resulting in a less sharp configuration.

Now, in an analogue to the Ti plasma experiments, we quantify the effects of the background pressure and external magnetic field on the propagation of the blast wave. Only the axial propagation of the central part of the blast wave, *i.e.* the bubble, is studied.

All the trajectories are very well fitted using the drag model, as every curve has $R^2 > 0.99$ when compared with the data (the summary can be found in Appendix A). For the sake of clarity I will first compare the difference in free propagation under different background gas pressure. Notice that all the relative errors are *larger* when compared with the Ti plasma experiments, even though the precision is higher in this case, *i.e.* the temporal resolution of the diagnostics is higher together

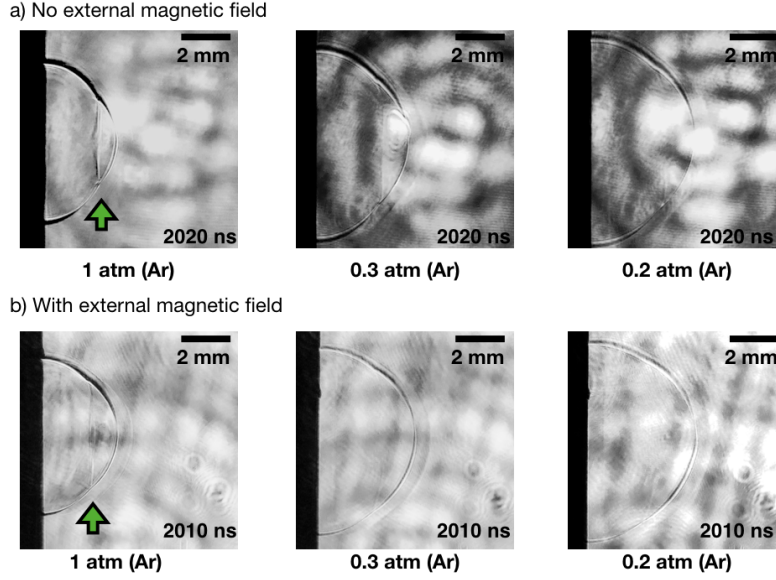


Figure 3.12: Shadowgraphy images of the experiment at $t \sim 2000$ ns. The first row shows results in free propagation, whereas the second with the external magnetic field. The green arrows point to the planar front.

with higher confinement of the shock waves due to the background pressure. This is because the annular beam is *smaller* by a factor of 5, therefore, every initial condition is smaller. In addition, due to the high-pressure Ar, the experiment evolves slower and at shorter final spatial-scales (as I will show below), therefore even though the absolute errors are smaller, the magnitude of the data gathered is smaller by a larger factor.

Now to the results. Firstly, the stopping distance r_s statistically increases as the pressure decreases, as $r_s(1 \text{ atm}) = (5.0 \pm 1.4) \times 10^{-1}$ cm, whereas $r_s(0.3 \text{ atm}) = (6.1 \pm 1.6) \times 10^{-1}$ cm and $r_s(0.2 \text{ atm}) = (6.6 \pm 1.5) \times 10^{-1}$ cm which is precisely what one would expect as the dissipation of momentum due to the interaction with the surrounding medium is reduced.

In contrast, the initial velocities are very similar from one to another. All the initial velocities are $v_0 \sim 2 \times 10^5$ cm/s (for further details, see Appendix A). This is one order-of-magnitude lower than the Ti annular plasmas. Notice that the power density in the C plasmas is larger by a factor ~ 5 than in the Ti plasma set up and the mass of the carbon atoms are ~ 3 times lighter than the titanium.

The interpretation of this result is that the surrounding gas in fact exerts pressure in the initial stages of the ablation of the target, thus the time for ballistic propagation is absolutely negligible. This is consistent with a gas made up of lighter atoms colliding against a mass of high-pressure gas. Thus, the mass of the blast wave equals the mass of the upstream almost immediately. Once said that, it is reasonable to assume that at least in a factor of 5, *i.e.* within the range of background pressure when comparing 1 atm to 0.2 atm experiments, the effect of the background gas to the initial velocity of the plasma is negligible.

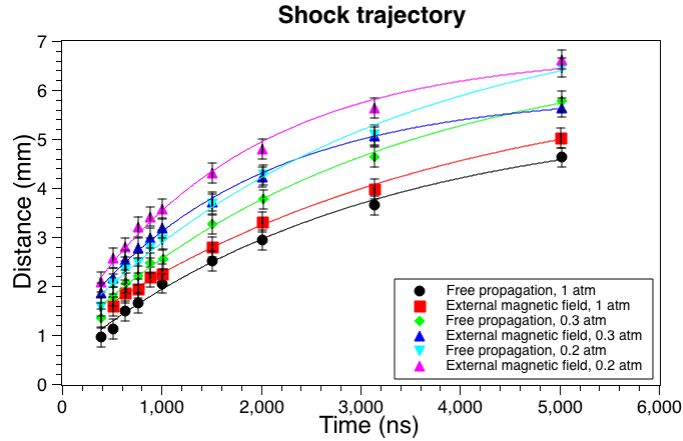


Figure 3.13: Trajectory profiles for the on-axis propagation of the blast wave.

Consistent with the discussion in Ti plasmas, the effect of the magnetic field in term of the parameters within the drag model can be neglected. There is no statistically significant differences between the free propagation and external magnetic field experiments. Although at all cases seems to have a collimating effect on the plume or bubble, for Ti and C plasmas respectively, the effect is not important in terms of propagation rates. In the case of the high-pressure backgrounds, this will be consistent with the fact that the outermost shock is in fact composed mainly by neutral gas, as I discuss in the next section.

3.2.2 Interferometry

We have now established a general description of the macroscopic dynamics in the high pressure experiments. However, one would like to know in a quantitative way some of the physical properties of the blast wave. Thus, one would like to distinguish the parts of the blast wave are *neutral* gas from the *ionised* plasma. Furthermore, it is necessary to quantify the electron density within the plasma.

I will now centre on the preliminary analysis in 3 characteristic instants in the time evolution of the experiment at 0.3 atm. These particular images were selected based on the overall quality of the fringe pattern, as the diagnostics beam sometimes have dark regions and the plasma sometimes imprint shadowgraphs onto the detection plane, effectively cutting the fringes.

The reference interferograms were taken after filling the vacuum (or lack thereof) chamber to the operational background pressure. Additionally, the orientation of the fringes are perpendicular to the target to obtain measurements of the axial propagation of the plasma. Measurements using fringes parallel to the graphite target were also performed, but not analysed in this work.

In order to primarily distinguish fringe shifts given by electron density from neutrals, interferograms taken on a candle were taken. Thus, nearby the candle wick the shifting is attributed to the effects of the electrons and notated in which direction. Therefore, fringe shifting in the opposite

direction is interpreted as neutrals. This will be confirmed during the analysis.

The electron density is obtained using an interferometry evaluation program called IDEA [25]. This program allow us to calculate the phase difference between the reference and ‘plasma’ interferograms, by tracing the fringes. In order to ensure a proper tracing, Figure 3.14 depicts the first steps in the analysis: produce an idealised skeleton of the fringe pattern. Using the path tool built-in the GNU Image Manipulation Program (GIMP) we draw one-pixel width lines representing the fringes in the interferogram for all ‘plasma’ and reference images.

These skeletons are then analysed using IDEA. The user provides certain masks to focus the analysis on the region of interest. Then the software employs fast Fourier transforms to track the lines and assign a phase to each pixel, given by the position with respect to the fringe. Then it subtracts the ‘plasma’ interferogram from the reference, obtaining a map of the phase difference.

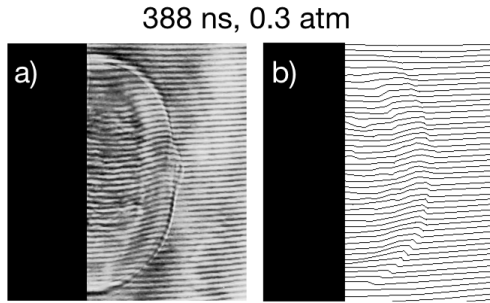


Figure 3.14: Interferogram of the plasma plume at 388 ns in 0.3 atm Ar background. a) Experimental data and, b) one-pixel width path of the fringes.

In order to obtain densities one must take certain considerations. Firstly, to avoid taking assumptions on the cylindrical symmetry of the system, no Abel inversion is performed, thus one does not obtain the density n , rather the integral of the density along the optical path of the probing beam $\int n dl$. Secondly, notice that from the discussion in Chapter 2, the fringe shift along produced by an electron gas carries a negative sign (see equation (2.5)). This distinguishes the electron fluid from the neutrals. Therefore, it is straightforward to tell when certain regions in the system are dominated by electrons or neutrals. Two separate calculations on the fringe shift are needed, one for each dominant component. When analysing the electron gas, *i.e.* the plasma, one follows the method explained in Chapter II. However, to analyse the neutral gas one must use Cauchy equation [29]

$$n_g = \left[A + \frac{B}{\lambda^2} \right] \frac{N_a}{N_L}, \quad (3.1)$$

where n_g is the gas refractivity, A and B are tabulated coefficients, λ is the probing laser wavelength, N_a is the gas number density and $N_L = 2.7 \times 10^{31} \text{ cm}^{-3}$ is the Loschmidt number. Therefore, notice that in both cases finding the phase shift along the optical path is reduced to multiply by the proper constants in the correspondent case, since as in the case of a plasma, the

fringe shift due to neutrals is also proportional to the line integral of the neutral number density along the path of the probing beam.

The resulting preliminary maps are presented in Figure 3.15. Preliminary, the analysis converting the phase shift into electron density map was used, in order to focus the analysis on the plasma. Thus, the absolute value of the color number labeling the neutrals is incorrect and correcting this is left as future work, following the discussion above. Notice that they show horizontal lines, the same direction of the fringe shifting. They appear as the result of the misalignment of the reference and ‘plasma’ interferograms. It is raised as a consequence of the spatial differences in luminosity of the laser beam passing through the interferometer on a shot-to-shot basis. Due to the fact that the analysed fringes are traced by hand and are one-pixel width, they are extremely hard to perfectly match. However, the dominant color on each region does in fact indicate features of the blast wave. As discussed above, the sign in the color bar indicates the composition from which is raised a given the refractive index. Therefore, positive signs indicates the presence of neutral gas, whereas the negative fringe shifting indicates the presence of the electron gas produced by ionisation, *i.e.* plasma.

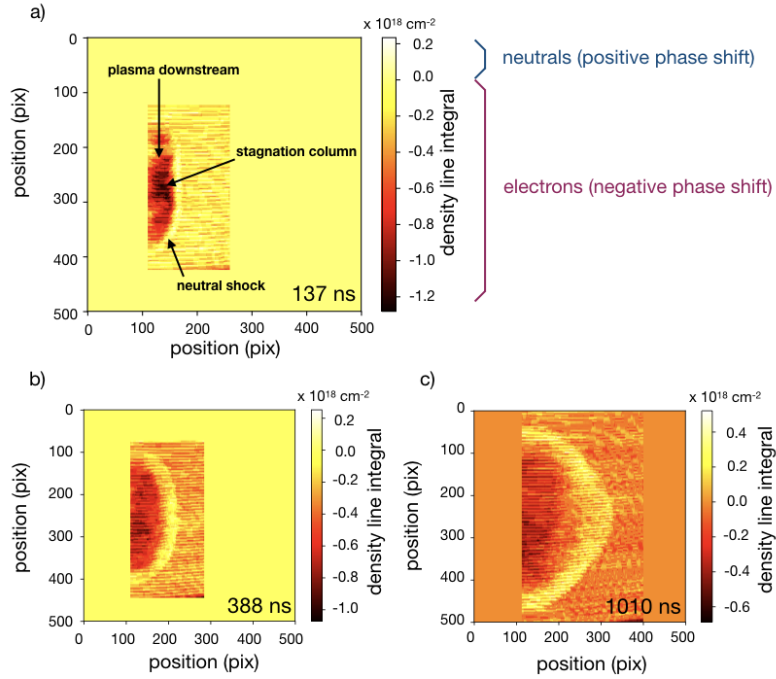


Figure 3.15: Preliminary density maps (along the optical path) in 0.3 atm Ar background. a) Blast wave at $t = 137 \text{ ns}$. The stagnation column, plasma downstream and neutral shocks are indicated by inlet arrows. Additionally the interpretation of the sign on the line density is provided. b) Blast wave at $t = 388 \text{ ns}$ and, c) blast wave at $t = 1010 \text{ ns}$.

At 137 ns we observe a central very dense region of plasma resulting from the stagnation process within a shock of neutrals. One can estimate the inwards velocity as the ratio between the radius

of the annular beam and the time it is observed to take the plasma to form the stagnation column, $v_{in} \sim r/T \sim 10^6$ cm/s. This is consistent with the speed of sound for Ar gas in standard conditions being $\sim 10^5$ cm/s. The stagnation column is roughly 50% more dense than the surrounding plasma. By assuming that the fringe shift through the optical path of the probing beam is dominated by this column, one can estimate that the electron density is $\sim 10^{19}$ cm⁻³, thus the collisionality parameter $\xi \sim 10^3$ for a C plasma with average ionisation $Z = 1$.

The lifespan of the column is rather short at this background pressure, however, since at 388 ns the column can no longer be observed. On the contrary, a feature sustained in time is that the surrounding plasma is retained within a neutral shocked region, which defines the outermost part of the blast wave. Thus, at all times it is observed that the innermost part of the blast wave, namely the downstream, is always filled with plasma.

These observations are consistent with an initial detonation forming a plasma that, subsequently acts as a piston pushing the surrounding gas. However, given the asymmetry of the initial detonation. *i.e.* the annular form rather than a point-like spot, leads to the formation of an asymmetric blast wave. At $t = 1010$ ns, the shock is clearly not spherically symmetric. Additionally, notice that the observed bubble leading the axial propagation is constituted mainly by neutrals, indicating that it is formed by the enhanced pressure of the central part of the piston.

From the fact that these asymmetric blast waves are mainly composed by neutrals one can comment on several things: firstly, that the action of the supersonic piston is not sufficient to produce a strong ionisation of the surrounding medium. Secondly, that it is not strange that the effects of the external magnetic field are negligible, as the plasma is confined within the downstream and does not significantly contribute to the composition of the shocked region. Thirdly, this certainly constitutes a drawback to study the Biermann battery in high-pressure background gases, as a requirement is that the fluid is a conductor.

Happily, there are possibilities in the future. Notice that there is a sharply defined difference between the neutral shock and plasma downstream. This, in addition to, the stagnation columns observed in high-pressure background gas, the observation of asymmetry in the blast waves and difference in radiance in low-pressure backgrounds suggests that the Biermann battery might be present within this experiment, as they are indicative of non-parallel temperature and density gradients.

Chapter 4

Conclusions and Future Work

In this thesis we studied the dynamics laser-produced annular plasmas produced from Ti and C solid targets. By using a combination of an axicon prism and a converging lens, an Nd:YAG 3.5 ns FWHM, 1064 nm laser beam is focused onto the targets in a ring-like shape.

For both experiments we observed that the expansion of the initial annular plasma determines multiple fronts of supersonic interaction amongst fluids. This can lead to future studies and comparison between different regimes in hydrodynamical supersonic motion within one compact experimental set-up.

The formation of a stagnation column produced by the inwards radial propagation of the annular plasma was observed in both low- and high- pressure argon gas, *i.e.* 80 mTorr and ~ 1 atm respectively. As very well known in the literature, the stagnation process always produces an increase of temperature of the incoming streams, due to the randomisation of the macroscopic forward momentum, thermalising it during the inelastic collision. After the radial collision, the column propagates axially, producing an asymmetric shock wave when interacting with the surrounding medium.

In particular, for Ti plasma experiments with an initial ring radius $r = 5$ mm propagating in 80 mTorr argon background, at times ~ 80 ns the stagnation column was first observed using 50 ns time-resolution ICCD imaging. The outermost part of column resembles the tip of a jet-like structure, that then propagates axially, forming a planar shock when interacting with the ambient gas. This configuration represents a robust feature of the dynamics of the plume up to characteristic times ~ 500 ns. Afterwards, however, the column cannot be observed and the blast wave transits from a planar configuration into a bow-like shock.

The axial front of the blast wave propagates with a characteristic velocity $v \sim 10^{5-6}$ cm/s decreasing with time very described by a drag model. Observations of the plume under the effects of an external magnetic field indicate that velocity of the flow is not altered by the external field due to magnetic confinement effects. This indicate that the thermal pressure dominates the momentum equation of the plasma. The front propagating radially outwards ballistically at a characteristic velocity $v \sim 10^6$ cm/s is much less radiant than its axial counterpart. Hence, radiance differences

along the shocked region suggest that its central part is in fact at a higher temperature than the plume propagating radially outwards.

Likewise, for smaller ring radius $r = 1$ mm illuminating C plasma experiments embedded in high-pressure argon background gas we observe the central column using time-resolved schlieren imaging. Using interferometric imaging from the blast wave, is it observed to be composed by an outermost shocked region of compressed neutrals and a plasma downstream. Thus, the laser-produced annular plasma behaves like a supersonic piston, compressing the ambient argon, subsequently producing two different fronts on the propagation. The first one is an asymmetry on the outermost part of the shock wave, as an expanding bubble leading the axial propagation of the blast wave. The blast wave expands at characteristic velocity $v \sim 10^5$ cm/s, regardless of the gas background pressure. Similarly, the effect of the external magnetic field is negligible within error bars.

In summary, for both experiments we have build an experimental platform to study in detail the formation of asymmetric blast waves, which show different dynamical properties depending on the material and background gas pressure. Thus, the latest experimental set-up allowed us to switch between diagnostics easily. The experimental set-up currently under construction will have parallel ICCD imaging with improved time resolution and spatiotemporally resolved spectrometry. Additionally, by increasing the strength of the external magnetic field we aim at gaining even more control over the time evolution of the asymmetric blast waves.

This results are encouraging for future studies regarding the Biermann battery: a two-fluid magnetohydrodynamical effect that allows the formation of magnetic seeds from initially unmagnetised plasmas. This is a mechanism by which the magnetic fields present throughout the Universe might had formed, and consequentially amplified through non-linear phenomena such as turbulence. However, the Biermann battery can only operate when the density and temperature gradients in the electron fluid within the plasma are non-parallel and asymmetric blast waves are ideal environments to generate this effect. The nearest future work will focus on measuring temperature distribution within the carbon annular plasma using spectrometry. This will allow us to accurately quantify the strength of the Biermann battery in the linear regime since it is $\propto T^{1/2}$. Afterwards studies using ps pulsed lasers, target materials and different ring radii will allow us to study different regimes of the plasma, as energy deposition, transport rates, amongst others will be modified. Characterising the dynamics of the laser-produced annular plasma, will allow us to benchmark simulations using state-of-the-art codes such as FLASH [30] in the distant future, with the aims of scaling the processes in this compact-scale experiment into larger facilities like the Vulcan laser at Rutherford Appleton Laboratories in the United Kingdom.

Part II

Laboratory Astrophysics
Experiments With
Magnetically-Driven Rotating
Plasmas on the MAGPIE
Generator

Chapter 5

Introduction

5.1 Differentially Rotating Plasmas and Outflows in Astrophysical Environments

Many astrophysical environments are dynamically dominated by rotation, as angular momentum is a constant of motion in gravitationally driven systems. Thus, through a process similar to turning an amorphous pizza mass into a flat disk, gas distributions within the interstellar medium gravitationally collapse into flat configurations termed accretion disks accompanying protoplanetary, protostellar, compact objects, amongst others. Many of these systems represent very high-temperature¹ environments leading to strong ionisation of the medium, therefore plasmas dominate the dynamics of such hot disks. It is worthwhile noticing is that they eventually cool down to become purely hydrodynamic neutrally charged configurations (e.g. rings around planets like Saturn) and even planetary systems orbiting a host star, which is an active subject of study in modern astrophysics. In this regard, the nature of plasmas during the high-temperature phase of those systems sets the initial conditions for other lower-temperature configurations.

One may ask, how does the rotation of plasmas in space dominate its phenomenology? Furthermore, the Keplerian orbits impose *differential* rotation of the plasma, *i.e.* a shear-flow. Hydrodynamical instabilities such as the Kelvin-Helmholtz appear when viscous fluids present shear flows, whereas the magneto-rotational instability when $\beta \lesssim 1$ and $Rm \gg 1$. In particular, the Kelvin-Helmholtz instability is known to be closely related to hydrodynamical turbulence, that plays an important role in other dynamical effects such as magnetic dynamos. Both effects affect the transport of angular momentum within accreting systems [31]. Therefore, the study of differentially rotating plasmas represents an outstanding problem in both modern Plasma Physics

¹In protostellar systems, the ultraviolet radiation produces photo-evaporation in the molecular clouds whereas their stellar wind blows through the interstellar medium at high velocity and temperatures. In contrast, high-temperatures are expected in environments nearby compact objects due to the action of the Virial theorem in the presence of strong gravity.

applied to Astrophysics.

Additionally, these systems exhibit another very interesting feature: plasma outflows observed as very long and highly-collimated jets. It is believed that they are accelerated during the accretion process, carrying away part of the rotation of the orbiting system effectively reducing its angular momentum, thus enhancing the accretion rate². Likewise, very long relativistic jets are observed emerging from both stellar mass- and super massive black holes. The precise mechanism that accelerates the outflows is still an open question, however it is believed to be produced during the interaction of the central object with the rotating disk.

5.2 Z Pinch Wire Arrays

The standard Z pinch is a conducting fluid initially carrying an electrical current along one given direction. Defining such direction as the Z axis of the standard cylindrical coordinates, an azimuthally oriented magnetic field is produced, *i.e.* $\mathbf{B} = B\hat{\theta}$. Thus, the Lorentz force raised by the interaction of the azimuthal field with the axial current drives an implosion radially inwards of the fluid, termed *pinch effect*.

There is a ‘Zoo’ of Z pinch-like experiments, but in the framework of this thesis, we are interested in wire arrays: cylindrical arrangements of very thin conducting wires (typically a few micron diameter) connecting electrodes. When the discharge provided by an external driver, usually pulsed high-current³ the solid wires are rapidly heated and turned into current-carrying plasma, leading to a core-corona structure [32]. In the meantime, the electric current produces a local magnetic field around each individual wire, which raises a global magnetic field due to superposition. Thus, the implosion of plasma is driven due to the Lorentz force produced by the interaction of the electrical current passing through the conducting plasma and the global magnetic field.

This implosion is not sudden, but rather a continuous ablation of the wires. Hence, the plasma accelerated by the Lorentz force reaches the center and stagnates producing a hot and dense column. For historical reasons, this accumulation of plasma observed as a dense column on-axis of the array⁴ is termed *precursor plasma*⁵. Once the 50% of the mass from the wires have been ablated, a rapid implosion of the rest of the material takes place producing an intense X ray yield (see *e.g.* [34]), which is termed *stagnation phase*

5.2.1 How to produce a rotating Z pinch

It is straightforward to see that standard Z pinches drive a purely radial implosion. Depending on the geometrical configurations of the wires connecting the electrodes in the electrical current source, it is possible to drive the implosion of the plasma in other directions. For instance, conical

²In protostellar systems this is believed to be a key process in the birth of massive stars

³The typical rise-time in these experiments are between $\sim 10^2 - 10^3$ ns and maximum current $\sim 10^{-1} - 10$ MA.

⁴Moving the precursor off-axis has been studied in [33].

⁵These experiments were initially used to produce high-intensity pulses of X rays. The observations indicated that the column of dense plasma was formed preceding the X ray pulse, and thus it was named precursor

wire arrays produce an axial component of the Lorentz force, which drives the implosion both inwards and upwards [37, 38].

To produce a rotating pinch, a configuration to tailor the magnetic topology has been proposed, where the azimuthal component of the Lorentz force is introduced by the return posts. The idea is to place the return posts close to the array in such way that there is an angular displacement of the center of each post to a respective wire, as shown in Figure 5.1a). Therefore, the local magnetic field around each individual wire will have a perturbation that drives the implosion off-axis. As presented in Figure 5.1, if all the flares implode coherently, the accumulative effect would produce a hollow, differentially rotating precursor plasma [39].

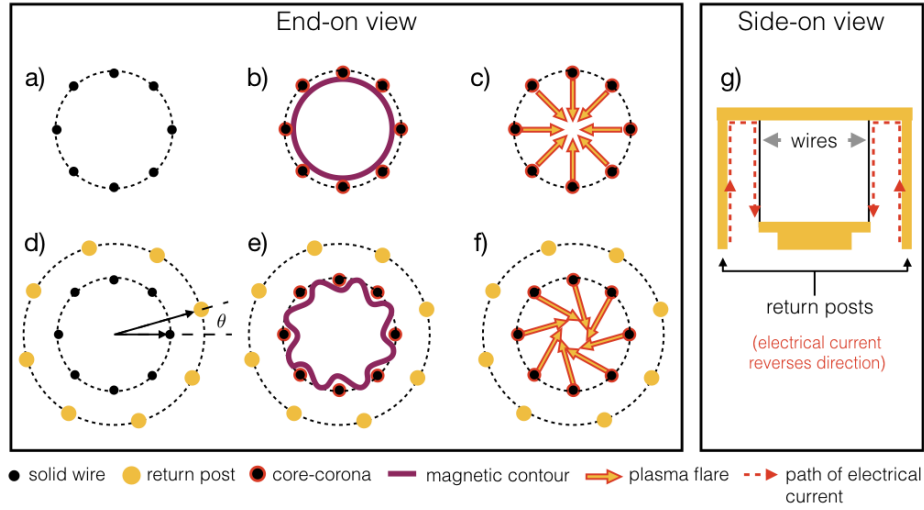


Figure 5.1: Schematic of the rotating Z pinch. The circular dotted contours are left for better visualisation. In a standard wire array: a) the wires are placed equally spaced, b) the magnetic contour is cylindrically symmetrical and, c) the implosion is purely radial. In the rotating Z pinch: d) the return posts are placed nearby the wires and angularly displaced by θ , e) the magnetic contour have a radial component and, f) the implosion is driven off-axis. g) Schematic depiction of the direction of the current through the wires and return posts.

Notice that there are two *a priori* difficulties facing this concept: firstly, the conducting low-density plasma formed during the experiment might shortcut the wires and return posts, thus annihilating the pinch effect and, secondly, the return posts must be thin enough to allow side-on probing.

However, there are advantages when compared to another rotating configuration studied at Imperial College London, which used two oppositely wound coils as electrodes connected by the thin wires [40]. This polar magnetic field is produced during the discharge, subsequently raising an azimuthal component of the Lorentz force. In contrast to that configuration, using the return posts allow us to control the strength and direction of the azimuthal component, this giving us control over the implosion dynamics. Furthermore, we have clear access to the region above the top electrode, therefore, we can diagnose any outflow accelerated during the experiment.

5.3 MHD Scaling and Laboratory Astrophysics

In this section we present the field of *Laboratory Plasma Astrophysics* (although I will be referring to it just as ‘Laboratory Astrophysics’), based upon an important property of MHD: *scale invariance*. I will depict what it means in terms of physical properties and how it allows us to set similarity criteria for comparing laboratory experiments to astrophysical processes.

The very first thing that one must bear in mind is the fact that our current experimental capabilities do not allow us to fully reproduce astrophysical systems. However, it is possible to recreate certain features of such systems, e.g. the macroscopic motion of a differentially rotating plasma, and study them in-detail in a laboratory. Roughly speaking, Astrophysics has historically advanced through three broad methods: observations, analytic theory and numerical simulations, each having its own set of difficulties when tackling open issues. Laboratory Astrophysics brings a new way of gaining insights about complex systems which represent modern outstanding problems⁶.

5.3.1 Euler similarity

In order to compare laboratory and astrophysical plasmas we need a set of rules that allows us to scale one to another (assuming that they are in fact scalable, which will be subject to a *posteriori* evaluation). Let us write the set of Euler MHD equations for a single compressible quasi-neutral conducting fluid, neglecting relativistic and quantum effects⁷, whilst retaining the electric resistivity, heat conduction (by both hydrodynamical and radiative diffusion) and viscosity in the optically thin regime⁸. These equations are [8, 41, 42, 44]:

Mass conservation

$$\frac{\partial \rho}{\partial t} + \nabla \cdot (\rho \mathbf{u}) = 0, \quad (5.1a)$$

momentum equation

$$\frac{\partial}{\partial t}(\rho \mathbf{u}) + \mathbf{u} \cdot \nabla(\rho \mathbf{u}) = -\nabla p + \nabla \cdot \underline{\sigma}_\nu + \frac{\mathbf{j} \times \mathbf{B}}{c}, \quad (5.1b)$$

energy equation

$$\frac{\partial}{\partial t} \left[\rho \left(\varepsilon + \frac{u^2}{2} + E_R \right) \right] + \nabla \cdot \left[\rho \mathbf{u} \left(\varepsilon + \frac{u^2}{2} \right) + p \mathbf{u} \right] = -\nabla \cdot (\mathbf{F}_R + E_R \mathbf{u} + \mathbf{Q} - \underline{\sigma}_\nu \cdot \mathbf{u}) - \mathbf{j} \cdot \mathbf{E}, \quad (5.1c)$$

and the induction equation

$$\frac{\partial \mathbf{B}}{\partial t} = \nabla \times \mathbf{u} \times \mathbf{B} + \eta \nabla^2 \mathbf{B}, \quad (5.1d)$$

where ρ and \mathbf{u} are the mass density and velocity, p the fluid pressure, the stress tensor for a compressible fluid is given by $\underline{\sigma}_\nu \equiv \rho \nu [\nabla \mathbf{u} + (\nabla \mathbf{u})^T] - \frac{2}{3}(\nabla \cdot \mathbf{u})\underline{I}$, whereas $\mathbf{j} \times \mathbf{B}/c$ is the electromagnetic force applied to a quasi-neutral conducting fluid, ε the specific internal energy, E_R is the

⁶Needless to say, Laboratory Astrophysics has difficulties and restrictions of applicability on its own.

⁷However the scaling methods for magneto-radiative-quantum effects in plasmas are very well explained in [42].

⁸This assumption will be supported later.

radiation energy density (hence $E_R \mathbf{u}$ is the radiative enthalpy flux for a optically thin medium), \mathbf{F}_R the radiative energy flux, \mathbf{Q} is the heat flux. Finally, ν the kinetic viscosity, ξ the second coefficient of viscosity (associated with compression), \mathbf{E} , \mathbf{B} the electric and magnetic fields, \mathbf{j} the current density and η the magnetic diffusivity⁹.

Cross *et al.* [42] propose the use of the thermal heat flux in the diffusive limit as a functional form of \mathbf{Q} , *i.e.*

$$\mathbf{Q} = -\frac{\rho\gamma\chi_{th}}{m(\gamma-1)}k_B\nabla T, \quad (5.2)$$

where χ_{th} is the thermal diffusivity, γ the adiabatic index, $m = Am_p$ the ion mass of and k_B the Boltzmann constant. They also propose a cooling function L_Λ as a sink term in the radiation continuity equation in order to approximate it as

$$L_\Lambda = \frac{\partial E_R}{\partial t} + \nabla \cdot [\mathbf{F}_R + E_R \mathbf{u}] \approx \rho\kappa_P\sigma T^4, \quad (5.3)$$

where κ_P is the Planck opacity. Thus, one obtains $\nabla \cdot [\mathbf{F}_R + E_R \mathbf{u}] \approx \rho\kappa_P\sigma T^4$, simplifying the energy equation [42, 43]. I have know the resources to justify studying the optically thin case. The mean-free-path for radiation is given by $\lambda_{rad} = 1/\rho\kappa_P \sim 25$ cm, for $T = 30eV$, $Z = 5$ and $n_e \sim 5 \times 10^{18}$ cm⁻³ which are conservative, although typical, parameters in Z pinch experiments. Given that the plasma has a characteristic scale $l_0 \sim 1$ cm, then $\lambda_{rad} \gg l_0$.

Now we centre our attention in building scale-free equations. Let us take the transformations

$$\mathbf{u} \rightarrow u_0 \hat{\mathbf{u}}, \quad \mathbf{r} \rightarrow l_0 \hat{\mathbf{r}}, \quad t \rightarrow \frac{l_0}{u_0} \hat{t}, \quad (5.4)$$

where the hatted quantities are defined as dimensionless and of order unity, *i.e.* \hat{u} , \hat{r} and \hat{t} , whereas the notted numbers, *i.e.* u_0 and l_0 , are termed *characteristic values* of their respective physical entities. Notice that the transformation for time considers the macroscopic time in terms for the size of the system divided by the velocity, *i.e.* $t_0 \equiv l_0/u_0$. The differential operators are given by

$$\frac{\partial}{\partial t} \rightarrow \frac{u_0}{l_0} \frac{\partial}{\partial \hat{t}}, \quad \nabla \rightarrow \frac{1}{l_0} \hat{\nabla}. \quad (5.5)$$

Accordingly, we can set values for scaling the electric and magnetic fields (\mathbf{B}), current density (\mathbf{j}), density ρ , pressure (p), temperature (T) and specific internal energy(ε). However, as opposed to spatiotemporal scaling –equations (5.4)–, the characteristic values for those quantities *are not arbitrary*, and must be chosen according to the electrodynamical and thermal equations, *i.e.* the set of transformation rules

$$\mathbf{E} \rightarrow E_0 \hat{\mathbf{E}}, \quad \mathbf{B} \rightarrow B_0 \hat{\mathbf{B}}, \quad \mathbf{j} \rightarrow j_0 \hat{\mathbf{j}}, \quad \rho \rightarrow \rho_0 \hat{\rho}, \quad p \rightarrow p_0 \hat{p}, \quad T \rightarrow T_0 \hat{T}, \quad \varepsilon \rightarrow \varepsilon_0 \hat{\varepsilon}, \quad (5.6)$$

is not linearly independent. As derived explicitly in Appendix B, the appropriate transformation rules for \mathbf{E} , \mathbf{j} , T and ε are given by

$$\mathbf{E} \rightarrow \frac{u_0 B_0}{c} \hat{\mathbf{E}}, \quad \mathbf{j} \rightarrow \frac{B_0 c}{4\pi} \hat{\mathbf{j}}, \quad T \rightarrow \frac{p_0/\rho_0}{Am_p k_B (Z+1)} \hat{T}, \quad \varepsilon \rightarrow \frac{1}{\gamma-1} \frac{p_0}{\rho_0} \hat{\varepsilon}, \quad (5.7)$$

⁹Here I have absorbed the factor $c^2/4\pi$ in the definition of η while renaming it. This will proof useful afterwards.

which are fully consistent with the approximations considered in this formalism. Introducing these scaling relations one finds the *dimensionless MHD equations*,

$$\frac{\partial \hat{\rho}}{\partial \hat{t}} + \hat{\nabla} \cdot (\hat{\rho} \hat{\mathbf{u}}) = 0, \quad (5.8a)$$

$$\begin{aligned} \frac{\partial}{\partial \hat{t}}(\hat{\rho} \hat{\mathbf{u}}) + (\hat{\mathbf{u}} \cdot \hat{\nabla})(\hat{\rho} \hat{\mathbf{u}}) = & -\frac{1}{\gamma M^2} \hat{\nabla} \hat{p} + \hat{\nabla} \cdot \left(\frac{1}{Re_\nu} \hat{\rho} \left[\hat{\nabla} \hat{\mathbf{u}} + (\hat{\nabla} \hat{\mathbf{u}})^T - \frac{2}{3} (\hat{\nabla} \cdot \hat{\mathbf{u}}) \underline{\mathbf{I}} \right] \right. \\ & \left. + \frac{1}{Re_\xi} (\hat{\nabla} \cdot \hat{\mathbf{u}}) \underline{\mathbf{I}} \right) + \frac{2}{\gamma M^2 \beta} \hat{\nabla} \times \hat{\mathbf{B}} \times \hat{\mathbf{B}}, \end{aligned} \quad (5.8b)$$

$$\begin{aligned} \frac{\partial}{\partial \hat{t}} \left[\hat{\rho} \left(\frac{1}{\gamma(\gamma-1)M^2} \hat{\varepsilon} + \frac{\hat{\mathbf{u}}^2}{2} \right) \right] + \hat{\nabla} \cdot \left[\hat{\rho} \hat{\mathbf{u}} \left(\frac{1}{\gamma(\gamma-1)M^2} \hat{\varepsilon} + \frac{\hat{\mathbf{u}}^2}{2} \right) + \frac{1}{\gamma M^2} \hat{p} \hat{\mathbf{u}} \right] = & \\ & -\frac{1}{\Pi_{thin}} \hat{\rho} \hat{T}^4 - \frac{2}{\gamma M^2 \beta} \hat{\mathbf{j}} \cdot \hat{\mathbf{E}} + \hat{\nabla} \cdot \left\{ \frac{1}{Pe} \frac{\gamma}{\gamma-1} \hat{\rho} \hat{\nabla} \hat{T} \right. \\ & \left. + \left[\frac{1}{Re_\nu} \hat{\rho} \left(\hat{\nabla} \hat{\mathbf{u}} + (\hat{\nabla} \hat{\mathbf{u}})^T - \frac{2}{3} (\hat{\nabla} \cdot \hat{\mathbf{u}}) \underline{\mathbf{I}} \right) + \frac{1}{Re_\xi} (\hat{\nabla} \cdot \hat{\mathbf{u}}) \underline{\mathbf{I}} \right] \cdot \hat{\mathbf{u}} \right\}, \end{aligned} \quad (5.8c)$$

$$\frac{\partial \hat{\mathbf{B}}}{\partial \hat{t}} = \hat{\nabla} \times \hat{\mathbf{u}} \times \hat{\mathbf{B}} + \frac{1}{R_m} \hat{\nabla}^2 \hat{\mathbf{B}} \quad (5.8d)$$

In this case, we have explicitly found the radiative single-fluid MHD dimensionless parameters, *i.e.* the hydrodynamical Reynolds numbers Re_ν and Re_ξ , magnetic Reynolds number R_m , Peclet number Pe and thin radiation number Π_{thin} , Mach number M and plasma β . Their functional forms are defined as

$$\begin{aligned} Re_\nu &\equiv \frac{u_0 l_0}{\nu}, & Re_\xi &\equiv \frac{\rho_0 u_0 l_0}{\xi}, & R_m &\equiv \frac{u_0 l_0}{\eta}, & Pe &\equiv \frac{u_0 l_0}{\chi_{th}}, \\ \Pi_{thin} &\equiv \frac{u_0^3}{\kappa_P l_0 \sigma T_0^4}, & M &\equiv \frac{u_0}{c_s}, & \beta &\equiv \frac{p_0}{B_0^2 / 8\pi}. \end{aligned} \quad (5.9)$$

Notice that, by construction, with exception to all dimensionless parameters, every hatted term in (5.8) is always of order unity and thus, the evolution of the system is determined by the size of the dimensionless parameters.

In other words, this means that the dynamical evolution of the system is described by the regime at which the dimensionless parameters are to respect to unity (*i.e.* $\ll 1$, $\gg 1$, ~ 1), regardless of the natural spatial and temporal scales of the system. Therefore, one concludes that *if two systems share their dimensionless parameters in the same regime as compared to unity, their evolution will be similar.*

There are two possible ways of interpreting this result. On the one hand, that in order to have *exact* scalability it is necessary that all the values of their dimensionless parameters match. On the other hand, if the values of the dimensionless parameters are sufficiently large for *both* systems, which is certainly the case for astrophysical contexts, then the set of equations (5.8) calculated for both systems effectively captures the properties of the ideal-limit of MHD¹⁰, and thus are compa-

¹⁰I will refer to the ideal-limit of MHD when the dissipation dimensionless parameters (Re , R_m and Pe) are much greater than unity and may be treated as infinite, *i.e.* when dissipation is negligible. The scalability will break outside this regime as I discuss in the next part.

table.

In order to relate the dimensionless parameters with physical quantities than can be actually measured in an experiment, we require functional forms of the dissipation coefficients. Fortunately, [42] provides us the expressions for the viscosity, magnetic and thermal diffusivity, respectively.

$$\nu = \min \left\{ \begin{array}{l} 3.3 \cdot 10^{-5} A^{1/2} T^{5/2} Z^{-4} \rho^{-1} \Lambda^{-1} \\ 2.8 \cdot 10^{43} A^{-5/2} T^{-1/2} Z^{-2} \rho^2 \Lambda B_0^{-2} \end{array} \right\}, \quad (5.10)$$

$$\eta = 2.4 \cdot 10^5 T^{-3/2} Z \Lambda, \quad (5.11)$$

$$\chi_{th} = \min \left\{ \begin{array}{l} 3.3 \cdot 10^{-3} A T^{5/2} Z(Z+1) \rho^{-1} \Lambda^{-1} \\ 8.6 \cdot 10^9 A^{1/2} T Z^{-1} B_0^{-1} \end{array} \right\}, \quad (5.12)$$

where, typically in wire-based Z pinch experiments $T_e = T_i \equiv T$ ($[T] = \text{eV}$) and Z is the effective ionisation degree. Whereas, the Planck opacity κ_P is dependant on the material and are tabulated. For aluminium it has the form

$$\kappa_P = 6.01 \cdot 10^8 T^{-2.42} \rho^{0.48}. \quad (5.13)$$

Additionally, a model for the ion speed of sound in a polytropic plasma written in terms of its temperature is given by [45]

$$c_s = 9.79 \cdot 10^5 A^{-1/2} (\gamma Z T)^{1/2}, \quad (5.14)$$

γ being the polytropic exponent.

One should wonder how do the physical parameters from one system map onto the other [8, 41]. Setting the superscripts (1) and (2) to denote those quantities in the context of two different systems, the scaling relations are

$$u_0^{(2)} = a u_0^{(1)}, \quad l_0^{(2)} = b l_0^{(1)}, \quad \rho_0^{(2)} = k \rho_0^{(1)}, \quad p_0^{(2)} = d p_0^{(1)}, \quad B_0^{(2)} = f B_0^{(1)}, \quad (5.15)$$

where a , b , k , d and f are scaling constants. Therefore, according to the discussion following (5.7), other quantities scale from one system to the other as

$$t_0^{(2)} = a^{-1} b t_0^{(1)}, \quad E_0^{(2)} = a f E_0^{(1)}, \quad j_0^{(2)} = f j_0^{(1)}, \quad T_0^{(2)} = d k^{-1} T_0^{(1)}, \quad \varepsilon_0^{(2)} = d k^{-1} \varepsilon_0^{(1)}. \quad (5.16)$$

This process provides us a very powerful tool: set limitations on *what* we are reproducing in a laboratory. Take the time scaling, for example. We may want to know how much evolution time we are effectively ‘simulating’ with our experiment, placing constraints on the validity of the scaling. It might be the case that the time scaling transformation may imply that our ‘simulation time’ is longer than the actual ‘lifetime’ of the astrophysical object. Here one must remind oneself that Laboratory Astrophysics does not *fully* reproduce astrophysical systems. Furthermore, the scaling relations allow us to map the initial conditions problem from one system to the other, which I will not discuss further here and it is very briefly described in [41].

Failure of MHD scale invariance

The fact that the set of equations (5.9) is scale-free implies that the MHD equations are self-similar. However, there is a spatial scale at which self-similarity must break down. To point out why this is an important feature take the case of other self-similar theories, such as electrodynamics. In the case of Maxwell equations, the wave equation is self-similar, *i.e.* all monochromatic electromagnetic waves are scaled versions of one another. If the energy it carries is proportional to the square of its amplitude, then it is possible to fill it with an arbitrary number of smaller waves so that any given wave can carry an arbitrary amount of energy, leading to the ultraviolet catastrophe¹¹. Of course, now we know that in fact the energy of the wave scales with its frequency and therefore quantum mechanics limits the scale invariance of electrodynamics, as a photon with shorter wavelength carry more energy.

Likewise, self-similarity in incompressible neutral fluids allow turbulence to energise smaller spatial scales through turbulent eddies breaking into smaller eddies in a process termed Kolmogorov cascade. When the cascade reaches the viscous scale, the fluid stops being self-similar, *i.e.* the Euler equations are no longer a good description of the hydrodynamics, and kinetic energy is dissipated into heat.

The latest point is useful to understand at which spatial scale MHD self-similarity breaks down, given that at certain regime of size and velocity, dissipation processes begin to dominate the dynamics. This is equivalent to have the dissipation dimensionless numbers Re_ν , R_m and Pe ¹² reaching values of order unity.

In fact, an interesting property about these dimensionless numbers is that the regime at which they lie tells us properties about the fluid. In general, just by stating their regime (compared to unity) instantly brings insights about the properties of the fluid. First notice that both Re , Rm and $Pe \propto u_0 l_0$, and scales as the inverse of a dissipative effect (*i.e.* viscosity, magnetic and thermal diffusivity, respectively). Therefore one concludes that they are in fact the ratio of inertial-to-dissipation processes.

The fact that length and velocity are at equal footing can be interpreted in the following way: consider a case where dissipation is negligible and so the dimensionless number is $\gg 1$. It either means that the size of the system is large enough such that dissipation occurs on much smaller scales and it has no dynamical influence and/or the system evolves fast enough so dissipation is too slow to be considerable.

More rigorously, consider a macroscopic spatial scale to describe the fluid given by $l^* \equiv \rho/|\nabla\rho|$ and a perturbation λ . The temporal scale at which that perturbation is dissipated is $\tau \sim \lambda^2/\nu$ and it dominates when $\tau < l^*/u_0$, which is equivalent to the condition $\lambda < Re^{1/2}l^*$. Similarly, for thermal dissipation, $\lambda < Pe^{1/2}l^*$ [41]. Thus, setting the minimum scales from which the set of MHD equations are scale invariant.

¹¹I first heard of this fascinating interpretation of the ultraviolet catastrophe studying from the first lecture of Neil Turok's course on General Relativity for the 2014 class of Perimeter Scholars International at the Perimeter Institute for Theoretical Physics.

¹²For simplicity I now neglect the bulk Reynolds number Re_ξ , since it is analog to Re_ν .

The very subtle assumption underneath the scalability criteria in Laboratory Astrophysics is that the dissipative dimensionless numbers must be much greater than unity, in order to fulfill the MHD scale invariance. In other words, if the astrophysical plasmas would have been dominated by dissipation, there is no possible way to scale them down into laboratory experiments. Happily, space is very big and violent, therefore both l_0 and u_0 are usually *astronomically* large.

5.3.2 An order-of-magnitude method of quantifying errors in dimensionless parameters

In the context of pulsed, dense plasmas there are several fundamental quantities that are very hard to measure with high degree of precision, *e.g.* Z , T_e and ρ . One can notice that the expressions for dimensionless parameters, *i.e.* equations (5.10) – (5.12), have a power-law dependence on such ‘hard-to-measure’ quantities, therefore one expects an according dependence on errors in estimations. Let me depict why this is relevant: consider a given dimensionless parameter, namely D , that must satisfy $D \gg 1$ for scalability purposes. After making the experiment we find $D \sim 10^2$, which indeed satisfies the criterion. However, what happens if our estimations are off so that it is plausible that $D \sim 1$? Does the scalability still hold? In other words, *how does a given factor of error in the estimation of characteristic quantities change the final value of the dimensionless parameters?*

As a disclaimer, in some occasions within this section I will admittedly drop the rigorous procedures followed in sections above, in the same spirit described in Prof Sanjoy Mahajan’s TEDx talk¹³, *in problem solving as in street fighting, rules are for fools*. As it is very much the case for studies based upon MHD scaling (*e.g.* [46, 47]), where rough estimations are ubiquitously found, I intend to give space for applying some well-educated estimations based upon experience and other authors’ work to add error bars to our calculations. Thus, the problem I address here is the order-of-magnitude propagation of scale factors and quantify, within certain degree of confidence, how good the scalability criteria is satisfied. To the best of my knowledge, there is no publication taking this into account.

Let us start by taking the equations for dimensionless parameters written as power-laws depending on a handful of parameters, *i.e.* from (5.9) and (5.10) - (5.14)

$$\begin{aligned} Re_\nu &\propto u_0 l_0 A^{-1/2} T_0^{-5/2} Z^4 \rho_0, & Rm &\propto u_0 l_0 T_0^{3/2} Z^{-1} \Lambda^{-1}, & Pe &\propto u_0 l_0 A^{-1} T_0^{-5/2} Z^{-2} \rho_0 \Lambda, & (5.17) \\ \Pi_{thin} &\propto u_0^3 l_0^{-1} T_0^{-1.08} \rho_0^{5.2}, & M &\propto u_0 A^{-1/2} Z^{1/2} T_0^{1/2}, & \beta &\propto \rho_0 Z T_0 B_0^{-2}. \end{aligned}$$

At this point we notice that calculating the propagation of errors given unaccurate estimates depends of 8 different variables: u_0 , l_0 , T_0 , Z , A , ρ_0 , B_0 and Λ . Seemingly, it is impractical to throw ourselves into the endeavour of computing directly, as it would be an exhausting homework. Hence, we would like to reduce the complexity of the problem.

¹³*Rote Learning Fragments of the World*, California Institute of Technology, 2011.

The first step of this method is *reduction of variables*: take a dimensionless number D which is a power-law function of m variables $\{\alpha_j\}$, $j = 1, 2, \dots, m$, i.e. $D = D(\{\alpha_j\})$. The claim (and hope) is that the set of $\{\alpha_j\}$ is reducible. This might be for two reasons: on the one hand, there a subset of variables $\{\alpha_i\}$ can have very well-determined values. Therefore there is nearly no uncertainty on its calculation and it does not contribute to the error. I name the set $\{\alpha_i\}$ *fixed variables*¹⁴. On the other hand, there are *related variables*, which are two (or more) separate quantities that are related through a power-law, thus it is possible to plug such relation into the functional form of D to eliminate one variable. Thus, from the original set $\{\alpha_j\}$, if we have found p fixed variables and q expressions for related variables, the dimension of D is reduced from a m -dimensional space to a n -dimensional space, where $n = m - (p + q)$.

Up until now, $m = 8$. The most straightforward fixed variable is the ion mass number A , since there is very little inaccuracy on its value, say $1/10$. This is because, according to the fabricant (California Fine Wire Company) they are 99.9% pure, therefore it is reasonable to assume that we are not unlucky so that the wires we used are heavily contaminated and/or such that they are populated by isotopes having mass numbers much larger than 27 or much lower than 25.

The Coulomb logarithm $\Lambda \equiv \ln(1.5 \cdot \pi^{-1/2} e^{-3} (k_B T)^{3/2} Z^{1/2} (1+Z)^{-1/2} n_e^{-1/2})$ is subject of argue. By its very definition, it is a related variable. However it is not a power-law, rather a logarithmic relation. Thus, the errors in the estimates of the independent variables propagate linearly rather than power-laws within Λ , hence I regard it as a fixed variable constrained to have a value ~ 15 .

The mass density ρ_0 can be broken down into more fundamental quantities, i.e. $\rho_0 = A m_p n_{e0} Z^{-1}$, where $m_p = 1.67 \times 10^{-24}$ g is the mass of the proton and n_{e0} is the characteristic electron density, an observable. Similarly, it is possible to estimate the average ionisation Z given a temperature T_0 . In the style of Sanjoy Mahajan [48] and Peter Goldreich [49], we make the rough approximation and consider a hydrogenic ion plasma having ionisation energies given by the Bohr levels, i.e. $E_i \approx Z^2 E_H$, $E_H = 13.6$ eV. Additionally, the effective energy for Coulomb processes is given by $3k_B T_e$ [44], therefore if the ionisation and effective energies are equal to produce ionisation, then $Z = (3k_B T_e / E_H)^{1/2}$. Even though this is a sufficiently good approximation [44], there are more refined models to calculate the ionisation of the medium, e.g. the Thomas-Fermi model, but for the purpose of this thesis I will not enter into such complicated realm.

Introducing these considerations we have reduced the problem. Above we found 2 fixed variables and 2 relations between variables. Therefore, we have found new and simpler power-law relations for the dimensionless parameters depending on u_0 , l_0 , T_0 , B_0 and n_{e0}

$$\begin{aligned} Re_\nu &\propto u_0 l_0 T_0^{-1} n_{e0}, & Rm &\propto u_0 l_0 T_0, & Pe &\propto u_0 l_0 T_0^{-4} n_{e0}, & (5.18) \\ \Pi_{thin} &\propto u_0^3 l_0^{-1} T_0^{-3.68} n_{e0}^{5.2}, & M &\propto u_0 T_0^{3/4}, & \beta &\propto n_{e0} T_0 B_0^{-2}. \end{aligned}$$

This is precisely what we want! This is, in a way, a description of the plasma based upon its most fundamental dynamically relevant parts: velocity, size, temperature, electron number density

¹⁴These are in fact contradictory terms. Bear in mind, however, that these quantities might in fact vary during the experiment or have a given degree of inaccuracy. The point I am stressing here is that such variation is small. It is certainly imaginable cases when declaring a variable as fixed can be subject of debate.

and magnetisation.

The next step of the method is *constraint values*. Here one must estimate maximum and minimum possible values for the n independent parameters $\{\alpha_j\}$. These values will be key to set the limits of the error bars. Set the suscripts $+$ and $-$ to denote them maximum and minimum values for any given quantity, respectively. Then write *scaling relations* between those extreme values using powers of 10, *i.e.* expressions of the kind $\alpha_{j+} = 10^\beta \alpha_{j-}$. In many cases the maximum and minimum values will not differ so greatly. This is not a problem because one can always find scaling laws and then use logarithms of the scaling coefficients. For any practical purpose, this is in fact what we will always do. Now I constraint values on u_0 , l_0 , T_0 , n_{e0} and B_0 , finding the scaling relations

$$u_{0+} = xu_{0-} \implies u_{0+} = 10^{\log(x)} u_{0-}, \quad (5.19a)$$

$$l_{0+} = yl_{0-} \implies l_{0+} = 10^{\log(y)} l_{0-}, \quad (5.19b)$$

$$T_{0+} = zT_{0-} \implies T_{0+} = 10^{\log(z)} T_{0-}, \quad (5.19c)$$

$$n_{e0+} = wn_{e0-} \implies n_{e0+} = 10^{\log(w)} n_{e0-}, \quad (5.19d)$$

$$B_{0+} = gB_{0-} \implies B_{0+} = 10^{\log(g)} B_{0-}. \quad (5.19e)$$

This will proof useful for the next step, *relating extreme values*. Back to our generic dimensionless parameter $D = D(\{\alpha_j\})$. Notice that, given that the dependence of D with the physical quantities $\{\alpha_j\}$ are power-laws, the maximum and minimum values of D , *i.e.* D_+ and D_- can be computed by evaluating D with the appropriate extreme value of each α_j . This must be done with some care. Let γ_j be the exponent of the power-law dependence of D with respect to the physical parameters, *i.e.*

$$D \propto \prod_{j=1}^n \alpha_j^{\gamma_j}, \quad (5.20)$$

thus, D_+ is given by taking α_{j+} when $\gamma_j > 0$. Conversely, when $\gamma_j < 0$, then the maximum value is obtained by taking α_{j-} . The logic is analog to obtain D_- . Noting that $\text{sign}(\gamma_j) = |\gamma_j|/\gamma_j$, this can be written in compact form

$$D_+ \propto \prod_{j=1}^n \alpha_{j,|\gamma_j|/\gamma_j}^{\gamma_j} \quad (5.21)$$

$$D_- \propto \prod_{j=1}^n \alpha_{j,-|\gamma_j|/\gamma_j}^{\gamma_j} \quad (5.22)$$

Now, we can relate the extreme values of D using a scaling relation, *i.e.* .

$$D_+ = \lambda D_- \quad (5.23)$$

Notice that now the problem of finding the limits of the error bars has reduced to half the labor, because, due to the scaling relation (5.23), it is necessary to compute only one of the extreme values of D . The other can be very easily found by using the fact that $\lambda = \prod_{j=1}^n 10^{\beta_j}$. Moreover, this really means that we have to evaluate the sum of exponents β_j .

Let see this in action. Plugging the set of relations (5.19) into the expressions for dimensionless parameters (5.18) with the corresponding extreme value. Then we write the scaling form of each highest dimensionless parameter in terms of the smallest possible value, obtaining

$$Re_{\nu+} = 10^{\log(x)+\log(y)+\log(z)+\log(w)} \times Re_{\nu-}, \quad (5.24a)$$

$$Rm_+ = 10^{\log(x)+\log(y)+\log(z)} \times Rm_-, \quad (5.24b)$$

$$Pe_+ = 10^{\log(x)+\log(y)+4\log(z)+\log(w)} \times Pe_-, \quad (5.24c)$$

$$\Pi_{thin+} = 10^{3\log(x)+\log(y)+3.68\log(z)+5.2\log(w)} \times \Pi_{thin-}, \quad (5.24d)$$

$$M_+ = 10^{\log(x)+0.75\log(z)} \times M_-, \quad (5.24e)$$

$$\beta_+ = 10^{\log(z)+\log(w)+2\log(g)} \times \beta_-, \quad (5.24f)$$

which delivers a new set of scaling relations.

The last part of this method is finding the *reference value* of the dimensionless parameter, which I will denote as a starred quantity. Typically D_+ and D_- will disagree in several orders-of-magnitude. To avoid D_+ dominating over D_- , I propose that one should take the *geometric mean* to obtain the reference value, i.e. $D^* \equiv (D_+D_-)^{1/2} = \lambda^{1/2}D_-$. Finally, if $D^* = 10^\delta$ and $D_- = 10^\epsilon$ the dimensionless number is

$$D = 10^{\delta \pm (\delta - \epsilon)}. \quad (5.25)$$

This is the form in which the dimensionless parameter D should be presented considering its error bars. The spirit behind writing the dimensionless parameter in this form is to deliver a quick sense of the broad regime at which it can take values.

Explicitly, in terms of the dimensionless parameters.

$$Re_\nu^* \equiv (Re_{\nu+}Re_{\nu-})^{1/2} = 10^{(\log(x)+\log(y)+\log(z)+\log(w))/2} \cdot Re_{\nu-}, \quad (5.26a)$$

$$Rm^* \equiv (Rm_+Rm_-)^{1/2} = 10^{(\log(x)+\log(y)+\log(z))/2} \cdot Rm_-, \quad (5.26b)$$

$$Pe^* \equiv (Pe_+Pe_-)^{1/2} = 10^{(\log(x)+\log(y)+4\log(z)+\log(w))/2} \cdot Pe_-, \quad (5.26c)$$

$$\Pi_{thin}^* \equiv (\Pi_{thin+}\Pi_{thin-})^{1/2} = 10^{(3\log(x)+\log(y)+3.68\log(z)+5.2\log(w))/2} \cdot \Pi_{thin-}, \quad (5.26d)$$

$$M^* \equiv (M_+M_-)^{1/2} = 10^{(\log(x)+0.75\log(z))/2} \cdot M_-, \quad (5.26e)$$

$$\beta^* \equiv (\beta_+\beta_-)^{1/2} = 10^{(\log(z)+\log(w)+2\log(g))/2} \cdot \beta_-. \quad (5.26f)$$

Thus, the set (5.26) delivers formulae to quickly compute central values and error bars for dimensionless parameters, having reducing the problem to fully calculate the lowest possible value for such parameters and some logarithms. Needless to say, one could leave the maximum values as independent variable without loss of generality.

Furthermore, this method might be of interesting to design experiments, as one might rapidly try different configurations to adjust the regimes of the parameters, possibly with the aims of narrowing them.

5.4 Summary

In this chapter I reviewed the motivation behind this part of the thesis, as rotating plasmas are very common in astrophysical environments and understanding their properties represents an outstanding issue. Afterwards I reviewed basic principles of Z pinch plasma experiments, leading to a state-of-the-art configuration to produce a rotating Z pinch. Ideally, this plasma experiment can be used to study in detail the physical properties of plasmas in astrophysical environments

In order to compare the two systems (laboratory and astrophysical plasmas), an extensive discussion about the theoretical framework of Laboratory Plasma Astrophysics was given. At the very core of the theory lies the scale invariance of ideal magnetohydrodynamics, which allow us to compare any two given systems as long as their dissipation timescales are much longer than the dynamical times and their characteristic spatial scale is much larger than the dissipative length. Thus, I constructed the dimensionless Euler MHD equations, which incorporated additional dimensionless parameters that are not linked with dissipation, like the Mach number and the plasma β . From this I claimed the central argument in laboratory astrophysics, termed Euler similarity: two systems are said to have similar evolution if their respective dimensionless parameters in the same regime as compared to unity. Hence, the problem of laboratory astrophysics is transformed into matching regimes between dimensionless parameters.

However, calculating dimensionless parameters is a hard labor. This is because the physical quantities from which they are constructed are frequently measured within large experimental uncertainty. Addressing this issue, I proposed a method to compute the dimensionless parameters required to test the similarity between laboratory and astrophysical plasmas, including error bars that quantify the effect of inaccuracies in the final computation of dimensionless parameters.

In the next chapter I will review the experimental set-up, including the MAGPIE pulsed-power generator where we performed the experiments, the hardware at MAGPIE allows us to produce the rotating pinch, the diagnostic techniques employed and the synchronisation settings to obtain the data.

Chapter 6

Experimental Set-up

Now I explain the experimental techniques and equipment used to produce and measure the rotating Z pinch. Many of the diagnostics employed here are very common in high-energy-density experiments and were reviewed in Part I. Thus, I will only explain the micro-channel plates as devices to measure the UV/XUV plasma self-emission.

Since the experiments were carried overseas, I will only summarise the basic concepts behind the pulsed-power driver used during this investigation. This is by no means an extensive review of its components and principles of operation. Likewise, the mechanism by which one synchronises the experiments with MAGPIE will not be explained. However, I will describe the hardware in certain detail.

6.1 The MAGPIE Pulsed-Power Generator

The Mega Ampere Generator for Plasma Implosion Experiments (MAGPIE) based at Imperial College London is the largest academic facility of its kind worldwide. It is designed to produce extreme high-energy-density (HED) conditions using a pulsed high-electrical-current discharges: 1.2 MA in 240 ns, resulting in a ~ 1 TW output power to drive the implosion of wire-based Z pinches and liners, having application in radiation physics, laboratory astrophysics, basic HED physics studies, amongst others.

The basic functioning of the driver is as follows: the energy is stored in 96, $0.7 \mu\text{F}$ capacitors distributed evenly in 4 Marx capacitor banks. Each bank is charged by two 100 kV power supplies. Once the discharge is initiated, the capacitors are connected in series through a process termed *Marx erection*, increasing the output voltage up to 2.4 MV. The pulse is then carried by pulse-forming lines (5Ω , 100 ns). Using a line-gap-trigger, the pulse is later discharged to the transfer transmission line (1.25Ω , 60 ns) which delivers the electric current to the load through a magnetically insulated transmission line (MITL) [50]. The final performance of the generator is monitored by two separate Rogowski coils placed surrounding different return posts within the vacuum chamber.

Finally, in our experiment, the load consists of a 16 mm diameter, 10 mm height, standard cylindrical array made of 8 aluminium (Al) wires, each 40 μm diameter. An specially designed hardware was designed by Jack Hare and then laser-cut in order to place 8, 1 mm diameter stainless steel rods at a ~ 3 mm from the array. The angular displacement between the wire and its corresponding return post, i.e. the closest neighboring steel rod, is 13° . The angular positioning of the hardware is achieved using an alignment key that allow the experimenter to center the electrodes and fix the notches with respect to the return posts. A side-on schematic is presented in Figure 6.3.

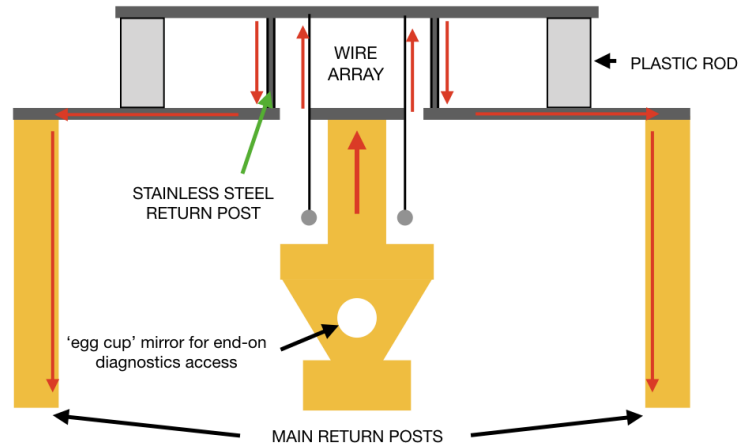


Figure 6.1: Schematic image of the hardware. The red arrows indicate the path of the electrical current.

The current passes from the central cathode through the wires. Then, a secondary electrode that is connected to the anode, and supported by thick plastic rods, carries the current into the return posts downwards, thus reversing the direction of the electrical current. Finally, the current is driven through 4, 22 mm diameter main return posts. Two mutually inverted Rogowski coils¹ measure the current at two different main return posts.

6.2 Diagnostics

In this part I will explain the principles of two self-emission diagnostics. These do not represent the complete set of diagnostics employed in the experiments. However, the remaining diagnostics were explained in the Chapter 2. Thus, this section is complemented with the discussion above. Notice that in this section the discussion will be rather brief. This is because, as opposed to interferometry, the self-emission diagnostics are extremely simple in their foundations. However, I intend to give a sufficiently deep discussion about the principles of functioning.

¹Rogowski coils are standard electric diagnostics in pulsed-power. They are placed onto an amperian loop surrounding a conductor that carries a non-steady electrical current. Thus, from Faraday law a voltage proportional to dI/dt is generated in the coil and measured in the oscilloscope. More details can be found in [20].

6.2.1 Optical fast framing

The Ultra UHSi 12/24 (Invisible Vision Company) is a state-of-the-art fast frame intensified ICCD camera, which can take up to 12 frames with an interframe up to 5 ns, a 5 ns maximum time resolution and a jitter ± 2.5 ns. The CCD is a 4872×3248 array of $7.4 \mu\text{m}$ pixels. The gain of the intensifier can be set up to 5000, however in the experiments it was set to a conservative 80. The exposure time is 5 ns, *i.e.* the best temporal resolution available. The optical fast framing camera is triggered using a 5 V TTL. More details can be found in the datasheet [53]. The spatial calibration was made by taking images of a M3 bolt backlighted using a torch.

6.2.2 Micro-channel plate imaging

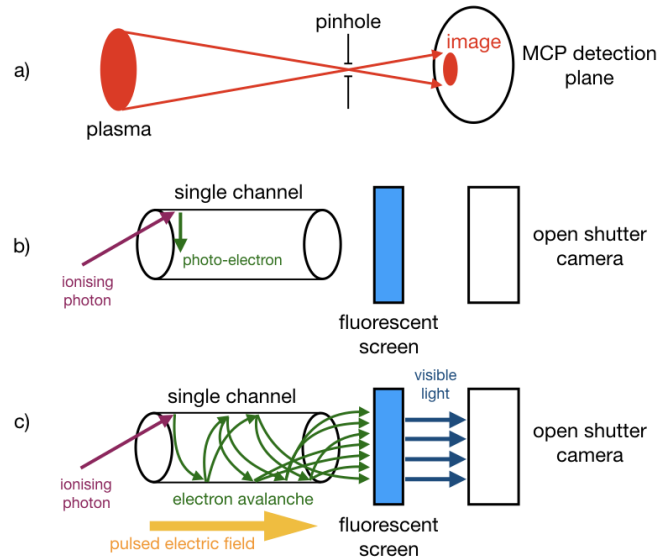


Figure 6.2: Schematic figure of the MCP principle of function. a) An image of the plasma onto the detection plate is formed, b) the ionising self emission produces photo-electrons on the detection plate, c) when the pulsed voltage is applied, the initial photo-electrons are accelerated into the micro-channel producing an electron avalanche.

Micro-channel plates (MCP) are photo-multipliers that capture the self-emission of the plasma in the UV/XUV band. Unlike the images formed in the ICCD, the MCP use pinholes to delimit the spatial resolution of the image. Thus, a small aperture² in front of the detecting surface of the MCP limits the direction from which the propagating rays departing from a given region of the plasma can arrive to the detection plane, as shown in Figure 6.2a). Additionally, the magnification is determined by the ratio between the pinhole-to-MCP distance (f_1) and the object-to-pinhole (f_2), *i.e.* $M = f_2/f_1$.

The gain of photo-multiplication is given by a high-voltage pulse. The principle of functioning is

²Smaller compared to the probed object, but larger than the diffraction limit.

rather simple. Consider a plasma emitting UV/XUV radiation such that an image is formed in the conducting detection surface of the MCP during the experiment. Due to photoelectric emission, photo-electrons are emitted when the photons are energetic enough to overcome the work function of the material, as depicted in Figure 6.2b). However, once the high-voltage pulse is activated in the MCP the electrons are conducting through small channels in the device. The gain of energy of each electron allow them to extract electrons from the walls of each channel, which are also accelerated through the MCP. Thus, as illustrated in Figure 6.2c), at the end of the avalanche process, the MCP increased the number of electrons produced by the UV/XUV radiation of the plasma. Finally, a fluorescent screen shines when the avalanche of electrons reaches it. An open shutter Canon camera captures the emission from the MCP. Hence, the temporal resolution of the MCP is determined by the width of the high-voltage pulse.

A set of two different 4 frame MCP's. However, one of the MCP which had a dead frame, thus we can obtain 7 images. The alignment is a standard procedure at MAGPIE. Using a simple in-house code, we calculated the magnification of each one. MCP A (3 frames) was prepared for $M \sim 0.78$ with a $70 \mu\text{m}$ pinhole diameter, whereas for image formation onto MCP B (4 frames) a $150 \mu\text{m}$ pinhole diameter and a magnification $M \sim 0.59$. MCP A was set to have better spatial resolution, *i.e.* larger magnification and smaller pinhole, at the cost of observing less of the inferior part of the experiment and capturing less light emitted from the plasma. In contrast, MCP B had a lesser magnification to observe the dynamics of the experiment globally, including any discharge occurring underneath the array and larger pinholes to ensure the plasma imaging.

6.3 Distribution of Diagnostics

The vacuum chamber at MAGPIE has 16 ports, from which 14 allow access for diagnostics (two are reserved for the vacuum pumps) at three 'stories' from 2" windows. Although the MITL is placed underneath the chamber, end-on probing is possible due to an egg cup' supporting the central electrode and holding a dispensable mirror within it. Thus, laser beams and/or self-emission can propagate through/from the array, being reflected by the mirror to any of the chamber's windows.

For consistency, the MCP cameras are placed at opposed positions of the chamber, thus no further assumptions of the experimental axial symmetry is required for crossed analysis.

An Mach-Zehnder interferometer was mounted with the reference beam passing outside the vacuum chamber (similar to the set-up on Part I) for end-on electron density measurements. The laser beams are produced by an Nd:YAG laser 355 nm and 532 nm wavelength, 500 ps FWHM and recorded onto neutrally filtered, 1.3 s open shutter Canon cameras. Collinear to the laser beams the optical fast frame camera is set. Using a LMR2/M filter that blocks 355 nm and 532 nm wavelength the laser beams are kept away from the intensified CCD.

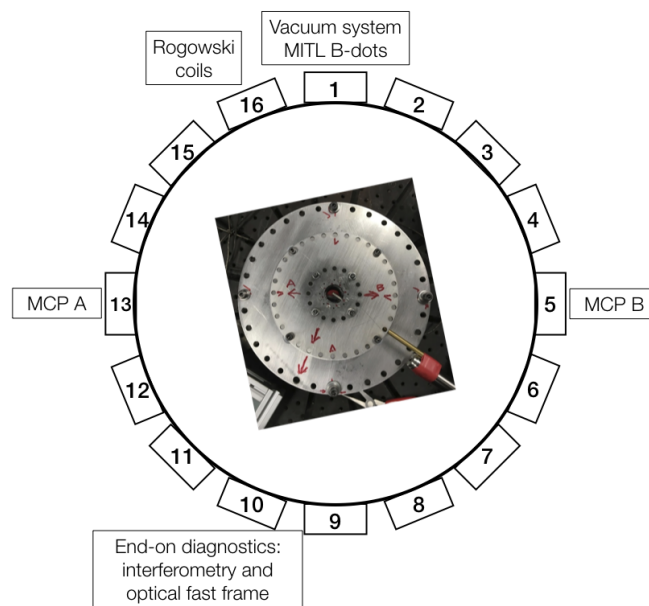


Figure 6.3: Schematic image of the diagnostics distribution inside the vacuum chamber.

Chapter 7

Results

During this chapter I present the experimental results and their contrast with numerical simulations using the GORGON code. Now I will differentiate between two features of the experiment: the rotating plasma within the array, *i.e.* between the electrodes, better described by the r and θ plane of cylindrical coordinates and; the axial outflow, which is projected onto the r and z plane. It should be noted that the data presented here was gathered during a single shot.

I finally discuss the scalability of both the rotating plasma and outflow to astrophysical environments by using some characteristic parameters found in accretion disks and the jets typically associated with them.

7.1 Rotating Plasma

Data from the optical self-emission is presented in Figure 7.1. We observe that the characteristic timescale at which the plasma reaches the region near the centre of the array is $t \sim 160$ ns, thus a rough estimation for the lower constraint of the velocity of the flares is $v_{abl} \gtrsim 5 \cdot 10^6$ cm/s. At $t = 164$ ns it is observed that the flares do propagate off-axis, although not in a symmetrical form. This is due to the misplacement of certain wires/return posts and overall differences in the ablation rates due to experimental errors. This will be confirmed in the following section.

At 239 ns we observe the formation of a rather stable structure at the centre of the array: a hollow star-shaped plasma. The sharp edges at the outermost part is most likely produced by the interaction of counter-propagating parts of the plasma flares. These flares also sustains the ring-shape of the configuration, as it exerts pressure to the central ring. Interestingly, the hollow centre persists for rather characteristic timescales $\Delta t \sim 100$ ns.

Let us evaluate further the meta-stability of this structure. Due to density gradients, pressure gradients must arise such that they push the fluid inwards, filling the central cavity. This process should occur in characteristic timescales $\tau \sim r/v_{th}$, where $r \sim 390$ μm is the radius of the hole and v_{th} is the thermal velocity. Since we do not have temperature measurements, I borrow the Thomson scattering measurements published by Bennett, *et al.* (2014) [40] as reference values.

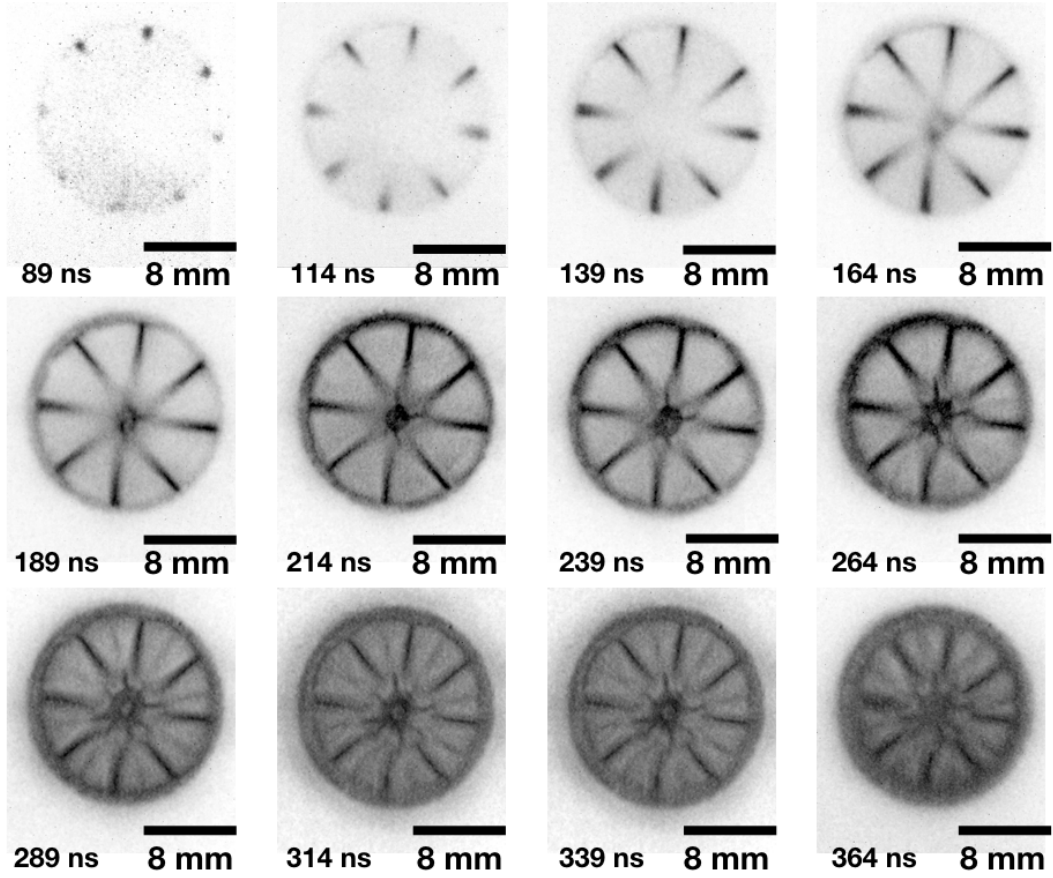


Figure 7.1: Time evolution of the experiment probed by end-on optical self-emission.

Assuming that the self-emission of the plasma is dominated by the electron emission, we consider $ZT_e \sim 150 - 200$ eV, hence $T_e \sim 30 - 100$ eV for typical ionisations $Z \sim 2 - 5$. This means that $v_{th} \sim 2 - 4 \cdot 10^8$ cm/s, which is consistent with $\tau \sim 0.1 - 0.2$ ns, which is 3 orders-of-magnitude faster than what it is observed.

A better comparison can be achieved through the electron diffusion coefficient D_e , aiming for estimating the diffusion rate, which can give a macroscopic picture of the characteristic timescales required to fill the hollow structure. Some considerations: firstly, I neglect ambipolar diffusion, because it typically occurs in weakly ionised plasmas so that the density of neutrals is much larger than the electron and ion densities. Secondly, I also neglect effects of the magnetic field, because in a non-current-carrying precursor, the centre of the array is the region where it is the weakest [33], therefore diffusion is most likely dominated by hydrodynamics. Consider the Einstein relation for constant diffusion and collision rates [51]

$$D_e = \frac{k_B T_e}{m_e \nu_{ie}}, \quad (7.1)$$

where ν_{ie} is the collision rate (also termed relaxation rate) between ion and electrons and it is

given by (in *MKS* units)

$$\nu_{ie} = v_{th} \lambda_{mfp}^{-1} = \frac{n_e e^4 \Lambda}{8\pi \epsilon_0^2 Z v_{th}^3 m_e^2} \quad (7.2)$$

The electron density is measured via Mach Zehnder interferometry. To analyse the interferograms, a code named MAGIC developed in-house at Imperial College London was used with the purpose of obtaining the maps from highly complex interferometric data (see e.g. Swadling et al. [52]). The pre-processing of the interferograms is quite similar to the one used in Part I, can be seen in Figure 7.2. Due to time constraints only the 532 nm wavelength probing beam data was analysed, hence the analysis of the 355 nm interferograms is left as future work.

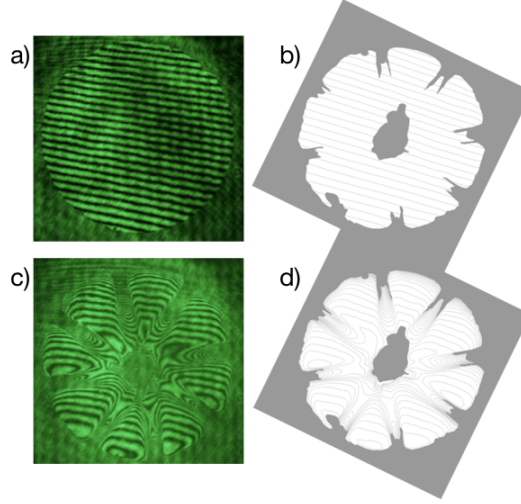


Figure 7.2: Interferometric data for 532 nm wavelength probing beam. a) Raw reference interferogram and, b) one-pixel width path of the reference interferogram. c) Plasma interferogram and, d) one-pixel width path of the plasma interferogram.

Figure 7.3 shows the electron density map calculated from the 532 nm laser probing. Notice that the rotating column completely obstructs the probing beam. This can be for three reasons: firstly, the electron density of the column is higher than the cutoff density for 532 nm; secondly, the motion of the plasma (which is neglected in the calculation followed from Hutchinson [20] and presented in Chapter 3) shifts the interferogram such that all the bright and dark fringes are mixed and/or; thirdly, the probing beam is heavily deviated by the plasma so that it escapes the detection system. The first two hypothesis are, in fact useful to constraint the electron density of the plasma and the flow velocity. However, to do the same based on the last one requires in detail measurements of the optical components. Thus, in a leap of optimism I use the former two possibilities to suggest constraints.

The cutoff density in *cgs* units is given by $n_c = \pi m_e c^2 / e^2 \lambda^2 = 4 \cdot 10^{21} \text{ cm}^{-3}$ for a 532 nm probing beam. In the reference interferogram (Figure 7.2a)) there are 26 fringes contained within the 16 mm array. Thus, the mean distance between fringes is $\sim 600 \mu\text{m}$. Hence, the flow velocity required to shift a 500 ps duration light pulse to pass such that the fringes are blurred by the motion

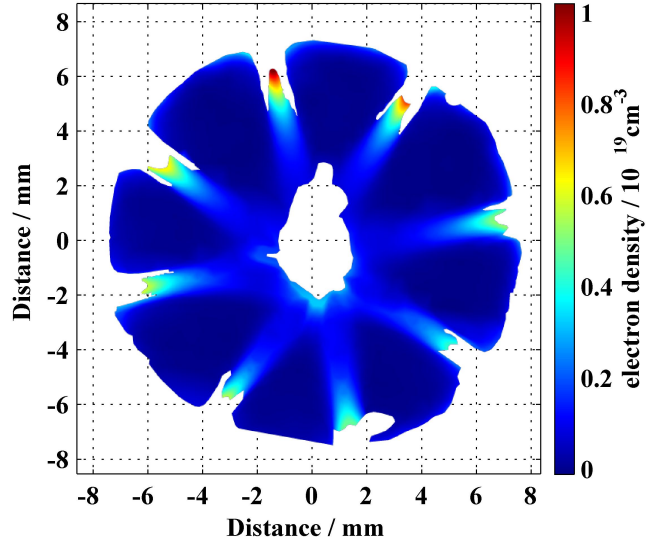


Figure 7.3: Map of electron density probed by the 532 nm wavelength end-on laser beam.

of the plasma is $v \sim 10^8$ cm/s. This is higher than the expected flow velocity, but not much higher. Future measurements with Thomson scattering will allow us to simultaneously measure the density and flow velocity.

Back to the relaxation time, given that it is much more plausible that the lines are mixed so that the interferograms cannot be observed, I will take a typical value for the electron number density $n_e \sim 5 \times 10^{18}$ cm $^{-3}$ just to give a rough estimate. Thus, from equation (7.1) the relaxation time is $\tau_{ie} = \nu_{se}^{-1} \sim 10^{-11}$ s, therefore, the diffusion coefficient for electrons is $D_e \sim 4 \times 10^5$ cm 2 /s, therefore the diffusion time for a region with characteristic length $r = 1$ mm is given by $\tau_{diff} = r^2/D_{se} \sim 25$ ns.

This are extremely encouraging results, as the time expected for diffusion to fill the hollow centre is much shorter than the time it seems to endure. Hence, one can assume that the centrifugal force in the non-inertial frame of reference of the fluid elements of the plasma hampers the diffusion inwards, sustaining the configuration.

7.2 Outflow Dynamics

Originally we were hoping to be able to observe and evaluate the performance of the experiment in terms of possible arc discharges amongst the wires, the return posts and/or electrodes, in addition to have an inspection of the rotating plasma from this viewpoint. An immediate conclusion is that the rotating Z pinch is robust against defects in the wires.

Notice that in all three images in Figure 7.4 the leftmost wire is extremely bent. This confirms the statement above about asymmetries induced by misplaced wires, as two main consequences appear in the ablation process: firstly, the ablation flares accelerated near the outwards bent wire

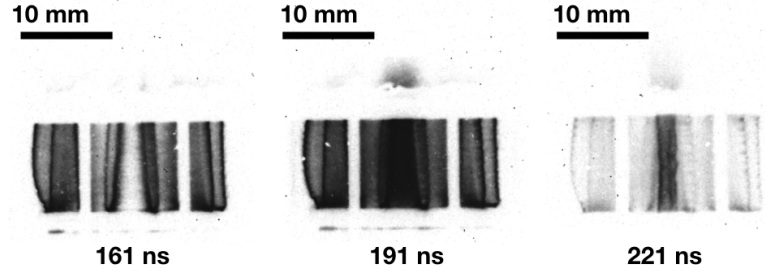


Figure 7.4: Images from UV/XUV self-emission using a $70 \mu\text{m}$ pinhole diameter.

take longer to reach the centre of the array and, secondly, the local magnetic field around the wire changes the effective inductance, thus modifying the ablation rate. Nevertheless, the end-on probing indicates that the rotating configuration can still be achieved.

However, an outstanding feature of this experiment appears from the side-on UV/XUV probing: the emission of a long, very collimated jet expelled by the top electrode (Figures 7.3 and 7.5). These two figures cannot be appropriately compared, because the pinhole diameter is different. Since we cannot see motion of the tip of the jet in Figure 7.5, we can only constraint its axial velocity using the $70 \mu\text{m}$ pinhole diameter MCP as $v \sim 3 \times 10^7 \text{ cm/s}$, which is comparable to typical velocities reported for the ablation flares [32].

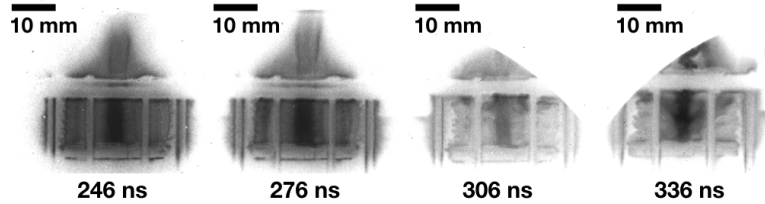


Figure 7.5: Images from UV/XUV self-emission using a $150 \mu\text{m}$ pinhole diameter.

From the side-on imaging we do not observe the typical MHD instabilities present in Z pinches associated with the Bessel modes $m = 0$ (sausage) and $m = 1$ (kink) within the array. This indicate that, if any current, it is small. Another possibility is that the rotating configuration mitigates the appearance of MHD instabilities. Studying this possibility is an outstanding problem on its own and way beyond the scope of this thesis.

Furthermore, up to times $t \sim 275 \text{ ns}$, there seems to be a correlation between the source and the jet, as the collimation degree seems to be inherited by the outflow from the rotating plasma within the array. This is extremely interesting because as the plasma emerges from the array, the pressure from the surrounding medium is reduced (as experimental vacuum in the chamber 10^{-5} Torr). Thus, the thermal pressure must be contained by magnetic pressure, *i.e.* $\beta \sim 1$. However, if the plasma is rotating, then there is a centrifugal component. If this is true, then the magnetisation of the plasma must be extremely high, $\beta \lesssim 1$. Given that apparently no current is being carried by the plasma, then it must be magnetic field lines advected from the source that allow the magnetic

field to confine the outflow.

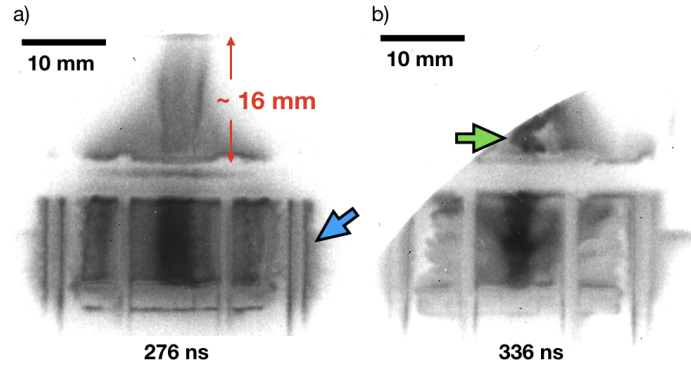


Figure 7.6: Images from UV/XUV self-emission. (a) At $t = 276$ ns a straight highly collimated jet is observed. (b) At $t = 336$ ns the jet develops a kink shape. The green arrow points at the kink jet, whereas the blue arrow to the ablation streams surrounding the return posts.

Another interesting result can be observed in Figure 7.6, which shows two different frames of MCP B with larger magnification. The initially well collimated jet extending straight upwards seems to enter a kink configuration at ~ 335 ns. This phenomenon can be observed in astrophysical jets such as the Crab nebula [47] and the stellar-mass black hole SS433 [56]. Notably, at these stages the stagnation phase appears to have already initiated in the array, breaking the correlation source-outflow.

Finally, an important result from the experiment is that the return posts exhibit ablation flares propagating outwards during the discharge. The ablation of the return posts can produce short-cut arcs between the wires and ground through the conducting plasma, disrupting the experiment, and can potentially break down the locality of the current through the return posts, meddling with the imposed magnetic topology within the array, killing the coherence of the off-axis imploding plasma flares.

7.3 Dimensionless Parameters and Scalability

Now I turn to apply the discussion in Chapter 5. There are certain difficulties in the estimation of physical parameters. For instance, to studying propagation of a jet, where one typically follows the tip of the jet, *i.e.* the leading edge and/or a fixed value for the electron density at different times. However, for the circulating flow we do not observe any ‘trackable’ feature, because there is no distinct representative point in the plasma that can be traced along the experiment. Thus, the characteristic velocity have to be estimated using prior work, simulations and constraints within this experimental set-up. In addition, electron temperature should also be estimated.

Here is where the discussion about placing error bars on the dimensionless parameters becomes extremely useful, as it allow us to quantify our ignorance, with the aims of taking future modifications to the experiments. I will compute dimensionless parameters for the rotating plasma within

the array and the resulting outflow separately.

Parameter	–	+	Scaling factor
u_0 (circulating flow)	4×10^6 cm/s	4×10^8 cm/s	10^2
v_0 (outflow)	3×10^6 cm/s	3×10^7 cm/s	10^1
r_0 (circulating flow)	1×10^{-2} cm	1×10^{-1} cm	10^1
z_0 (outflow)	1×10^1 cm	2×10^1 cm	$10^{0.3}$
n_e	10^{18} cm $^{-3}$	10^{21} cm $^{-3}$	10^3
T_e	30 eV	100 eV	$10^{0.5}$
B	10^4 G	10^5 G	10^1

Table 7.1: Extreme values for estimations of physical quantities.

In Table 7.1, I present the maximum and minimum values for physical quantities relevant in the experiments, denoted as + for maximum and – for minimum. At the rightmost column I present the scaling factor that relates these values as a power of 10. Notice that I am assuming that the temperature, electron number density and magnetic field are the same for the jet and rotating flow. This is quite a strong assumption, however this will provide me some numbers to give estimations. Anyway, the method for estimating errors in dimensionless parameters might be key to give some constraints.

Now I turn into discussing the dimensionless parameters for both the rotating plasma within the array and the outflow which are shown in Tables 7.2 and 7.3. In both cases the Reynolds number satisfies $Re_\nu \gg 1$, therefore the dissipative timescales are much longer when compared to the dynamical characteristic timescales, and therefore the kinetic viscosity is acting on much smaller spatial scales. A large Reynolds number is always associated with hydrodynamical turbulence, which might explain the high-temperature of the plasma observed by Bennett *et al* [40].

The magnetic Reynolds number is notable large in the case of the outflow. This means that the plasma satisfies the Lundquist theorem [55], thus the magnetic field is frozen-in the flow. This might explain why the jet sustains its high degree of collimation during the experiment. In contrast, the reference magnetic Reynolds number larger than unity, however in the most pessimistic scenario it might drop below unity.

The thermal diffusion is much more important in the rotating plasma than in the outflow, as the Peclet number within the array can have values below unity. Furthermore, the plasma exhibits strong radiative cooling, as the Radiation numbers are very large for both cases. Finally, the flows seems to be supersonic, which is consistent with the shocked regions observed using end-on probing of the experiments. Finally, the plasma β seems large. This is extremely unusual in Z pinch experiments as $\beta \sim 1$ is a stability criterion. Given than the possible values can drop below unity by more than an order-of-magnitude, this can be interpreted as the result of errors in the parameters estimates. In the future this observations can help to further constraint the uncertainty in the calculation of dimensionless parameters, as the steady state of the plasma might be use to

Dimensionless parameter	Value	Physical meaning
Re_ν	$10^{6.2\pm 3.2}$	Viscous dissipation negligible
Rm	$10^{1.4\pm 1.8}$	Magnetic field convection dominates over diffusion
Pe	$10^{3.3\pm 4.0}$	Thermal dissipation is negligible
Π_{thin}	$10^{15.2\pm 11.2}$	Radiatively cooled flow
M	$10^{1.2\pm 1.6}$	Supersonic flow
β	$10^{4.0\pm 5.5}$	Thermal-to-magnetic pressure ratio

Table 7.2: Dimensionless parameter for the rotating flow (within array).

relate variables.

Dimensionless parameter	Value	Physical meaning
Re_ν	$10^{8.2\pm 2.4}$	Viscous dissipation negligible
Rm	$10^{3.4\pm 0.9}$	Magnetic field is frozen-in the flow
Pe	$10^{4.3\pm 3.2}$	Thermal dissipation is negligible
Π_{thin}	$10^{11.0\pm 10.4}$	Radiatively cooled flow
M	$10^{1.1\pm 1.6}$	Supersonic flow
β	$10^{4.0\pm 5.5}$	Thermal-to-magnetic pressure ratio

Table 7.3: Dimensionless parameter for the outflow.

The comparison to actual astrophysical environments will be left as future work. The main point I would like to emphasize is that, within a large degree of certainty, for both rotating plasma and outflow are *scale invariant*, because all the reference values of the dimensionless parameters associated with dissipation are much larger than unity and only in extremely pessimistic circumstances they might drop below unity. Thus, within a large degree of certainty the dissipative timescales are irrelevant to the macroscopic dynamics. Therefore, if scale is unimportant for the temporal evolution of the experiment, it can be compared with systems at any larger scale (and smaller, up to the failure of MHD scale invariance). This is a property ubiquitous in astrophysical systems, where dissipation is also negligible. Hence, these represent extremely encouraging results.

Chapter 8

Conclusions and Future Work

During the second part of this thesis we investigated a novel Z pinch experiment, looking at producing magnetically-driven rotating plasma flows. The experiments were performed using the MAGPIE pulsed power generator, which delivers 1.2 MA in 240 ns with an output power of 1 TW. The load of the generator is a 10 mm height, 16 mm diameter cylindrical wire array consisting of $8 \times 40 \mu\text{m}$ Al wires. Placed close to this arrays, 8 steel rods used as return posts drive the plasma flares off-axis during the implosion.

The aims of this experiment is to simulate astrophysical environments as accretion disks, ubiquitously found in space. Succeeding in this endeavour would allow us to isolate, study and control in detail physical properties of these objects, shedding light onto outstanding problems in modern astrophysics. However, to compare laboratory and astrophysical plasmas rigorous criteria are required. Thus, I derived the MHD dimensionless equations and extensively discussed the scale invariance of such equations in detail. As a consequence the Euler similarity criteria states that two systems have comparable evolution if their dimensionless parameters in the same regime as compared to unity.

A large set of diagnostics was used to take a big amount of data from a single shot. Optical fast frame imaging together with laser interferometry was used to obtain end-on information of the time evolution of the experiment. Furthermore, 7 frames from MCP cameras where used to investigate the UV/XUV emission of the plasma.

After the off-axis implosion of the coronal plasma, the formation of a hollow structure at the centre of the array was observed. Two outstanding features were observed: firstly, it remained in a steady state for much longer than what one expects thermal expansion ~ 0.1 ns and diffusion ~ 25 ns . In contrast, the hollow structure persisted in time for times ≥ 250 ns. This is strong evidence of the rotation of the plasma, which could not be measured directly by following an ‘orbiting’ feature, as the time differences might be explained by the centrifugal force exerted on the plasma in the co-moving frame of reference. Together with the side-on imaging of the plasma, we determined that the experiment is robust against misplaced/bent wires and ablation on the surface of the return posts. Therefore, the radial component of the magnetic field provided by the

electrical current passing through the return posts remains rather invariant in symmetry breaking around the steel rods.

The electron density map for 532 nm wavelength laser probing was calculated. However, the fringes from the interferogram disappeared on the rotating plasma. This could be interpreted in three different way: the plasma having a density above the cutoff density $\sim 10^{21} \text{ cm}^{-3}$; the flow having a velocity $\gtrsim 10^8 \text{ cm/s}$ imposing a superposition of the bright and dark parts of the interferogram and; the probing beam being heavily deviated so they cannot be detected by the cameras. These number were used as upper constraints for the electron number density and flow velocity.

The side-on imaging showed a very interesting feature: a very long, supersonic, highly collimated jet of plasma. These jets are usually observed emitted in accreting systems, being ascribed to the accretion process. In the experiment, however, no accretion occurs and the rotating plasma produces an outflow. Neither it needs the presence of an *ad hoc* axial force, as opposed to other Z pinch experiments like radial foils and conical wire arrays. The high collimation of the jet can be explained in terms of a magnetic bottle advected by the plasma from the array, which must counterbalances the thermal pressure (and the centrifugal force if it is in fact rotating). This outflow shows a kink morphology at later times, once the stagnation process has been initiated within the wire array.

Future work will be centred in analysing the 355 nm wavelength probing laser interferogram, which can pass through the hollow part of the rotating plasma, as opposed to the 532 nm wavelength beam. Furthermore, Thomson scattering measurements will help to determine if the plasma is in fact rotating and, possible, being able to measure the velocity radial profile. This is extremely important to evaluate if the plasma satisfies the Rayleigh criterion of stability. If we are lucky, this experiment might be a way of producing the magneto-rotational instability in a Earth-based laboratory. This should be explored by testing different wire materials to control collisionality, cooling rates, resistivity, amongst others. Additionally an analytical model to describe the hollow rotating pinch should be developed as an important part of future investigations.

The outflow also should be further studies, as the transition to the kink configuration seems extremely interesting from a laboratory astrophysics viewpoint, as it might allow to correlate the dynamics of the jet and the source.

Appendices

APPENDIX A: Fitted parameters in Axial and Radial profiles

The following tables summarise the parameters fitted to the propagation trajectories for titanium and carbon plasmas. Two models were adjusted to the data. On the one hand, the drag model, *i.e.*

$$\mathbf{r}(t) = \mathbf{r}_s (1 - e^{-\beta t}) - \mathbf{r}_0, \quad (8.1)$$

where the initial velocity is a quantity of interest and given by $\mathbf{u}_0 = \mathbf{r}_s \beta$. On the other hand, the ballistic solution

$$\mathbf{r}(t) = \mathbf{u}_0 t + \mathbf{r}_0, \quad (8.2)$$

already contains explicitly the initial velocity \mathbf{u}_0 .

Parameters for Ti annular plasma experiments

	r_s (cm)	β (s ⁻¹)	r_0 (cm)	v_0 (cm/s)	R^2
FP	$(3.0 \pm 0.3) \times 10^0$	$(7.2 \pm 2.0) \times 10^5$	$(-2.1 \pm 1.0) \times 10^{-1}$	$(2.2 \pm 0.6) \times 10^6$	0.989
MF	$(3.1 \pm 0.3) \times 10^0$	$(7.5 \pm 1.0) \times 10^5$	$(0.6 \pm 1.0) \times 10^{-1}$	$(2.3 \pm 0.4) \times 10^6$	0.989

Table 8.1: Fitting parameters for the axial propagation of the shock in free propagation (FP) and in the external magnetic field (MF).

	r_s (cm)	β (s ⁻¹)	r_0 (cm)	v_0 (cm/s)	R^2
FP	$(3.8 \pm 0.2) \times 10^0$	$(5.7 \pm 0.9) \times 10^5$	$(-5.7 \pm 0.9) \times 10^{-1}$	$2.1 \pm 0.4 \times 10^6$	0.997
MF	$(3.8 \pm 0.2) \times 10^0$	$(5.3 \pm 0.9) \times 10^5$	$(-5.2 \pm 0.9) \times 10^{-1}$	$2.0 \pm 0.4 \times 10^6$	0.995

Table 8.2: Fitting parameters for the axial propagation of the leading edge in free propagation (FP) and in the external magnetic field (MF).

The plots presented in Chapter 3 are found by measuring the diameter of the plume. Thus, the initial radial velocity is half the slope of the plot. I denote \dot{D} as the time derivative of the diameter, *i.e.* the slope of the plot, and u_0 the radial velocity.

	r_0 (cm)	\dot{D} (cm/s)	u_0 (cm/s)	R^2
FP	$(9.7 \pm 0.9) \times 10^{-1}$	$(2.4 \pm 0.3) \times 10^6$	$(1.2 \pm 0.2) \times 10^6$	0.985
MF	$(1.1 \pm 0.1) \times 10^0$	$(2.5 \pm 0.3) \times 10^6$	$(1.3 \pm 0.2) \times 10^6$	0.977

Table 8.3: Fitting parameters for the radial propagation of the plume in free propagation (FP) and in the external magnetic field (MF).

Parameters for C annular plasma experiments

	r_s (cm)	β (s ⁻¹)	r_0 (cm)	v_0 (cm/s)	R^2
FP (1 atm)	$(5.0 \pm 1.4) \times 10^{-1}$	$(3.7 \pm 2.6) \times 10^5$	$(-9.7 \pm 2.3) \times 10^{-2}$	$1.8 \pm 1.4 \times 10^5$	0.995
MF (1 atm)	$(5.4 \pm 2.4) \times 10^{-1}$	$(2.7 \pm 1.6) \times 10^5$	$(-9.7 \pm 2.6) \times 10^{-2}$	$1.5 \pm 1.2 \times 10^5$	0.997
FP (0.3 atm)	$(6.1 \pm 1.6) \times 10^{-1}$	$(3.2 \pm 2.1) \times 10^5$	$(-8.7 \pm 2.2) \times 10^{-2}$	$2.0 \pm 1.4 \times 10^5$	0.997
MF (0.3 atm)	$(4.9 \pm 0.7) \times 10^{-1}$	$(5.5 \pm 2.7) \times 10^5$	$(-1.0 \pm 0.3) \times 10^{-1}$	$2.7 \pm 1.4 \times 10^5$	0.997
FP (0.2 atm)	$(6.6 \pm 1.5) \times 10^{-1}$	$(3.3 \pm 1.9) \times 10^5$	$(-1.0 \pm 1.9) \times 10^{-1}$	$2.2 \pm 1.4 \times 10^5$	0.995
MF (0.2 atm)	$(5.7 \pm 0.8) \times 10^{-1}$	$(4.7 \pm 2.2) \times 10^5$	$(-1.4 \pm 0.3) \times 10^{-1}$	$2.7 \pm 1.3 \times 10^5$	0.995

Table 8.4: Fitting parameters for the axial trajectory of the blast wave in free propagation (FP) and in the external magnetic field (MF) at different background pressure.

APPENDIX B: Derivation of the Dimensionless MHD Equations

The MHD equations for a optically thin, magnetised, compressible single fluid plasma are

$$\frac{\partial \rho}{\partial t} + \nabla \cdot (\rho \mathbf{u}) = 0, \quad (8.3a)$$

$$\frac{\partial}{\partial t}(\rho \mathbf{u}) + \mathbf{u} \cdot \nabla(\rho \mathbf{u}) = -\nabla p + \nabla \cdot \left(\rho \nu \left[\nabla \mathbf{u} + (\nabla \mathbf{u})^T - \frac{2}{3}(\nabla \cdot \mathbf{u})\underline{\mathbf{I}} \right] + \xi(\nabla \cdot \mathbf{u})\underline{\mathbf{I}} \right) + \frac{\mathbf{j} \times \mathbf{B}}{c}, \quad (8.3b)$$

$$\begin{aligned} \frac{\partial}{\partial t} \left[\rho \left(\varepsilon + \frac{u^2}{2} \right) \right] + \nabla \cdot \left[\rho \mathbf{u} \left(\varepsilon + \frac{u^2}{2} \right) + p \mathbf{u} \right] = & -\nabla \cdot \{ \mathbf{F}_R + E_R \mathbf{u} + \mathbf{Q} \\ & - \left(\rho \nu \left[\nabla \mathbf{u} + (\nabla \mathbf{u})^T - \frac{2}{3}(\nabla \cdot \mathbf{u})\underline{\mathbf{I}} \right] + \xi(\nabla \cdot \mathbf{u})\underline{\mathbf{I}} \right) \cdot \mathbf{u} \} - \mathbf{j} \cdot \mathbf{E}, \end{aligned} \quad (8.3c)$$

$$\frac{\partial \mathbf{B}}{\partial t} = \nabla \times \mathbf{u} \times \mathbf{B} + \eta \nabla^2 \mathbf{B}. \quad (8.3d)$$

Following [44], we will assume that the plasma is well described by a polytropic gas, thus satisfying the conditions

$$p = \frac{\rho(1+Z)k_B T}{Am_p}, \quad (8.4a)$$

$$c_s^2 = \left(\frac{\partial p}{\partial \rho} \right)_S = \frac{\gamma p}{\rho}, \quad (8.4b)$$

$$\varepsilon = \frac{p}{\rho(\gamma-1)} = \frac{c_s^2}{\gamma(\gamma-1)}, \quad (8.4c)$$

where $\gamma = 1 + 2/n \gtrsim 1$ is the polytropic exponent, n the polytropic index and equation (8.4b) assumes that the process is isoentropic. For a monoatomic, thermally dominated gas $\gamma = 5/3$ and will be regarded as constant. The set (8.4) is a good approximation unless the plasma is dominated by radiation and/or the plasma is under ionising processes¹. The latter assumption is the most delicate in our experiment, however a more realistic approximation is beyond the scope of this thesis, which is centred on scaling relations rather than exact calculations.

Let us compute the dimensionless form of each one separately, starting with the easiest. By taking the transformations (5.4) in (8.3b)

$$\frac{u_0}{l_0} \frac{\partial \rho_0 \hat{\rho}}{\partial \hat{t}} + \frac{1}{l_0} \hat{\nabla} \cdot (\rho_0 u_0 \hat{\rho} \hat{\mathbf{u}}) = 0 \longrightarrow \frac{u_0 \rho_0}{l_0} \frac{\partial \hat{\rho}}{\partial \hat{t}} + \frac{u_0 \rho_0}{l_0} \hat{\nabla} \cdot (\hat{\rho} \hat{\mathbf{u}}) = 0, \quad (8.5)$$

thus, the dimensionless mass conservation equation takes the form

$$\frac{\partial \hat{\rho}}{\partial \hat{t}} + \hat{\nabla} \cdot (\hat{\rho} \hat{\mathbf{u}}) = 0. \quad (8.6)$$

The next simplest equation is for induction (8.3d). Using the same straightforward procedure one finds

$$\frac{u_0 B_0}{l_0} \frac{\partial \hat{\mathbf{B}}}{\partial \hat{t}} = \frac{u_0 B_0}{l_0} \hat{\nabla} \times \hat{\mathbf{u}} \times \hat{\mathbf{B}} + \frac{B_0}{l_0^2} \eta \hat{\nabla}^2 \hat{\mathbf{B}}, \quad (8.7)$$

¹These cases are treated carefully in R. Paul Drake's book.

multiplying on both sides of equation (8.7) by l_0/u_0B_0 it becomes

$$\frac{\partial \hat{\mathbf{B}}}{\partial \hat{t}} = \hat{\nabla} \times \hat{\mathbf{u}} \times \hat{\mathbf{B}} + \frac{\eta}{u_0 l_0} \hat{\nabla}^2 \hat{\mathbf{B}}, \quad (8.8)$$

where, on the right-hand-side we can identify the magnetic Reynolds number $R_m \equiv u_0 l_0 / \eta$. To work the momentum equation it is easier to break (8.3c) down to each term and find their characteristic value decomposition separately. Thus,

$$\frac{\partial}{\partial \hat{t}}(\rho \mathbf{u}) + (\mathbf{u} \cdot \nabla)(\rho \mathbf{u}) = \frac{\rho_0 u_0}{l_0} \left[\frac{\partial}{\partial \hat{t}}(\hat{\rho} \hat{\mathbf{u}}) + (\hat{\mathbf{u}} \cdot \hat{\nabla})(\hat{\rho} \hat{\mathbf{u}}) \right], \quad (8.9a)$$

$$-\nabla p = -\frac{p_0}{l_0} \hat{\nabla} \hat{p}, \quad (8.9b)$$

$$\nabla \cdot \underline{\sigma}_\nu = \frac{u_0 \rho_0}{l_0} \hat{\nabla} \cdot \left(\hat{\rho} \nu \left[\hat{\nabla} \hat{\mathbf{u}} + (\hat{\nabla} \hat{\mathbf{u}})^T - \frac{2}{3}(\hat{\nabla} \cdot \hat{\mathbf{u}}) \underline{I} \right] + \frac{\xi}{\rho_0} (\hat{\nabla} \cdot \hat{\mathbf{u}}) \underline{I} \right), \quad (8.9c)$$

$$\frac{\mathbf{j} \times \mathbf{B}}{c} = \frac{j_0 B_0}{c} \hat{\mathbf{j}} \times \hat{\mathbf{B}}. \quad (8.9d)$$

By adding the set of equations (8.9) pondered by the factor $l_0/u_0^2 \rho_0$ the momentum equation is written as

$$\begin{aligned} \frac{\partial}{\partial \hat{t}}(\hat{\rho} \hat{\mathbf{u}}) + (\hat{\mathbf{u}} \cdot \hat{\nabla})(\hat{\rho} \hat{\mathbf{u}}) = & -\frac{p_0}{u_0^2 \rho_0} \hat{\nabla} \hat{p} + \hat{\nabla} \cdot \left(\frac{\nu}{u_0 l_0} \hat{\rho} \left[\hat{\nabla} \hat{\mathbf{u}} + (\hat{\nabla} \hat{\mathbf{u}})^T - \frac{2}{3}(\hat{\nabla} \cdot \hat{\mathbf{u}}) \underline{I} \right] \right. \\ & \left. + \frac{\xi}{u_0 l_0 \rho_0} (\hat{\nabla} \cdot \hat{\mathbf{u}}) \underline{I} \right) + \frac{l_0 j_0 B_0}{u_0^2 \rho_0 c} \hat{\mathbf{j}} \times \hat{\mathbf{B}}. \end{aligned} \quad (8.10)$$

Here we identify two hydrodynamic Reynolds number, $Re_\nu \equiv u_0 l_0 / \nu$ and the termed *bulk* Reynolds number associated with compression $Re_\xi \equiv u_0 l_0 \rho_0 / \xi$. Additionally, in the pressure term we find the speed of sound c_s given by (8.4b), leading to the appearance of the Mach number $M \equiv u_0 / c_s$, the dimensionless measurement for sub- or supersonic flow. The electromagnetic term must be analysed with caution. Let us write the Ampere law neglecting the displacement current and apply the decomposition, *i.e.*

$$\nabla \times \mathbf{B} = \frac{4\pi}{c} \mathbf{j} \longrightarrow \frac{B_0 c}{4\pi l_0 j_0} \hat{\nabla} \times \hat{\mathbf{B}} = \hat{\mathbf{j}}. \quad (8.11)$$

Notice that the right-hand-side of the latest equation in (8.11) is of order unity. By construction $\hat{\nabla} \times \hat{\mathbf{B}} \sim 1$ as well, therefore one concludes that a new condition must hold

$$\frac{B_0 c}{4\pi l_0 j_0} = 1, \quad (8.12)$$

which sets secondary conditions relating l_0 , j_0 and B_0 while implying

$$\frac{l_0 j_0}{c} = \frac{B_0}{4\pi} \Rightarrow \frac{l_0 j_0 B_0}{\rho_0 u_0^2 c} = \frac{B_0^2}{4\pi \rho_0} \frac{1}{u_0^2} = \frac{v_A^2}{u_0^2}, \quad (8.13)$$

where we have identified the reference Alfvén velocity $v_A \equiv B_0 / \sqrt{4\pi \rho_0}$, leading to the Alfvénic Mach number $M_A \equiv u_0 / v_A$. However, it will be convenient to relate it to the plasma $\beta \equiv$

$p_0/(B_0^2/8\pi)$ defined as the ratio between the thermal and magnetic pressure. Explicitly by introducing the speed of sound and the hydrodynamical Mach number in the right-hand-side of (8.13) we obtain

$$\frac{1}{M_A^2} = \frac{v_A^2}{u_0^2} = \frac{v_A^2}{\gamma M^2 c_s^2} = \frac{1}{\gamma M^2} \frac{B_0}{4\pi\rho_0} \frac{\rho_0}{p_0} = \frac{1}{\gamma M^2} \frac{2(B_0^2/8\pi)}{p_0} \equiv \frac{2}{\gamma M^2 \beta}. \quad (8.14)$$

Finally, as a consequence of (8.11) and (8.12) it is straightforward to see $\hat{\mathbf{j}} \times \hat{\mathbf{B}} = \hat{\nabla} \times \hat{\mathbf{B}} \times \hat{\mathbf{B}}$, which is the form that the momentum equation is commonly expressed in MHD.

We have one stone remaining ahead: the energy equation. Again, by breaking it term by term as we did for the momentum equation

$$\frac{\partial}{\partial t} \left[\rho \left(\varepsilon + \frac{\mathbf{u}^2}{2} \right) \right] = \frac{u_0^3 \rho_0}{l_0} \frac{\partial}{\partial \hat{t}} \left[\hat{\rho} \left(\frac{\varepsilon_0}{u_0^2} \hat{\varepsilon} + \frac{\hat{\mathbf{u}}^2}{2} \right) \right], \quad (8.15a)$$

$$\nabla \cdot \left[\rho \mathbf{u} \left(\varepsilon + \frac{\mathbf{u}^2}{2} \right) + p \mathbf{u} \right] = \frac{u_0^3 \rho_0}{l_0} \hat{\nabla} \cdot \left[\hat{\rho} \hat{\mathbf{u}} \left(\frac{\varepsilon_0}{u_0^2} \hat{\varepsilon} + \frac{\hat{\mathbf{u}}^2}{2} \right) + \frac{p_0}{u_0^2 \rho_0} \hat{p} \hat{\mathbf{u}} \right], \quad (8.15b)$$

$$-\nabla \cdot [\mathbf{F}_R + E_R \mathbf{u}] \approx -\rho \kappa_P \sigma T^4 = -\kappa_P \rho_0 \sigma T_0^4 \hat{\rho} \hat{T}^4, \quad (8.15c)$$

$$-\nabla \cdot \mathbf{Q} = \frac{1}{l_0} \hat{\nabla} \cdot \left(\frac{\chi_{th} \rho}{m} \frac{\gamma}{\gamma-1} k_B \nabla T \right) = \frac{\rho_0 \chi_{th} k_B T_0}{m l_0^2} \frac{\gamma}{\gamma-1} \hat{\nabla} \cdot (\hat{\nabla} \hat{T}), \quad (8.15d)$$

$$\nabla \cdot (\underline{\sigma}_\nu \cdot \mathbf{u}) = \frac{u_0^2 \rho_0}{l_0^2} \hat{\nabla} \cdot \left(\left[\nu \hat{\rho} \left\{ \hat{\nabla} \hat{\mathbf{u}} + (\hat{\nabla} \hat{\mathbf{u}})^T - \frac{2}{3} (\hat{\nabla} \cdot \hat{\mathbf{u}}) \underline{\underline{I}} \right\} + \frac{\xi}{\rho_0} (\hat{\nabla} \cdot \hat{\mathbf{u}}) \underline{\underline{I}} \right] \cdot \hat{\mathbf{u}} \right), \quad (8.15e)$$

$$-\mathbf{j} \cdot \mathbf{E} = -j_0 E_0 \hat{\mathbf{j}} \cdot \hat{\mathbf{E}}. \quad (8.15f)$$

where we have included the Planck opacity and the thermal heat flux in the diffusive limit, as proposed in [42]. Multiplying these equations by $l_0/u_0^3 \rho_0$ and summing them one finds

$$\begin{aligned} & \frac{\partial}{\partial \hat{t}} \left[\hat{\rho} \left(\frac{\varepsilon_0}{u_0^2} \hat{\varepsilon} + \frac{\hat{\mathbf{u}}^2}{2} \right) \right] + \hat{\nabla} \cdot \left[\hat{\rho} \hat{\mathbf{u}} \left(\frac{\varepsilon_0}{u_0^2} \hat{\varepsilon} + \frac{\hat{\mathbf{u}}^2}{2} \right) + \frac{p_0}{u_0^2 \rho_0} \hat{p} \hat{\mathbf{u}} \right] = -\frac{\kappa_P l_0 \sigma T_0^4}{u_0^3} \hat{\rho} \hat{T}^4 - \frac{l_0 j_0 E_0}{\rho_0 u_0^3} \hat{\mathbf{j}} \cdot \hat{\mathbf{E}} \\ & + \hat{\nabla} \cdot \left\{ \frac{u_0^3 l_0 m}{\chi_{th} k_B T_0} \frac{\gamma}{\gamma-1} \hat{\rho} \hat{\nabla} \hat{T} + \left[\frac{\nu}{u_0 l_0} \hat{\rho} \left(\hat{\nabla} \hat{\mathbf{u}} + (\hat{\nabla} \hat{\mathbf{u}})^T - \frac{2}{3} (\hat{\nabla} \cdot \hat{\mathbf{u}}) \underline{\underline{I}} \right) + \frac{\xi}{u_0 l_0 \rho_0} (\hat{\nabla} \cdot \hat{\mathbf{u}}) \underline{\underline{I}} \right] \cdot \hat{\mathbf{u}} \right\}. \end{aligned} \quad (8.16)$$

Notice that in this equation we obtain several dimensionless parameters defined before, in particular from the right-hand-side of equation (8.4c) it is easy to see that $\varepsilon_0 = 1/M^2 \gamma (\gamma - 1)$. In addition to those, by approximating $k_B T_0 \sim m u_0^2$ we can recognise the usual form of the Peclet number $Pe \equiv u_0 l_0 / \chi_{th}$ and the radiation number $\Pi_{thin} \equiv u_0^3 / l_0 \kappa_P \sigma T_0^4$.

Let us centre our attention in the coefficient $l_0 j_0 E_0 / \rho_0 u_0^3$. Notice than using the same argument to analyse Ampere law (8.11), Faraday law yields a relation for the electric and magnetic fields, *i.e.*

$$\frac{\partial \mathbf{B}}{\partial t} = -c \nabla \times \mathbf{E} \Rightarrow E_0 = \frac{u_0}{c} B_0. \quad (8.17)$$

Therefore, by imposing the latest condition together with (8.12) into $l_0 j_0 E_0 / \rho_0 u_0^3$, one obtains

$$\frac{l_0 j_0 E_0}{\rho_0 u_0^3} = \frac{l_0 j_0 B_0}{\rho_0 u_0^2 c} = \frac{B_0^2}{4\pi \rho_0 u_0^2} = \frac{2}{\gamma M^2 \beta}, \quad (8.18)$$

which is precisely a well-known result from above.

In summary, the set of dimensionless MHD equations calculated in (8.6), (8.8), (8.10) and (8.16), written in terms of the dimensionless parameters is

$$\frac{\partial \hat{\rho}}{\partial \hat{t}} + \hat{\nabla} \cdot (\hat{\rho} \hat{\mathbf{u}}) = 0, \quad (8.19a)$$

$$\begin{aligned} \frac{\partial}{\partial \hat{t}}(\hat{\rho} \hat{\mathbf{u}}) + (\hat{\mathbf{u}} \cdot \hat{\nabla})(\hat{\rho} \hat{\mathbf{u}}) = & -\frac{1}{\gamma M^2} \hat{\nabla} \hat{p} + \hat{\nabla} \cdot \left(\frac{1}{Re_\nu} \hat{\rho} \left[\hat{\nabla} \hat{\mathbf{u}} + (\hat{\nabla} \hat{\mathbf{u}})^T - \frac{2}{3} (\hat{\nabla} \cdot \hat{\mathbf{u}}) \underline{I} \right] \right. \\ & \left. + \frac{1}{Re_\xi} (\hat{\nabla} \cdot \hat{\mathbf{u}}) \underline{I} \right) + \frac{2}{\gamma M^2 \beta} \hat{\nabla} \times \hat{\mathbf{B}} \times \hat{\mathbf{B}}, \end{aligned} \quad (8.19b)$$

$$\begin{aligned} \frac{\partial}{\partial \hat{t}} \left[\hat{\rho} \left(\frac{1}{\gamma(\gamma-1)M^2} \hat{\varepsilon} + \frac{\hat{\mathbf{u}}^2}{2} \right) \right] + \hat{\nabla} \cdot \left[\hat{\rho} \hat{\mathbf{u}} \left(\frac{1}{\gamma(\gamma-1)M^2} \hat{\varepsilon} + \frac{\hat{\mathbf{u}}^2}{2} \right) + \frac{1}{\gamma M^2} \hat{p} \hat{\mathbf{u}} \right] = & \\ -\frac{1}{\Pi_{thin}} \hat{\rho} \hat{T}^4 - \frac{2}{\gamma M^2 \beta} \hat{\mathbf{j}} \cdot \hat{\mathbf{E}} + \hat{\nabla} \cdot \left\{ \frac{1}{Pe} \frac{\gamma}{\gamma-1} \hat{\rho} \hat{\nabla} \hat{T} \right. & \\ \left. + \left[\frac{1}{Re_\nu} \hat{\rho} \left(\hat{\nabla} \hat{\mathbf{u}} + (\hat{\nabla} \hat{\mathbf{u}})^T - \frac{2}{3} (\hat{\nabla} \cdot \hat{\mathbf{u}}) \underline{I} \right) + \frac{1}{Re_\xi} (\hat{\nabla} \cdot \hat{\mathbf{u}}) \underline{I} \right] \cdot \hat{\mathbf{u}} \right\}, & \end{aligned} \quad (8.19c)$$

$$\frac{\partial \hat{\mathbf{B}}}{\partial \hat{t}} = \hat{\nabla} \times \hat{\mathbf{u}} \times \hat{\mathbf{B}} + \frac{1}{R_m} \hat{\nabla}^2 \hat{\mathbf{B}} \quad (8.19d)$$

Let us now work out the linearly independent set of transformations discussed in (5.7). Notice that using equations (8.4), (8.12) and (8.18) it is easy to see that the appropriate characteristic values to scale \mathbf{E} , \mathbf{j} , T and ε are given by

$$\mathbf{E} \rightarrow \frac{u_0 B_0}{c} \hat{\mathbf{E}}, \quad \mathbf{j} \rightarrow \frac{B_0 c}{4\pi} \hat{\mathbf{j}}, \quad T \rightarrow \frac{p_0 / \rho_0}{Am_p k_B (Z+1)} \hat{T}, \quad \varepsilon \rightarrow \frac{p_0 / \rho_0}{\gamma-1} \hat{\varepsilon}. \quad (8.20)$$

Thus, by introducing (5.15) into these equations one obtains the relation between the physical quantities in two scalable systems, *i.e.*

$$E_0^{(2)} = af E_0^{(1)}, \quad j_0^{(2)} = fj_0^{(1)}, \quad T_0^{(2)} = dk^{-1} T_0^{(1)}, \quad \varepsilon_0^{(2)} = dk^{-1} \varepsilon_0^{(1)}. \quad (8.21)$$

Bibliography

- [1] A Reisenegger, F Zepeda. *Eur. Phys. J. A.* **52**, 52 (2016)
- [2] P H Scherrer, *et al.* *Sol Phys* **54**, 353 (1997)
- [3] P M Koch, Y W Tang, P T P Ho. *The Astrophys. Journal* **747**, 79 (19pp) (2012)
- [4] F Govoni and L Feretti. *Int. J. Mod. Phys. D* **13**, 1549 (2004)
- [5] F Suzuki-Vidal. *Nature Phys.* **11**, 98 (2015)
- [6] L Biermann, *Z Naturforsch.* **5a**, 65 (1950)
- [7] A Kandus, K E Kunze, C G Tsagas. *Phys. Reports* **505**, 1-58 (2011)
- [8] G Gregori, B Reville, F Miniati. *Phys. Reports* **601**, 1-34 (2015)
- [9] K Schoeffle, N F Loureiro, R A Fonseca, L O Silva. *Phys. Plasmas* **23**, 056304 (2016)
- [10] Ya B Zel'dovich & Yu P Raizer. *Physics of Shock Waves and High-Temperature Hydrodynamic Phenomena.* Dover (2002).
- [11] A Marcowith, *et al.* *Rep. Prog. Phys.* **79**, 046901 (2016)
- [12] E R Tubman, *et al.* *Phys. Plasmas*, **24**, 103124 (2017)
- [13] L J Radziemski, D A Cremers, *Laser-Induced Plasmas and Applications.* Dekker (1989)
- [14] P T Rumsby, J W M Paul, M M Masoud. *Plasma Phys.* **16**, 969-975 (1974)
- [15] F Veloso, *et al.* *Rev. of Sci. Instrum.* **77**, 063506 (2006)
- [16] F Veloso, *et al.* *Plasma Sources Sci. Technol.* **18**, 04512 (2009)
- [17] L M Cabalín & J J Laserna. *J Anal. Spectrom.* **19**, 445-450 (2004)
- [18] V Valenzuela, *et al.* *J Phys.: Conf. Ser.* **1043**, 012046 (2018)
- [19] J H McLeod. *J Opt. Soc. Am.* **44**, 8 (1954)
- [20] I H Hutchinson, *Principles of Plasma Diagnostics.* Cambridge Press, Second Edition (2002)

- [21] M Van Dyke, An Album of Fluid Motion. The Parabolic Press Stanford (1988)
- [22] P A Tipler & R A Llewellyn. Modern Physics. W H Freeman & Company, Fifth Edition (2008)
- [23] B P Abbott, *et al.* Phys. Rev. Lett. **116**, 061102 (2016)
- [24] R A Riley, *et al.* Rev. Sci. Instrum. **63**, 10 (1992)
- [25] M Hipp, *et al.* Measurement **36**, 53-66 (2004)
- [26] Magnum, Field Precision LLC (<http://www.fieldp.com>)
- [27] M Favre, *et al.* AIP Advances **7**, 085002 (2017)
- [28] C Graziani, *et al.* The Astroph. Journal **802**, 43 (22pp) (2015)
- [29] Yu I Ostrovsky, M M Butusov & G V Ostrovskaya. Interferometry by Holography. Springer-Verlag Berlin Heidelberg New York (1980)
- [30] B Fryxell *et al.* 2000, The Astroph. Journal Sup. Ser. **131**, 273 (2000)
- [31] S A Balbus. Annu. Rev. Astron. Astrophys. **41**, 555-97 (2003)
- [32] S C Bott, *et al.* Phys. Rev. E. **74**, 046403 (2006)
- [33] F Veloso, *et al.* Phys. Plasmas **22**, 072509 (2015)
- [34] M K Matzen. Phys. Plasmas **4**, 5 (1997)
- [35] J P Chittenden, *et al.* Plasma Phys. Controlled Fusion **46**, B457 (2004)
- [36] A Ciardi, *et al.* Phys. Plasmas **14**, 056501 (2007)
- [37] S V Lebedev, *et al.* Plasma Phys. Control. Fusion **47**, B465-B479 (2005)
- [38] G Munoz, V Valenzuela, *et al.* AIP Conf. Ser. **1639**, 92 (2014)
- [39] M Bocchi, *et al.* The Astrophys. Journal **767**, 84 (9pp) (2013)
- [40] M J Bennett, *et al.* AIP Conf. Proc. **1639**, 71-75 (2014)
- [41] D Ryutov, *et al.* The Astrophys. Journal **518**, 821-832 (1999)
- [42] J E Cross, B Reville, G Gregori. The Astrophys. Journal **795**, 59 (10pp) (2014)
- [43] L D Landau, E M Lifshitz, Fluid Mechanics. Oxford: Pergamon Press (1987)
- [44] R P Drake, High-Energy-Density Physics: Fundamentals, Inertial Fusion, and Experimental Astrophysics. Springer (2006)
- [45] H D Huba, Revised NRL Plasma Formulary. Washington, DC: Office of Naval Research (2013).

- [46] V Valenzuela-Villaseca, undergraduate project *Experiments in Conical Wire Array Z Pinch Plasmas*, Pontificia Universidad Catolica de Chile (2015).
- [47] C K Li, *et al.* Nature Comm. **7**, 13081 (2016)
- [48] S Mahajan, *The Art of Insight in Science and Engineering*. MIT Press (2014)
- [49] P Goldreich, S Mahajan, S Phinney, *Order-of-Magnitude Physics: Understanding the World With Dimensional Analysis, Educated Guesswork, and White Lies*. Unofficially published draft (1999)
- [50] I H Mitchell, *et al.* Rev. Sci. Instrum. **64**, 4 (1996)
- [51] Yu P Raizer, *Gas Discharge Physics*. Springer (1991)
- [52] G F Swadling, *et al.* Phys. Plasmas **20**, 022705 (2013)
- [53] Ultra UHSi 12/24 datasheet. Invisible Vision Company, (<http://www.invisiblevision.com>)
- [54] M A Liberman, J S De Groot, A Toor & R B Spielman. *Physics of High-Density Z Pinch Plasmas*. Springer (1998)
- [55] D A Gurnett & A Bhattacharjee. *Introduction to Plasma Physics With Space and Laboratory Applications*. Cambridge Press (2005)
- [56] K M Blundell & M G Bowler. The Astroph. Journal **616**, L159-L162 (2004)